

# ABSTRACT

Title of dissertation: A SEARCH FOR MUON NEUTRINOS  
COINCIDENT WITH NORTHERN  
GAMMA-RAY BURSTS USING ICECUBE

Michael Richman, Doctor of Philosophy, 2015

Dissertation directed by: Dr. Kara Hoffman  
Department of Physics

We present constraints derived from a search of four years of IceCube data for a prompt neutrino flux from gamma-ray bursts (GRBs). A single low-significance neutrino was found in coincidence with one of the 506 observed bursts, consistent with the expectation from atmospheric backgrounds. Although GRBs have been proposed as candidate sources for ultra-high energy cosmic rays, our limits on the neutrino flux disfavor much of the parameter space for the latest models. We also find that no more than  $\sim 1\%$  of the recently observed astrophysical neutrino flux consists of prompt emission from GRBs that are potentially observable by existing satellites. These results currently represent world-leading constraints on a prompt neutrino flux from GRBs.

In this thesis, we also introduce an original machine learning software package called `pybdt`. This implementation is now the *de facto* standard tool for machine-learning-based classification in IceCube analyses. Finally, we describe an extension of the unbinned likelihood method used in past searches to allow for the combination of data from different detector configurations with different background characteristics in the calculation of model constraints.

A SEARCH FOR MUON NEUTRINOS  
COINCIDENT WITH NORTHERN  
GAMMA-RAY BURSTS USING ICECUBE

by

Michael Richman

Dissertation submitted to the Faculty of the Graduate School of the  
University of Maryland, College Park in partial fulfillment  
of the requirements for the degree of  
Doctor of Philosophy  
2015

Advisory Committee:  
Dr. Kara Hoffman, Chair  
Dr. Gregory Sullivan  
Dr. Erik Blaufuss  
Dr. Rabindra Mohapatra  
Dr. Coleman Miller

## Acknowledgments

This dissertation is the culmination of years of work made possible only by technical and other help from many individuals. It should go without saying that the list begins with my parents, Rich and Laura Richman, who have always encouraged me to pursue my complementary interests in science and computing. During my tenure at The College of New Jersey, Romulo Ochoa and other instructors provided crucial opportunities for me to appreciate the usefulness of software as a tool in physics. At the University of Maryland (UMD), an advanced laboratory class with Simone Kulin revealed to me that data analysis is my academic passion.

Kara Hoffman became my advisor and mentor, and I cannot thank her enough for her role in my career. She enabled me to participate in two excellent collaborations: IceCube and the Askaryan Radio Array (ARA). This has led not only to fascinating work but also to travel opportunities I never imagined, including in particular two incredible journeys to the South Pole. I was given both the freedom to chart my own course and the guidance I needed to stay on track. I also want to thank Erik Blaufuss for copious level-headed advice and Greg Sullivan for challenging me to think about the big-picture implications of the design of our analysis.

I am indebted to many others affiliated with UMD. I learned almost everything I know about statistics from older graduate students Kevin Meagher, Peter Redl and Brian Christy, and this work flows directly from conversations with them about how to use and improve our GRB analysis method. Henrike Wissing brought me moments of clarity regarding the collaborative process. Alex Olivas provided numerous insights into the details of IceCube's complex simulation chain. I think it is fair to say that Troy Straszheim changed my life by convincing me to adopt Python as my primary analysis tool. Don La Dieu was always available

to make sure our computers “just work”. Robert Hellauer greatly simplified my work by making GRB-web vastly more usable and for “turning the crank” in modeling GRB neutrino spectra. Our secretary, Naomi Russo, consistently ensured that my various travels went off without a hitch. Lastly, I want to thank Robert and the other newer students and post-doc in our group — Ryan Maunu, Elim Cheung and John Felde — for learning from me in a way that reinforced my own understanding while building off of my work to accomplish other science goals I could never address alone. All of these people became not just colleagues, but friends that I will never forget.

This work is wholly dependent on the international IceCube Collaboration. Its culture of scientific integrity and computational sensibility make it a truly top-notch academic community. All 305 members of its author list deserve some level of thanks, but I want to identify some who have been instrumental to my success. Naoko Kurahashi has been reviewing my work from my first data unblinding proposal through the submission of a paper on my results. She gave me useful technical feedback, but more importantly, she saw my potential as a physicist long before I could see it for myself. Ignacio Taboada, Alexander Kappes and Nathan Whitehorn suggested numerous clarifications and improvement for my analysis. Jakob van Santen provided countless insights, especially pertaining to technical details in this thesis. Martin Schmitz and Florian Scheriau encouraged me to better understand and to improve my machine learning software, PyBDT, which is now being used by countless others to study a wide range of topics. Tania Wood consistently rekindled my passion for science at times when my interest in programming seemed to outshine my dedication to physics. Lisa Unger reminded me to take ownership of the trajectory of my career and my life, and I owe her thanks for empowering me to choose a path of continued research.

A large network of personal friends has made my tenure at UMD not only tolerable, but the best chapter of my life so far. Adriana Pilafova first opened my eyes to the possibility of earning my Ph.D. My fellow graduate students, bandmates and close friends Matt Severson, Bill McConville, Mike Azatov and Erin Moody helped me become more musically creative than ever before. The UMD ultimate frisbee club connected me with a diverse group of undergraduates who playfully call me “Pops” as we unite to enjoy a challenging yet relaxing sport that never fails to strengthen my body and clear my mind. Crystal Wheaden, in particular, became one of my closest friends, and she has tirelessly seen me through the best of times and the worst of times.

Finally, I want to acknowledge financial support from the National Science Foundation, the University of Maryland and the University of Wisconsin, which have facilitated the construction and operation of IceCube in general and the completion of this work in particular.

# Table of Contents

List of Tables	viii
List of Figures	ix
1 Introduction	1
2 Gamma-ray Bursts	7
2.1 History of GRB Observations	7
2.2 Modern GRB Detection	11
2.2.1 Fermi	11
2.2.2 Swift	12
2.2.3 Other Satellites and the IPN	12
2.2.4 Gamma-ray Coordinates Network	14
2.2.5 GRB-web	15
2.3 Fireball model	17
2.3.1 Cosmic Ray Production	18
2.3.2 Neutrino Emission	19
2.3.2.1 Top-down models	20
2.3.2.2 Bottom-Up Models	23
3 IceCube	28
3.1 Detection Principle	29
3.1.1 Muon Propagation	32
3.1.2 South Pole Ice	33
3.2 Optical Sensors	35
3.2.1 Contents and Operation	37
3.2.2 Calibration	40
3.2.2.1 Timing Calibration	40
3.2.2.2 Signal Response Calibration	41
3.2.2.3 Geometry Calibration	43
3.3 Data Acquisition	43
3.3.1 Trigger	43
3.3.2 Processing and Filtering	44
3.3.3 Experiment Control and Monitoring	46
4 Event Processing	48
4.1 Pulse Series Construction	48
4.1.1 DOM Cleaning	49
4.1.2 Waveform Calibration	49
4.1.3 Waveform Fitting	50
4.1.4 Pulse Series Cleaning	50
4.2 Reconstruction algorithms	52
4.2.1 LineFit	52

4.2.2	Single Photoelectron (SPE) Fit . . . . .	53
4.2.3	Multiple Photoelectron (MPE) Fit . . . . .	57
4.2.4	Angular Error Reconstruction . . . . .	58
4.2.5	Bayesian Up/Down Fit . . . . .	59
4.2.6	Split Reconstructions . . . . .	60
4.2.7	Energy Reconstruction . . . . .	61
4.3	Simulation . . . . .	62
4.3.1	Neutrino Simulation . . . . .	62
4.3.2	Cosmic-Ray Simulation . . . . .	64
4.3.3	Detection Simulation . . . . .	66
5	Neutrino Selection . . . . .	68
5.1	Event Quality Measures . . . . .	69
5.1.1	Fit Quality Parameters . . . . .	70
5.1.2	Fit Stability Parameters . . . . .	72
5.1.3	Event Topology Parameters . . . . .	74
5.2	Initial Data-Reduction Cuts . . . . .	81
5.2.1	Muon Filter . . . . .	81
5.2.2	Analysis Level Filter . . . . .	82
5.2.3	Basic Quality Cut . . . . .	83
5.3	Neutrino Level Cut . . . . .	84
5.3.1	Decision Trees . . . . .	85
5.3.1.1	Decision Tree Training . . . . .	86
5.3.2	Boosted and Randomized Decision Tree Forests . . . . .	87
5.3.2.1	Boosted Decision Tree Forests . . . . .	88
5.3.2.2	Random Decision Tree Forests . . . . .	90
5.3.2.3	Pruning . . . . .	91
5.3.3	Final Sample . . . . .	92
5.3.3.1	IC86-1 Classifier . . . . .	92
5.3.3.2	IC79 Classifier . . . . .	100
6	Unbinned Likelihood Analysis . . . . .	104
6.1	Probability Distribution Functions . . . . .	104
6.1.1	Time PDFs . . . . .	105
6.1.2	Direction PDFs . . . . .	105
6.1.3	Energy PDFs . . . . .	107
6.2	Test Statistic . . . . .	110
6.3	Frequentist Method . . . . .	112
6.3.1	Randomized Background Injection . . . . .	113
6.3.2	Randomized Signal Injection . . . . .	114
6.3.3	Significance . . . . .	116
6.3.4	Discovery Potential . . . . .	117
6.3.5	Upper limits . . . . .	117
6.3.6	Final Optimized Cuts . . . . .	118

7	IC40 through IC86 Year 1 Constraints	121
7.1	Multi-year Unbinned Likelihood Analysis . . . . .	121
7.1.1	Method . . . . .	121
7.1.2	Result . . . . .	122
7.2	Systematic Errors . . . . .	123
7.2.1	Optical Module Efficiency . . . . .	124
7.2.2	Photon Propagation in Ice . . . . .	125
7.2.3	Other Errors . . . . .	125
7.2.4	Total Systematic Error . . . . .	126
7.3	Model Constraints . . . . .	126
7.4	GRBs and Observed Astrophysical Neutrinos . . . . .	128
8	Conclusion and Outlook	132
A	GRB Catalogs	135
	Bibliography	151



## List of Tables

2.1	Satellite Observations of GRBs. . . . .	16
7.1	DOM Efficiency Systematics. . . . .	125
7.2	Ice Model Systematics. . . . .	125
7.3	Total Systematic Errors. . . . .	126
A.1	IC79 GRB Catalog. . . . .	136
A.2	IC86-1 GRB Catalog. . . . .	143
A.3	Omitted Bursts. . . . .	150

## List of Figures

1.1	Cosmic Ray Spectrum. . . . .	5
1.2	Hillas Plot. . . . .	6
2.1	BATSE Sky Map. . . . .	8
2.2	BATSE GRB Lightcurves. . . . .	9
2.3	BATSE GRB Durations. . . . .	10
2.4	Standard Fireball Model Spectra. . . . .	26
2.5	Photospheric Model Spectra. . . . .	26
2.6	ICMART Model Spectra. . . . .	27
3.1	IceCube Overview. . . . .	29
3.2	Neutrino Interaction Feynman Diagrams. . . . .	30
3.3	Range of Neutrino Interaction Products. . . . .	31
3.4	Initial Muon Energy. . . . .	32
3.5	Muon Energy Losses. . . . .	34
3.6	Scattering and Absorption Profiles. . . . .	35
3.7	Deployment Seasons. . . . .	36
3.8	DOM Schematic. . . . .	37
3.9	Digital Optical Module Mainboard. . . . .	39
3.10	DOMcal Charge Distribution. . . . .	42
4.1	Digitizer Front-end Shaping Functions. . . . .	51
4.2	Photon Propagation Geometry. . . . .	55
4.3	Pandel Function. . . . .	56
4.4	Muon Neutrino Cross Sections. . . . .	64
4.5	Density Profile in the PREM. . . . .	65
5.1	LineFit Distributions. . . . .	70

5.2	$\text{plogl}_{\text{SPE1}}$ Distributions. . . . .	72
5.3	Cramer-Rao Distributions. . . . .	73
5.4	$\Delta\Psi(\text{LineFit}, \text{MPE})$ Distributions. . . . .	74
5.5	Log-Bayes-ratio Distributions. . . . .	75
5.6	$\Delta\Psi(\text{Time Split 1}, \text{Time Split 2})$ Distributions. . . . .	76
5.7	$\Delta\Psi(\text{Geometry Split 1}, \text{Geometry Split 2})$ Distributions. . . . .	77
5.8	Split-min-zenith Distributions. . . . .	77
5.9	Split-min-log-Bayes-ratio Distributions. . . . .	78
5.10	$N_{\text{dir}}$ Distributions. . . . .	78
5.11	$L_{\text{dir}}$ Distributions. . . . .	79
5.12	Direct Ellipse Distributions. . . . .	79
5.13	$L_{\text{empty}}$ Distributions. . . . .	80
5.14	Separation Distributions. . . . .	80
5.15	Example Decision Tree. . . . .	85
5.16	Gini Index. . . . .	87
5.17	Decision tree weights . . . . .	90
5.18	Classifier Score Distributions. . . . .	93
5.19	Discovery Potential Proxy. . . . .	95
5.20	Discovery Potential Dependence on Training Parameters. . . . .	97
5.21	IC86-1 Signal Efficiency and Background Rates. . . . .	98
5.22	IC86-1 Angular Resolution. . . . .	99
5.23	IC86-1 Effective Area. . . . .	99
5.24	IC79 Signal Efficiency and Background Rates. . . . .	102
5.25	IC79 Angular Resolution. . . . .	103
5.26	IC79 Effective Area. . . . .	103
6.1	Time PDF Ratio. . . . .	106
6.2	Background Direction PDF. . . . .	108

6.3	Energy PDF Ratio. . . . .	109
6.4	Seasonal Variation. . . . .	113
6.5	Energy and Zenith Distribution. . . . .	115
6.6	Background Test Statistic Distribution. . . . .	116
6.7	Optimizing for Discovery. . . . .	119
6.8	Optimizing for Sensitivity. . . . .	120
7.1	Test Statistic vs. 4-yr Background. . . . .	123
7.2	Doubly-Broken Power Law Constraints. . . . .	128
7.3	Standard Fireball Model Constraints. . . . .	129
7.4	Photospheric Model Constraints. . . . .	130
7.5	ICMART Model Constraints. . . . .	130
7.6	Unbroken Power Law Constraints. . . . .	131

## Chapter 1: Introduction

In 1912, Viktor Hess used balloon flights to demonstrate that ionizing radiation observed on the Earth’s surface increased with altitude and therefore had an extraterrestrial origin [1]. The alien particles crashing into the upper atmosphere came to be known as cosmic rays. We now know that they consist of atomic nuclei; that the flux is very nearly isotropic; and that the spectrum follows an approximate power law over many decades in energy. Below 1 GeV, protons emitted by the sun dominate the flux. For somewhat higher energies, the sources are located elsewhere in the galaxy; recent work shows that supernova remnants are important contributors [2]. However, the observed spectrum, shown in Figure 1.1, extends to above  $10^{10}$  GeV before showing an exponential suppression. While lower energy nuclei from galactic sources can reach us after propagating in curved paths through galactic magnetic fields, at energies near or above  $\sim 10^{9.5}$  GeV, the so-called “ankle” due to the slight hardening of the spectrum, the sources must be extragalactic since such energetic nuclei could not be contained by galactic magnetic fields. These are referred to as ultra-high energy cosmic rays (UHECRs), and so far, no compelling evidence has revealed their sources.

Only the most energetic astrophysical objects could possibly produce the flux at the “ankle” — energies of  $10^{9.5}$ – $10^{10.5}$  GeV. The Hillas plot [3], shown in Figure 1.2, is a way of visualizing the cosmic ray production potential of various known objects. Based on the criterion that would-be cosmic rays must be confined by sufficient magnetic fields to reach the required energies on the size scale of the accelerator, gamma-ray bursts (GRBs) emerge as very promising source candidates.

GRBs are among the most violent explosions known in the universe. They are divided into two classes: long and short bursts. Long bursts release  $\mathcal{O}(10^{51})$  –

$10^{54}$  erg)  $\times \Omega/4\pi$ , where  $\Omega$  is the opening angle of the beamed gamma-ray emission, in  $2 - \sim 1000$  s while short bursts release approximately a factor of 100 less energy but in only  $\sim 10^{-3} - 2$  s. The release of such a large amount of energy in such small amounts of time places GRBs in the upper-left of the Hillas plot. Because they are well-localized in space and time, they are convenient objects to study; knowing where and when to look allows for very low-background experiments. Unfortunately, associating GRBs with cosmic ray production is nevertheless non-trivial. Curvature of the paths of charged particles by galactic and intergalactic magnetic fields makes direct correlation of cosmic rays to astrophysical sources impossible except for nearby objects and the most energetic cosmic rays.

Indirect detection via neutral particles such as photons or neutrinos is a more promising approach. If protons are present in the acceleration engine of GRBs, they will interact with photons in the engine. Therefore, one possible detection channel is gamma production via the Delta resonance:

$$p + \gamma \rightarrow \Delta^+ \rightarrow p + \pi^0 \rightarrow p + 2\gamma. \quad (1.1)$$

However, these gammas would have sufficiently high energies that most would interact with extragalactic background light — the sea of photons produced by stars and active galactic nuclei — before reaching Earth [5]. Those that survive propagation to Earth would be difficult to distinguish from the highest energy gammas that make up the bulk of the observed emission from GRBs.

The Delta resonance can also produce neutrinos:

$$p + \gamma \rightarrow \Delta^+ \rightarrow n + \pi^+ \rightarrow n + \mu^+ + \nu_\mu. \quad (1.2)$$

Unlike photons, neutrinos are unlikely to undergo additional interactions in the source or in extragalactic space, so they can reach the Earth unimpeded. However,

the small interaction cross section which enables them to escape the source and pass through space unimpeded also makes them very difficult to detect. The solution is to observe many GRBs with as large a detector as possible in search of a correlation.

IceCube is currently the best-suited detector for such a search. It consists of an array of 5160 optical sensors, occupying a cubic-km deep in the South Pole ice cap, that can detect the Cherenkov light emitted by energetic charged particles produced when neutrinos interact in the ice. Because muons can travel several km through the ice, the volume available for observing muon neutrinos is much larger than the instrumented volume. Earlier work [6,7] using two years of data from the partially completed array found no evidence of muon neutrinos correlated with GRBs. This led to the first significant constraints on neutrino emission, and in turn cosmic ray production, by GRBs. The theory community has responded by refining its models in terms of both the definitions of model inputs and the details of the calculation of model outputs.

In this thesis, similar methods to those used previously [6,7] are applied to a search for muon neutrinos from northern hemisphere GRBs in two more years of IceCube data, including the first year of data from the completed array and one year of data from the nearly-completed array. These two years of data are combined with two years of previously analyzed data from the partially-completed array to obtain world-leading constraints on neutrino production in GRBs with a sensitivity  $\sim 3\times$  better than previous searches. In addition to these results, we present some improvements to the analysis method. The most important of these is an original software package called `pybdt`, now commonly used for signal acceptance and background rejection in IceCube analyses, which implements standard boosted and randomized decision tree classification methods in a way that fits well into the rest of the IceCube software ecosystem. We also develop a

new extension to the unbinned likelihood method that allows for the calculation of combined results from different detector configurations and potentially even different detection channels.

The thesis is organized as follows: In chapters 2 and 3, we discuss GRBs and the IceCube detector. Chapter 4 covers data processing and simulation, and chapter 5 applies the resulting datasets to neutrino selection and background rejection. The unbinned likelihood method used to conduct the search is explained in chapter 6. In chapter 7, we extend the method for combined multi-year analyses before presenting the latest results derived from four years of data, including datasets analyzed for the first time in this work, and corrected to account for systematic uncertainties. Finally, concluding remarks are offered in chapter 8. Per-GRB details are tabulated in Appendix A.



## Cosmic Ray Spectra of Various Experiments

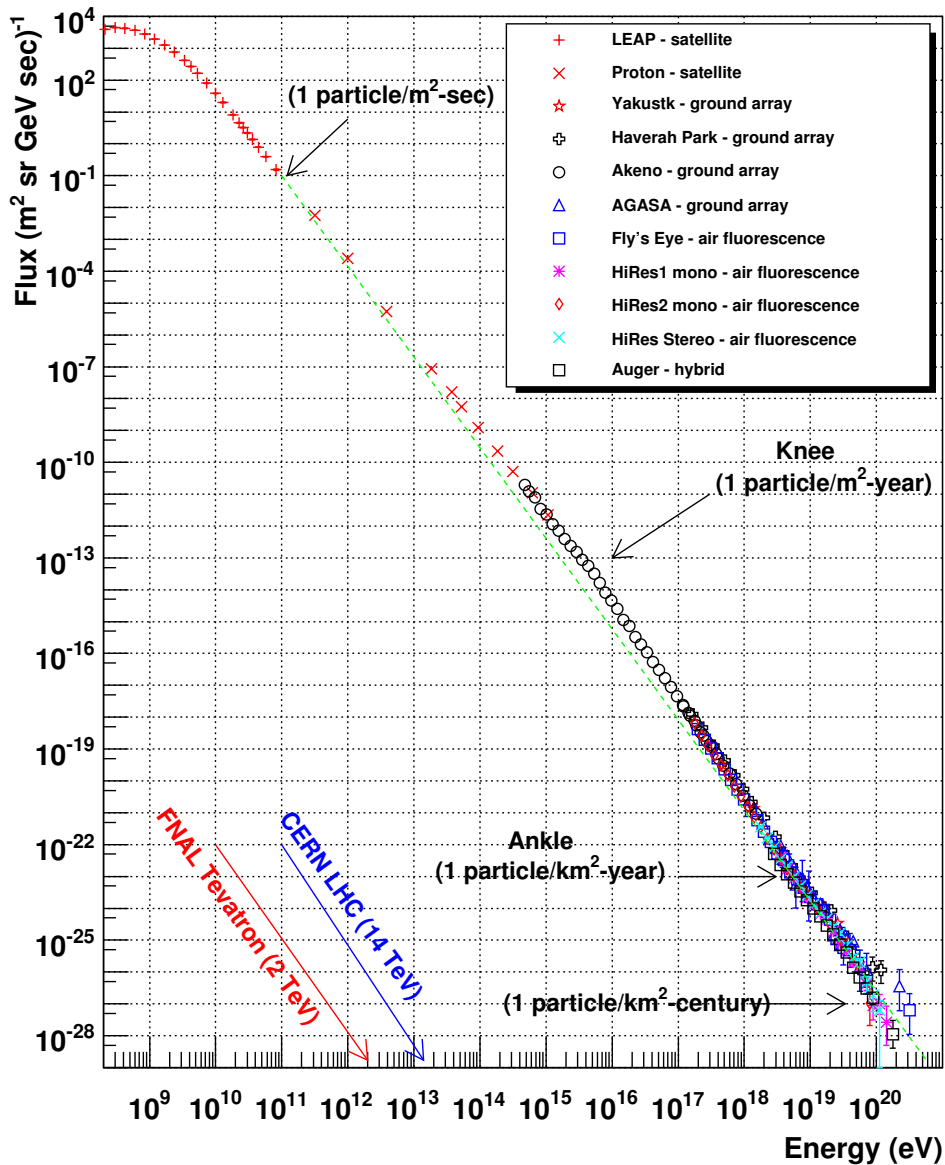


Figure 1.1: Measurements of the cosmic ray spectrum from several experiments. The observed spectrum shows only small deviations from an  $E^{-2.7}$  power law (shown as a dashed green line). While per-particle energies are well-measured, the distribution of the chemical composition of these particles — protons vs. heavier atomic nuclei — is still under active investigation. As discussed in the next chapter, if GRBs are important sources of UHECRs then the particles that make up the ankle flux would consist of protons. Figure from William Hanlon, University of Utah.

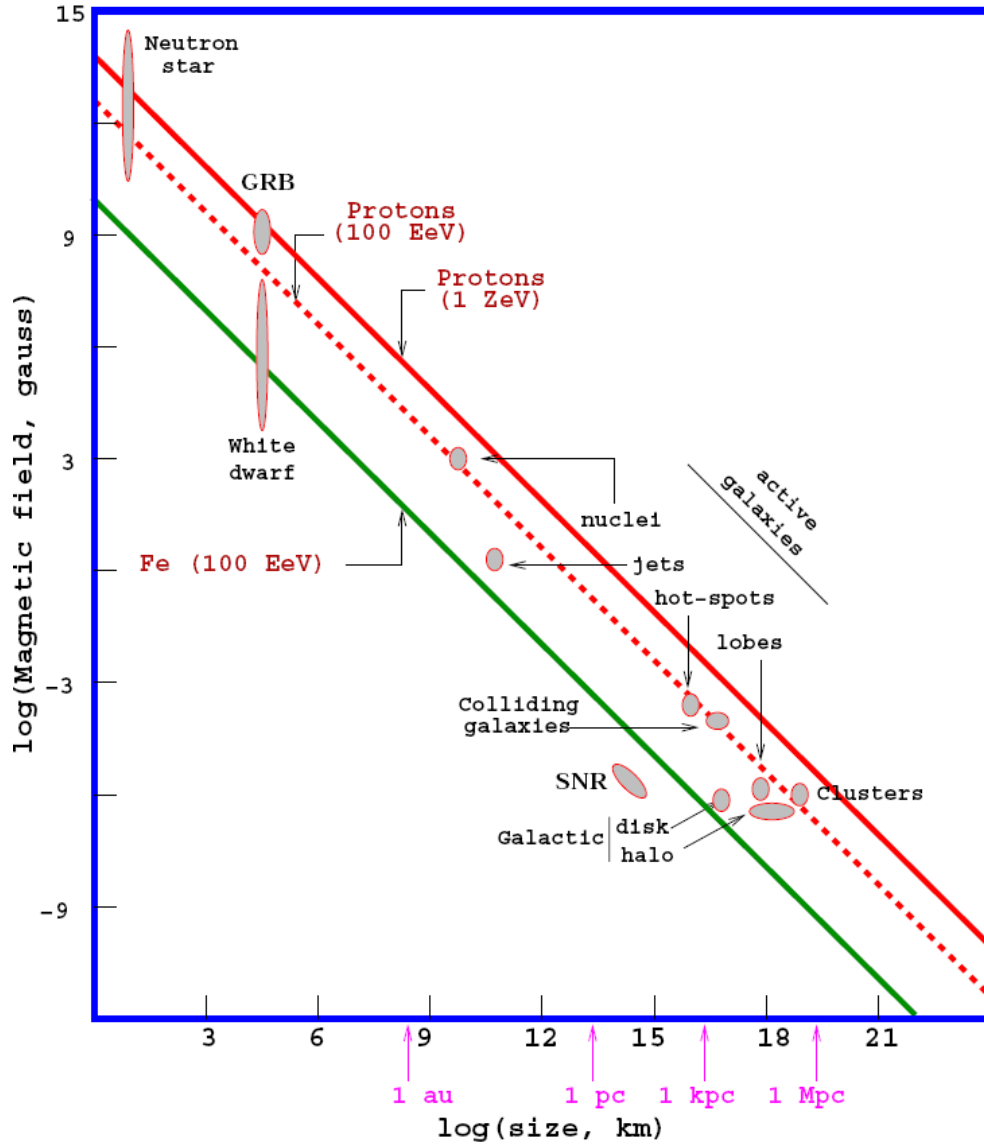


Figure 1.2: The Hillas plot. The magnetic field needed to contain a particle within a source long enough to obtain a given energy is a function of the size of the source and the species of the particle. Solid red indicates the threshold for producing  $10^{12}$  GeV protons; dotted red is the threshold for producing  $10^{11}$  GeV protons; and green is the threshold for producing  $10^{11}$  GeV iron nuclei. Figure from [4], which modified the original from [3].

## Chapter 2: Gamma-ray Bursts

Gamma-ray bursts (GRBs) are intense but brief signals observed by satellite-borne gamma-ray detectors. When one occurs, it outshines the remainder of the gamma-ray sky for about  $10^{-3}$ – $10^3$  s. Current satellites discover bursts at a rate of about 300 per year, distributed isotropically throughout the sky. As we will see, these violent events could be responsible for the production not only of gamma-rays and other electromagnetic radiation but also of ultra-high energy cosmic rays (UHECRs) via the acceleration of protons. If so, a potentially observable accompanying population of high energy neutrinos would be produced.

In this chapter we discuss electromagnetic observations of (GRBs) and the theory behind a possible correlated flux of high energy neutrinos. We will begin with an overview of the history of GRB observations. Then we describe the state-of-the-art in GRB detection. Finally, we will discuss the latest models tested in this experiment.

### 2.1 History of GRB Observations

Gamma-ray bursts were first observed by the Vela satellite program [8], which was intended to monitor for violations of the Nuclear Test Ban Treaty. As a result, the earliest observations, which took place in 1967, were classified for 7 years before being released to the public. Ultimately, burst timing and satellite-satellite timing triangulation excluded the Earth, as well as the sun, moon and visible supernovae, as sources [9].

The source locations of GRBs remained uncertain until observations by the Burst And Transient Source Experiment (BATSE) [10], an array of 8 NaI detectors on the corners of the Compton Gamma-ray Observatory (CGRO) which launched in 1990. Timing triangulation allowed for the localization of GRBs within a

## 2704 BATSE Gamma-Ray Bursts

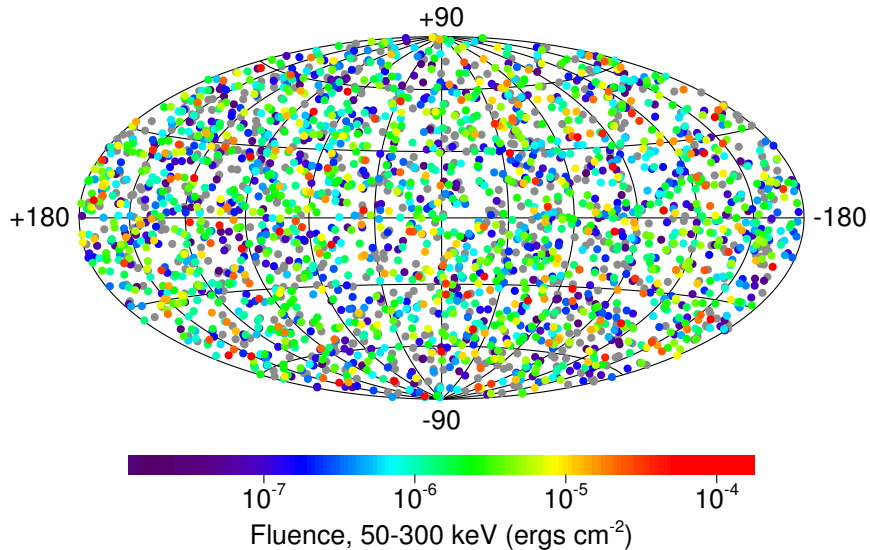


Figure 2.1: Map of 2704 BATSE GRBs [11] Bursts are plotted in galactic coordinates, with the plane of the Milky Way along the central horizontal axis. Bursts are colored according to their total fluence, with the brightest bursts shown in red, the dimmest in purple, and bursts with incomplete data in grey. The isotropic distribution of bursts was the first strong evidence of their extragalactic nature.

few degrees. A population of 2704 bursts demonstrated that the GRBs were distributed isotropically in the sky with no dependence on the burst brightness in gamma-rays (see Figure 2.1). This was the first strong evidence of the extragalactic nature of GRBs. BATSE also demonstrated the extreme variability of GRB lightcurves (Figure 2.2) as well as the existence of distinct classes of short ( $\lesssim 2$  s) and long bursts ( $\gtrsim 2$  s)(Figure 2.3).

In 1996, Beppo-SAX, a hard X-ray telescope, was launched [13]. This instrument provided the first evidence of X-ray afterglow emission by GRBs [14]. Later, the precise X-ray afterglow localization allowed subsequent optical follow-up, which in turn enabled redshift measurements [15, 16]. Measured redshifts at  $z \gtrsim 1$  provided definitive proof that GRBs are of extra-galactic origin. In addition, detailed analysis of one of these bursts [17] provided the first evidence of beamed emission from GRBs.

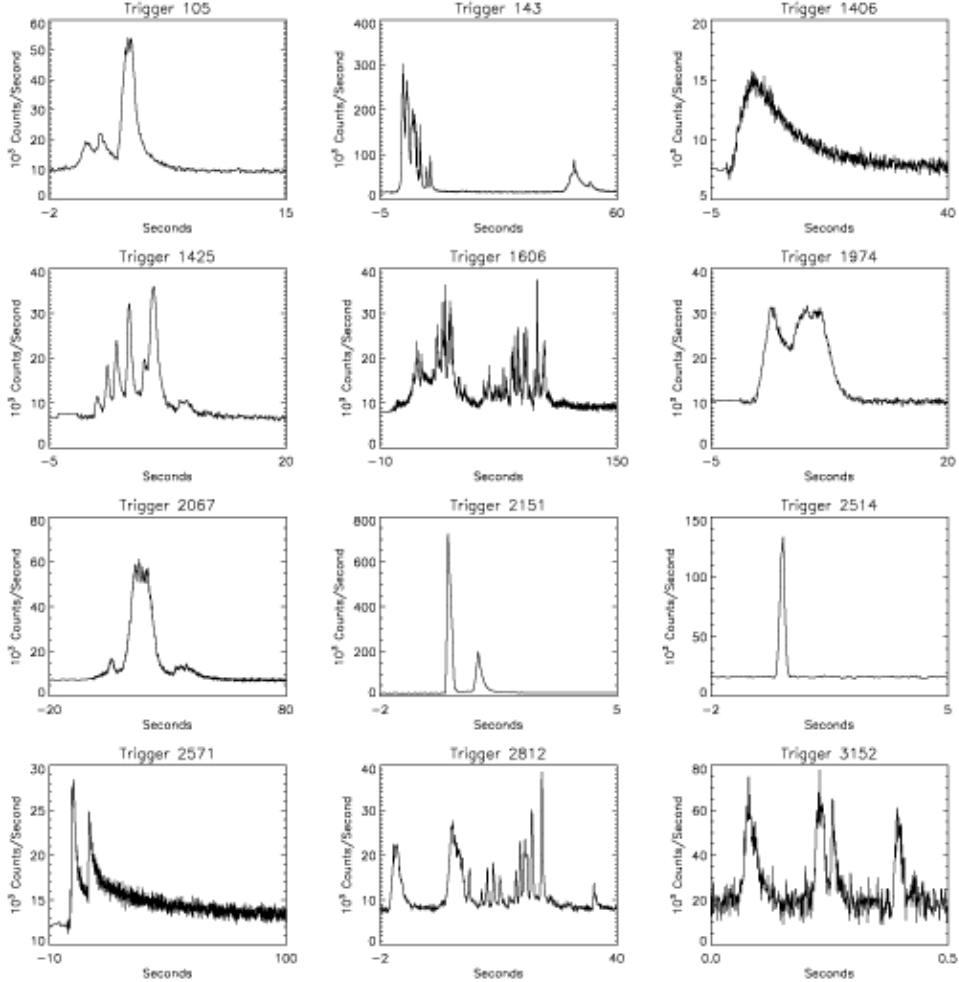


Figure 2.2: Lightcurves of 12 BATSE GRBs [12]. Gamma emission typically consists of one or more pulse with fast rise time and exponential decay, but unpredictable quiet periods and other erratic peak structures are common.

The High Energy Transient Explorer (HETE-2) [18] was launched in 2000 to perform multi-wavelength observations of GRBs. Its wide-field X-ray monitor (WXM) allowed it to transmit sub-arcsecond burst localizations to instruments on the ground within seconds of a GRB detection. The resulting rapid follow-up programs allowed the first spectroscopic confirmation of an association of long GRBs with supernovae [19]. HETE-2 also allowed the first observations of a broadband (X-ray to optical) afterglow for a short GRB, which bolstered existing gamma-ray evidence that short bursts arise from a distinct source population

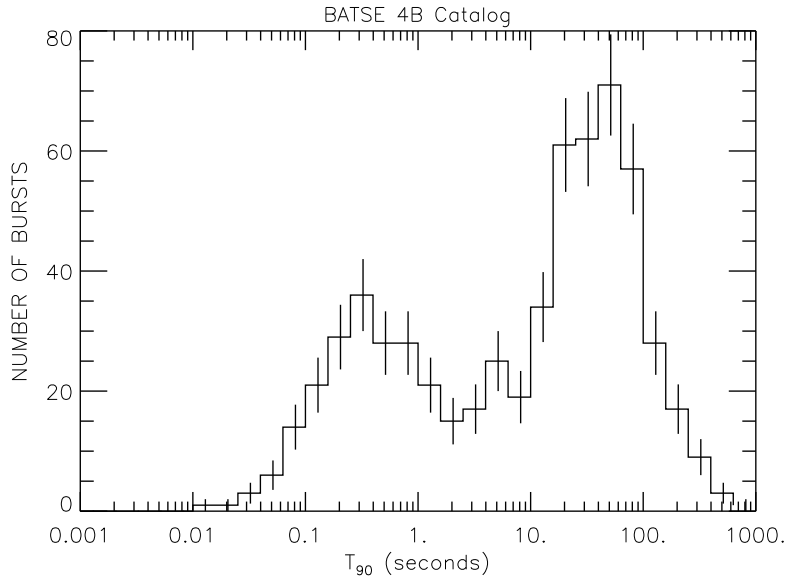


Figure 2.3: Distribution of burst durations from the fourth BATSE catalog [11]. This bimodal duration distribution is among the most important evidence for the existence of two distinct classes of GRB progenitor objects.

closer to Earth and with less energy than long bursts [20]; these bursts are thought to be driven by the merger of compact objects such as black holes or neutron stars to form a single black hole.

More recently, the Swift mission [21, 22] was launched in 2004, coupling a gamma-ray detector with X-ray, optical and ultraviolet (UV) follow-up instruments. Swift can slew to the direction of gamma emission within one minute of its observation, allowing extremely detailed broadband afterglow follow-up and precise burst localization. Swift has established the existence of bursts with redshifts of  $6 \lesssim z \lesssim 8$ , suggesting that some bursts date back to the earliest stars [23–26].

The latest satellite of historical significance for GRB observations is the Fermi Gamma-ray Space Telescope [27], which was launched in 2008. The on-board Large Area Telescope (LAT) can obtain detailed localization and spectral information for some very bright bursts [28]. However, the Gamma-ray Burst Monitor (GBM) [29] is especially useful in a transient coincidence search such as

the present experiment because of its wide-band and full-sky gamma-ray acceptance; that is, the GBM is sensitive to any sufficiently bright burst not occulted by the Earth, moon or sun. The high detection efficiency of the GBM is countered somewhat by larger statistical and systematic localization uncertainties; however, so many bursts are detected only by the GBM that it is nevertheless important to consider them in a coincidence search.

## 2.2 Modern GRB Detection

Above, we considered the historical significance of some key GRB observations. Today, GRBs are monitored by a wide array of instruments deployed throughout the solar system. In this section, we will discuss the technical details of various missions — most importantly, Fermi and Swift — that contributed burst information used in this analysis. We also cover NASA’s Gamma-ray Coordinates Network, which is used to distribute burst information to the community, as well as GRB-web, a catalog of GRB properties maintained by IceCube.

### 2.2.1 Fermi

The Fermi Gamma-ray Space Telescope [27] consists of two gamma-ray instruments: the Large Area Telescope (LAT) [28] and the Gamma-ray Burst Monitor (GBM) [29]. The LAT is sensitive in the high energy 20 MeV–300 GeV band, with an energy-dependent field of view that is 2.4 sr at 1 GeV. The energy threshold of the LAT is too high to allow for efficient discovery of GRBs; however, detailed multi-band light curves and good localization are produced when the LAT does observe a GRB.

The GBM consists of 12 thallium activated sodium iodide [NaI(Tl)] detectors sensitive in the 8 keV–1 MeV range and two bismuth germinate (BGO) detectors

bridging the gap between the NaI(Tl) detectors and the LAT with a sensitive band of 200 keV–40 MeV. The GBM calculates burst positions using detector-detector timing offsets. The statistical uncertainty is 1–15° depending on the amplitude of the burst [29]. The systematic uncertainty has been estimated by comparison with more precise instruments such as Swift, and it can be parameterized as a sum of Gaussian errors: 2.6° with 72% weight and 10.4° with 28% weight [30]. The wide energy range and full-sky coverage of the GBM allow it to observe more bursts than any other single active observatory. For very bright bursts, it also triggers the satellite to slew so that the LAT can measure the afterglow lightcurve in detail for  $\sim 5$  hr. The GBM is currently the most prolific GRB discovery instrument.

### 2.2.2 Swift

Swift was launched in 2004 primarily for the purpose of studying GRBs [21]. In light of multi-observatory multi-wavelength observations, it was designed for rapid multi-wavelength observations by multiple instruments on a rapid-slewing satellite. The Burst Alert Telescope (BAT) scans the sky with a field of view of 1.4 sr. It is sensitive to gamma-rays in the 15–150 keV band. Upon detection of a burst, it calculates the burst position within 1–4 arcmin. Within a minute, the satellite autonomously slews so that the burst is in the field of view of the X-ray Telescope (XRT) and Ultraviolet/optical telescope (UVOT). The XRT performs spectroscopy in the 0.1–10 keV band. If X-ray emission is found, the XRT localizes the burst within 3–5 arcsec [31] and additional follow-up is performed in the 170–600 nm band by the UVOT, which can localize the burst within 0.3 arcsec.

### 2.2.3 Other Satellites and the IPN

While most burst information used in this experiment was obtained using Fermi and Swift, several other instruments provide useful data:



**Konus-WIND:** Konus is a full-sky gamma-ray detector on board the Global Geospace Science (GGS) WIND satellite [32, 33], which was launched in 1994. The satellite maintains a halo orbit around the Lagrangian point  $L1$ , the point between the Sun and the Earth where an object moves around the Sun with an orbital period of exactly one Earth year. Konus consists of two large NaI(Tl) scintillators oriented towards the north and south ecliptic poles. These scintillators alone do not allow for burst localization; however, high resolution (2 ms) light curve measurement and good spectral resolution in the 10 keV–10 MeV range are possible.

**INTEGRAL:** Like Swift, INTEGRAL [34] is designed for gamma-ray, X-ray and optical observation of gamma-ray sources. It is sensitive to gamma-rays in the 15 keV–10 MeV band, X-rays in the 3–35 keV band, and optical radiation near 550 nm. Its angular resolution is 12 arcmin. Because INTEGRAL has a smaller field of view than Swift, it does not contribute as many localizations to our analysis. The satellite also includes an Anti-Coincidence Shield (ACS) which, like Konus-WIND, can act as a full sky GRB monitor without independent localization.

**MAXI:** The Monitor of All-sky X-ray Image (MAXI) [35] is an X-ray scanner on board the International Space Station (ISS) [36]. It continuously monitors the X-ray sky in the 0.5–30 keV range. It can sometimes localize bursts based on their X-ray afterglow, and occasionally it can discover bursts independently based on extrapolation of the observed X-ray spectrum into the gamma-ray regime.

**AGILE and SuperAGILE:** AGILE and SuperAGILE [37] are detectors on board an Italian Space Agency satellite in low-Earth orbit. AGILE scans the gamma-ray sky in the 30 MeV–50 GeV. SuperAGILE is an X-ray detector

sensitive in the 15–45 keV. SuperAGILE has a field of view larger than 1 sr and angular resolution of 6 arcmin, allowing it to provide good localization for some GRBs.

**Suzaku:** Suzaku is a Japanese satellite consisting of a Hard X-ray Detector [38] and its ACS. Taken together, these instruments comprise the Suzaku Wideband All-sky Monitor (WAM) [39]. It is sensitive to the 50 keV–5 MeV energy band. As with Konus and the INTEGRAL ACS, Suzaku cannot localize bursts independently; however, it sometimes is able to provide good timing and spectral measurements.

GRBs can also be localized by triangulation using gamma detection timing information from multiple satellites. This is facilitated by the Third Interplanetary Network (IPN3) [40], which includes 2001 Mars Odyssey [41], the Reuven Ramaty High Energy Solar Spectroscopic Imager (RHESSI) [42], the Mercury Surface, Space Environment, Geochemistry and Ranging (MESSENGER) [43], as well as the instruments discussed above. In this way, satellites with no independent directional capabilities can nevertheless contribute to GRB localization. For some bursts, IPN3 triangulation provides the best available localization.

#### 2.2.4 Gamma-ray Coordinates Network

NASA’s Goddard Space Flight Center pools GRB observations using a system called the Gamma-ray Coordinates Network (GCN) [44], a part of the more general Transient Astronomy Network. GCN distributes over e-mail three types of messages: notices, circulars, and reports. Alerts are machine readable documents providing basic information immediately upon burst discovery to facilitate rapid follow-up by other instruments. Circulars provide refined timing, localization and spectral fit information in prose written by scientists after further data collec-

tion and analysis. Reports summarize all circulars for a given burst. Information distributed through GCN is stored in a permanent archive on the GCN website, where it can be mined for GRB data long after the burst has passed.

### 2.2.5 GRB-web

While GCN is useful for organizing multi-instrument burst observation, it does not provide a tabulated archive of burst information. IceCube, however, maintains a publicly-accessible archive called GRB-web [45]. This service provides a summary table of burst data for a user-specified date range as well as detailed information from all available GCN circulars. It also incorporates data from the Fermi-GBM catalogs [30, 46–48].

The summary table aggregates all available observations for each GRB. The burst start and stop times  $T_1$  and  $T_2$  are the earliest and latest times that any satellite reported gamma observations above background. The localization and corresponding angular error estimate are taken preferentially from Swift-UVOT, Swift-XRT, Swift-BAT, SuperAGILE, Fermi-LAT, IPN3, Fermi-GBM, Maxi, and INTEGRAL in this order. The gamma-ray fluence and spectral fit are taken preferentially from Fermi-GBM, Konus-WIND, Suzaku, Swift-BAT, and INTEGRAL in this order. These choices generally ensure that the best possible localization and widest-band spectral fit are used in subsequent analysis. Details about observations by different satellites and links to the corresponding GCN circulars are also accessible through the online interface. Figure 2.1 summarizes each instrument’s observations during the two years of new northern GRBs analyzed in this experiment. Additional catalog details are provided in Appendix A.

Detailed predictions of neutrino spectra, which will be discussed in Section 2.3.2, are derived from the observed per-burst gamma-ray spectra. Satellites report spectral fits to a power-law, a power-law with an exponential cutoff, or a

Satellite	Position	$T_1$	$T_2$	Fluence
Fermi-GBM	193 (62%)	199 (64%)	200 (64%)	218 (70%)
Fermi-LAT	2 (1%)	0 (0%)	0 (0%)	0 (0%)
INTEGRAL	4 (1%)	7 (2%)	7 (2%)	4 (1%)
IPN3	14 (5%)	0 (0%)	0 (0%)	0 (0%)
Konus-WIND	0 (0%)	19 (6%)	22 (7%)	28 (9%)
MAXI	2 (1%)	2 (1%)	2 (1%)	0 (0%)
SuperAGILE	3 (1%)	2 (1%)	2 (1%)	0 (0%)
Suzaku	0 (0%)	7 (2%)	4 (1%)	2 (1%)
Swift-BAT	20 (6%)	75 (24%)	74 (24%)	50 (16%)
Swift-UVOT	3 (1%)	0 (0%)	0 (0%)	0 (0%)
Swift-XRT	70 (23%)	0 (0%)	0 (0%)	0 (0%)

Table 2.1: GRB observations during the first year of operation of the completed detector and one year of operation of the nearly completed detector, by satellite.

Band function [49]. The latter is a smoothed doubly-broken power law and can be expressed as:

$$F_\gamma(E_\gamma) = f_\gamma \times \begin{cases} \left(\frac{E_\gamma}{100 \text{ keV}}\right)^{-\alpha_\gamma} \cdot \exp(-E_\gamma/E_0) & E_\gamma < \varepsilon_\gamma, \\ \left(\frac{E_\gamma}{100 \text{ keV}}\right)^{-\beta_\gamma} \left[\frac{(\beta_\gamma - \alpha_\gamma) \cdot E_0}{100 \text{ keV}}\right]^{\beta_\gamma - \alpha_\gamma} \exp(-\beta_\gamma - \alpha_\gamma) & E_\gamma \geq \varepsilon_\gamma, \end{cases} \quad (2.1)$$

where  $f_\gamma$  is the total gamma fluence,  $\alpha_\gamma$  and  $\beta_\gamma$  are the best fit spectral indices,  $E_0$  is a reported reference energy, and  $\varepsilon_\gamma = (\beta_\gamma - \alpha_\gamma) \cdot E_0$  is the gamma spectrum break energy. To simplify neutrino flux calculations, in GRB-web, all burst spectra are re-interpreted as broken power-laws of the form

$$F_\gamma(E_\gamma) = f_\gamma \times \begin{cases} \varepsilon_\gamma^{(\alpha_\gamma - \beta_\gamma)} E_\gamma^{-\alpha_\gamma} & E_\gamma < \varepsilon_\gamma, \\ E_\gamma^{-\beta_\gamma} & E_\gamma \geq \varepsilon_\gamma. \end{cases}$$

For bursts fit with a power-law,  $\alpha_\gamma$  is set to the measured power-law;  $\varepsilon_\gamma$  is set to 200 keV for long bursts and 1 MeV for short bursts; and  $\beta_\gamma = \alpha_\gamma + 1$ . For bursts fit with a power-law with an exponential cutoff,  $\alpha_\gamma$  is again set to the measured

power-law;  $\varepsilon_\gamma$  is set to the reported  $\varepsilon_{\text{cutoff}}$ ; and again  $\beta_\gamma = \alpha_\gamma + 1$ . For bursts fit with a Band function,  $\alpha_\gamma$  and  $\beta_\gamma$  are set to the reported spectral indices and  $\varepsilon_\gamma = \varepsilon_{\text{Band}} \cdot (\alpha_\gamma - \beta_\gamma)/(2 + \alpha_\gamma)/e$ , where  $e$  is the usual Euler constant. For bursts observed only by Fermi-GBM and for which the spectral indices and break energy are not provided, average values from the published Fermi-GBM spectral catalog are used [46]. Finally, the normalization  $f_\gamma$  is found by enforcing that the integral of the catalog broken power-law is equal to the fluence observed by the satellite in the energy band quoted in the circular along with the fit. The validity of this prescription for regularizing the gamma spectra has been considered in more detail previously [50]; here we continue applying the method as it has been used in earlier searches [6, 7, 51].

Some northern bursts occurring during the detector configurations used in this experiment were not suitable for analysis due to detector downtime, calibration runs, or test runs. The remaining catalog includes 293 bursts previously unanalyzed bursts over a two-year period. Combined with previous searches, the catalog includes 506 bursts over a four-year period.

## 2.3 Fireball model

The standard theoretical framework for GRBs is the fireball model. In the fireball model, matter accreting onto the progenitor — generally believed to be a supernova collapse for long bursts and a compact object merger for short bursts — is heated by the dissipation of gravitational energy and ejected in a jet along the rotation axis of the progenitor. The matter is driven away from the engine and into the interstellar medium in a highly relativistic fireball consisting of a series of plasma shells with slightly different velocities. Collisions between plasma shells produce shocks in the magnetic field near the shell boundaries, which largely confine charged particles to their shells. As shells with different speeds collide,

charged particles undergo first order Fermi acceleration, reflecting between shocks at the leading and trailing edge of their shell and ultimately achieving energies as high as  $10^{20}$  eV.

The fireball model elegantly accounts for several observed burst characteristics. The accretion-driven jet reduces the total initial energy required to produce the enormous fluence observed on Earth, relative to a hypothetical isotropic process. The colliding shells can produce the rapid variability of gamma-ray lightcurves. Emission from earlier in the outflow, where the fireball is optically thick to gamma-rays, produces the thermal emission observed in some bursts. The burst expands adiabatically as it coasts away from the progenitor and eventually is optically thin to gamma-rays. At this stage, internal shocks between plasma shells are thought to produce the observed non-thermal power-law spectrum emission via synchrotron radiation by Fermi-accelerated electrons. Eventually, the relativistic outflow collides with the surrounding interstellar medium. The resulting external shocks are thought to produce the observed broadband afterglow.

### 2.3.1 Cosmic Ray Production

Waxman noted in 1995 [52] that, if the matter initially injected into GRB fireballs contains protons or heavier nuclei — if it has some baryonic loading — then GRBs could account for most or all of the observed UHECR flux. Most models assume that the baryonic loading consists of protons. A high energy proton flux can be produced in GRBs because protons would be Fermi accelerated just as the electrons are. GRBs are promising candidates for UHECR acceleration because gamma-ray observations indicate an aggregate energy generation rate comparable to what is required to produce the UHECR flux. Furthermore, multi-wavelength observations require the fireball to contain significant energy in magnetic fields and to be highly relativistic, and similar constraints are imposed if

GRBs are the sources of UHECRs. The original argument [52] has been strengthened somewhat by recent measurements of the UHECR flux and the GRB redshift distribution [53].

However, the strong magnetic fields that confine the particles during acceleration would also tend to trap them as the fireball expands and cools. Recently, Baerwald et al [54, 55] considered this ejection problem in detail. At least three mechanisms may contribute to cosmic ray escape from the fireball. Direct escape is the most straightforward; protons near the edge of a plasma shell can leak out if they acquire enough energy that the Larmor radius, the radius of curvature of the particles in the local magnetic field, is larger than the distance to the edge of the shell. Additional protons may escape by diffusive processes. Proton escape generally becomes easier with increasing proton energy, such that the escape mechanism involved influences the emitted cosmic ray spectrum. Lastly, neutrons produced in  $p\gamma$  interactions would not be magnetically confined, and they would escape as cosmic rays unless the photon density is so high that most of them undergo  $n\gamma$  interactions. The authors find [55] that, ignoring constraints from neutrino searches, any combination of these effects can produce the ankle of the observed cosmic ray flux. However, the magnitude of the required baryonic loading depends on the escape mechanism. As we will see in the next section, this has strong implications for the constraints neutrino searches can place on GRB cosmic ray acceleration and escape.

### 2.3.2 Neutrino Emission

In 1997, Waxman and Bahcall [56] noted that during collisions between plasma shells, or internal shocks, protons of sufficiently high energy in the fireball

would interact with fireball gamma-rays through the Delta resonance:

$$p + \gamma \rightarrow \Delta^+ \rightarrow \begin{cases} n + \pi^+ & 1/3 \text{ of all cases,} \\ p + \pi^0 & 2/3 \text{ of all cases.} \end{cases} \quad (2.2)$$

The decay of the charged pions gives rise to a neutrino flux:

$$\begin{aligned} \pi^+ &\rightarrow \nu_\mu + \mu^+ \\ &\hookrightarrow e^+ + \nu_e + \bar{\nu}_\mu. \end{aligned} \quad (2.3)$$

While the Delta resonance process is expected to dominate neutrino production, all standard model  $p\gamma$  interactions can contribute. Models of the shape and normalization of the neutrino flux can be categorized as top-down or bottom-up; each approach is outlined in turn below.

### 2.3.2.1 Top-down models

Top-down models yield a neutrino flux prediction by postulating that the total diffuse UHE cosmic ray flux is produced by GRBs. Although the flux must originate from point sources and at specific times, the models provide aggregate predictions averaged in time and over the sky. We refer to these predictions as “quasi-diffuse.” These models generally follow the analytical prescription originally provided by Waxman and Bahcall [56]. We begin by considering the energy required for the Delta resonance process to proceed. To model the kinematics in the fireball, we require two special relativistic transformations. The first accounts for the burst’s position at a redshift  $z$ . The second transforms to the frame of the coasting fireball and is parameterized by an average bulk Lorentz factor  $\Gamma$  relative to the progenitor, where  $100 \lesssim \Gamma \lesssim 1000$ . Then, for a given photon energy  $E_\gamma$  observed at Earth, the energy required for the Delta resonance interaction to



proceed is

$$E_p = \frac{\Gamma^2}{(1+z)^2} \frac{m_\Delta^2 - m_p^2}{4E_\gamma}. \quad (2.4)$$

If the pion takes on average 1/5 of the available energy, and the final lepton states  $e^+$ ,  $\nu_e$ ,  $\nu_\mu$  and  $\bar{\nu}_\mu$  share the pion energy equally, then the resulting neutrino energy is  $E_\nu = E_p/20$ .

The interaction rate as a function of proton energy, and ultimately the neutrino spectrum as a function of neutrino energy, is calculated by integrating over the observed average burst gamma-ray spectrum, using the approximation that most interactions occur near the peak of the  $p + \gamma \rightarrow \Delta^+$  cross section. For sufficiently high  $E_p$ , and hence  $E_\nu$ , any photon can participate, and the neutrino spectrum traces the proton spectrum. At lower energies, the spectrum is harder (less steeply falling with energy) by one power of  $E_\nu$  because the interaction only takes place for proton interactions with higher energy photons. The value of this first break energy is proportional to  $\Gamma^2$  and inversely proportional to the average observed gamma-ray break energy. An additional spectral break occurs at higher energies, where intermediate pions and muons are sufficiently boosted, and therefore long-lived, to lose significant energy to adiabatic fireball expansion (steepening the spectrum by  $E_\nu^{-1}$ ) or synchrotron radiation (steepening the spectrum by  $E_\nu^{-2}$ ) before producing neutrinos through their decay.

In this dissertation, we provide constraints on neutrino flux models of the form

$$\Phi_\nu(E) = \Phi_0 \cdot \begin{cases} E^{-1} \varepsilon_b^{-1} & E < \varepsilon_b, \\ E^{-2} & \varepsilon_b \leq E < 10\varepsilon_b, \\ E^{-4} (10\varepsilon_b)^2 & 10\varepsilon_b \leq E, \end{cases} \quad (2.5)$$

where  $\varepsilon_b$  is the first break in the neutrino spectrum; the second break occurs at  $10\varepsilon_b$ ; and  $\Phi_0$  is the overall normalization. The spectral index of  $-2$  for  $\varepsilon_b \leq E < 10\varepsilon_b$  reflects an assumption that the proton spectrum in the fireball goes approximately as  $dN_p/dE_p \propto E^{-2}$ , which is natural under Fermi acceleration and which allows the production of the UHECR flux above the ankle. The soft  $E^{-4}$  spectrum above the second break energy reflects an assumption that synchrotron radiation dominates pion and muon energy losses at the highest energies. This assumption produces a lower total neutrino flux prediction compared to cooling dominated by adiabatic fireball expansion, and hence is conservative in the sense that it reduces our chance of overstating the implications of our constraints.

We interpret our results in the context of two top-down models that represent approximate extremes of the neutrino flux that would be expected if GRBs dominate UHE cosmic ray production. Each model depends upon measured values for the cosmic ray flux [57] to establish the neutrino flux normalization as well as the average measured gamma-ray spectral break [46] and an assumed typical bulk Lorentz factor  $\Gamma \sim 300$  to establish the neutrino break energies. The simplest case is that of full proton confinement, in which case cosmic rays escape GRBs only as neutrons. In this neutron-escape model, if we maintain that the Delta resonance dominates fireball  $p\gamma$  interactions, then equations (2.2) and (2.3) show that every cosmic ray is accompanied by three neutrinos. Our reference for this scenario is taken from Ahlers et al. [58].

On the other hand, the original prescription from Waxman and Bahcall [56] allows protons to escape the fireball freely, and thus the UHE cosmic ray flux is accompanied by fewer neutrinos. To relate the measured cosmic ray flux to a predicted neutrino flux, this case depends on additional assumptions for average burst parameters. One of these is an average GRB isotropic luminosity  $L_{\text{iso}} \sim 10^{51} \text{ erg s}^{-1}$ . This quantity is calculated by assuming that the energy flux

per time per area at Earth is representative of isotropic emission radiating in every direction from the burst engine. The other is a typical progenitor variability timescale  $t_v \sim 10^{-3}$  s, which is inferred from the rate of variation observed in GRB lightcurves. Both  $L_{\text{iso}}$  and  $t_v$  are measured in the frame of an observer on Earth.

### 2.3.2.2 Bottom-Up Models

Top-down analytic models provide a useful benchmark neutrino flux expectation. However, because of strong variation in the observed gamma-ray emission from burst to burst, it is desirable to derive a neutrino prediction on a per-burst basis using all available burst information. This was first done by Guetta, et al [59]. Their prescription is similar to the top-down models described above, but they use per-burst measured gamma-ray spectra and per-burst assumptions for the isotropic luminosity and variability timescale. Then it is assumed that fixed fractions of the total burst energy contribute to electron acceleration ( $f_e$ ) and proton acceleration ( $f_p = 1/f_e$ ). The baryonic loading  $f_p$  cannot be measured directly, and so it is typically assumed to take a value that approximately reproduces the Waxman-Bahcall prediction in the limit of large ensembles of bursts.

More recently, significant progress has been made in developing a more complete picture of both the interactions within the fireball [60] and the implications of different cosmic ray escape scenarios [54, 55]. While the underlying fireball model has not changed, its relationship to a possible neutrino signal has been clarified. The neutrino modeling improvements are two-fold. First, some corrections to the analytical treatment have been identified [60]. The spectral shape is adjusted by including the difference between the cooling breaks for muons and pions, along with a  $(1+z)$  special relativistic transformation for  $t_v$ . The normalization is adjusted due to energy losses of secondary particles and the energy-dependence of the mean free path of the protons, along with some missing factors in the pion pro-

duction efficiency. These analytical adjustments all reduce the expected neutrino flux for given burst parameters, although it should be noted that approximate agreement between the analytical per-burst model and the Waxman-Bahcall prescription can still be recovered by clearly identifying the energy range over which the baryonic loading  $f_p$  is defined [55] and choosing somewhat larger values for this quantity.

The second improvement is to replace the approximate treatment with a full numerical simulation of the particle physics of  $p\gamma$  interactions and particle propagation within the fireball. This method automatically accounts for the corrections listed above, and it was found that the revised analytical prediction agrees well with numerical simulation under the constraint that only  $p + \gamma \rightarrow \Delta^+$  interactions are allowed [60]. However, full numerical simulation accounts for other interaction channels, which enhances the neutrino flux expectation and shifts the spectral shape somewhat due to contributions from all other standard model processes, including multi-pion and kaon production modes.

We evaluate neutrino flux predictions for detailed bottom-up models using a wrapper for SOPHIA [61], a Monte Carlo software package that propagates an ensemble of particles in time according to the standard model. Our version of the program has been modified to account for the magnetic fields in the fireball plasma shells, where the energy in magnetic fields is assumed to be in equipartition with the energy in electrons. We consider three model variants. In the standard fireball scenario, internal shocks occur at a distance from the source determined by the variability timescale and the bulk Lorentz factor:

$$r_C \simeq 2\Gamma^2 c \frac{t_v}{1+z}. \quad (2.6)$$

We consider this scenario along with two alternatives. One is the photospheric

model, in which the dominant neutrino production occurs at a much smaller radius [62, 63]. The other is a Poynting-dominated flux model — Internal Collision-induced MAgnetic Reconnection and Turbulence, or ICMART — in which internal shocks and particle acceleration take place at a much larger radius [63]. Compared to the standard case, these alternative models produce much larger and much smaller neutrino fluxes, respectively, and therefore give a sense of the scale of model dependence in this experiment.

Our results are presented as exclusion contours in the  $f_p$ - $\Gamma$  parameter space, where all other parameters are either measured or assumed in the same way as in earlier work [51]. As in the analytic models, the expected neutrino flux scales linearly with the baryonic loading; the assumed value of  $\Gamma$ , however, adjusts the spectral shape in nontrivial ways. In our parameter space scans, we produce numerically-simulated per-burst spectra in increments of 50 in  $\Gamma$ . The neutrino spectra for some values of  $\Gamma$  and given a benchmark baryonic loading  $f_p = 10$ , summed over all 506 bursts included in the present analysis, are shown for each type of model in Figures 2.4 through 2.6. For the standard and photospheric models, we consider the range  $100 < \Gamma < 950$ . The normalization decreases and the softening of the spectrum shifts to higher energies with increasing  $\Gamma$ . Thus the expected TeV–PeV neutrino fluence, and ultimately the ability of IceCube to place meaningful constraints, also decrease with increasing  $\Gamma$ . These effects are stronger for the standard model than for the photospheric model. For ICMART, the dependence on  $\Gamma$  is stronger still, so we test this model only for smaller values  $50 < \Gamma < 400$ .

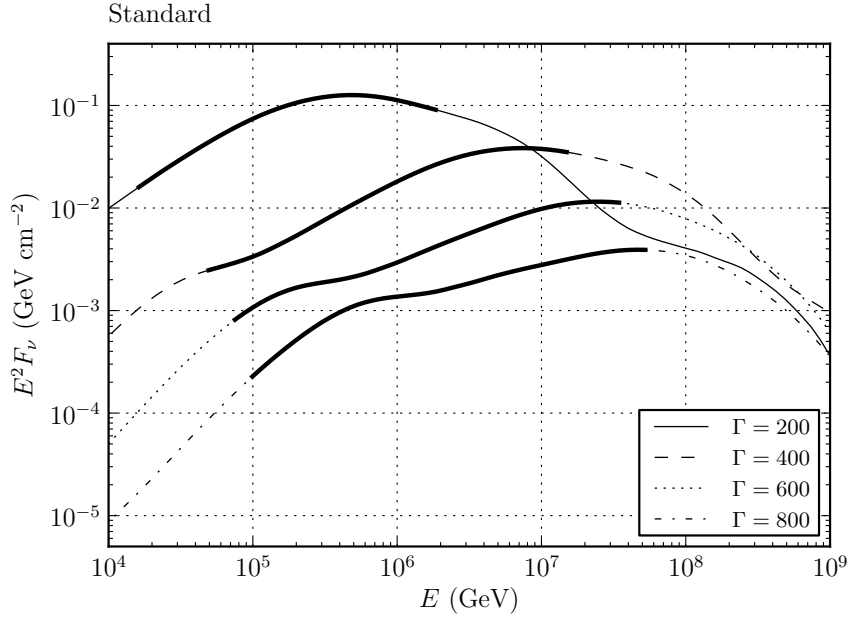


Figure 2.4: Summed burst spectra for  $f_p = 10$ , with varying  $\Gamma$  under numerical simulation of the standard fireball model. In this figure and the following two, the bold segments of the curves indicate the energy range containing 90% of neutrino events, based on simulation.

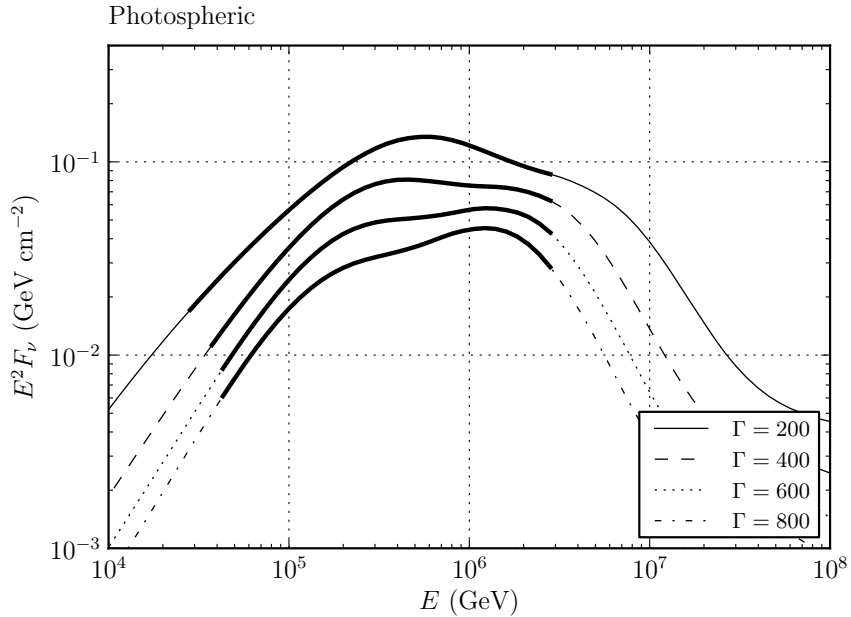


Figure 2.5: Summed burst spectra for  $f_p = 10$ , with varying  $\Gamma$  under numerical simulation of the photospheric fireball model.

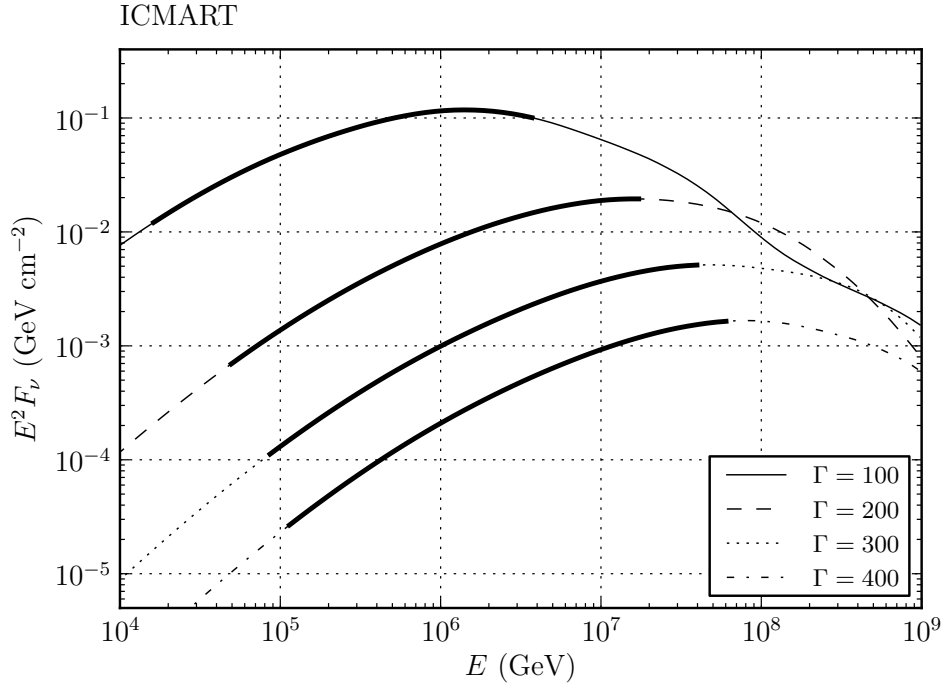


Figure 2.6: Summed burst spectra for  $f_p = 10$ , with varying  $\Gamma$  under numerical simulation of the ICMART model. Note that, because of the stronger dependence on  $\Gamma$  relative to the standard and photospheric scenarios, we restrict our attention to smaller values of  $\Gamma$  where the predicted neutrino signal is strong enough that we will be able to place meaningful constraints on the model.

## Chapter 3: IceCube

Neutrinos can reach the Earth from distant sources because their extremely low interaction cross section allows them to pass through intervening matter undisturbed. Unfortunately, this means that they rarely interact with matter on Earth as well. Therefore, very large detectors are required to detect astrophysical neutrinos. The IceCube Neutrino Observatory, generally referred to simply as IceCube, is a cubic-km detector deployed deep in the South Pole ice cap. It is the first detector large enough to enable the detection of the predicted neutrino flux from GRBs. An overview of the basic detector structure is shown in Figure 3.1.

IceCube observes neutrinos indirectly by using a hexagonal-prism array of photomultiplier tubes (PMTs) to collect Cherenkov light radiated by energetic charged particles produced by neutrinos when they interact in the ice cap or in the nearby rock. The excellent optical properties of the deep ice and the partial attenuation of the large background flux of downgoing cosmic ray-induced muons motivate the extreme depth of the array. The South Pole glacier is especially useful for the detection of charged current muon neutrino interactions because even product muons originating several km from the instrumented volume can reach the array and be observed. The elongation of muon tracks also enables  $\sim 1^\circ$  resolution for angular reconstruction.

In this chapter, we discuss the operation of IceCube. We will start with the interaction of neutrinos in the ice and the propagation of the muons they produce. Then we discuss the detector equipment in detail, starting with its modules for detecting Cherenkov light, and finally describing the operation of the array as a whole.



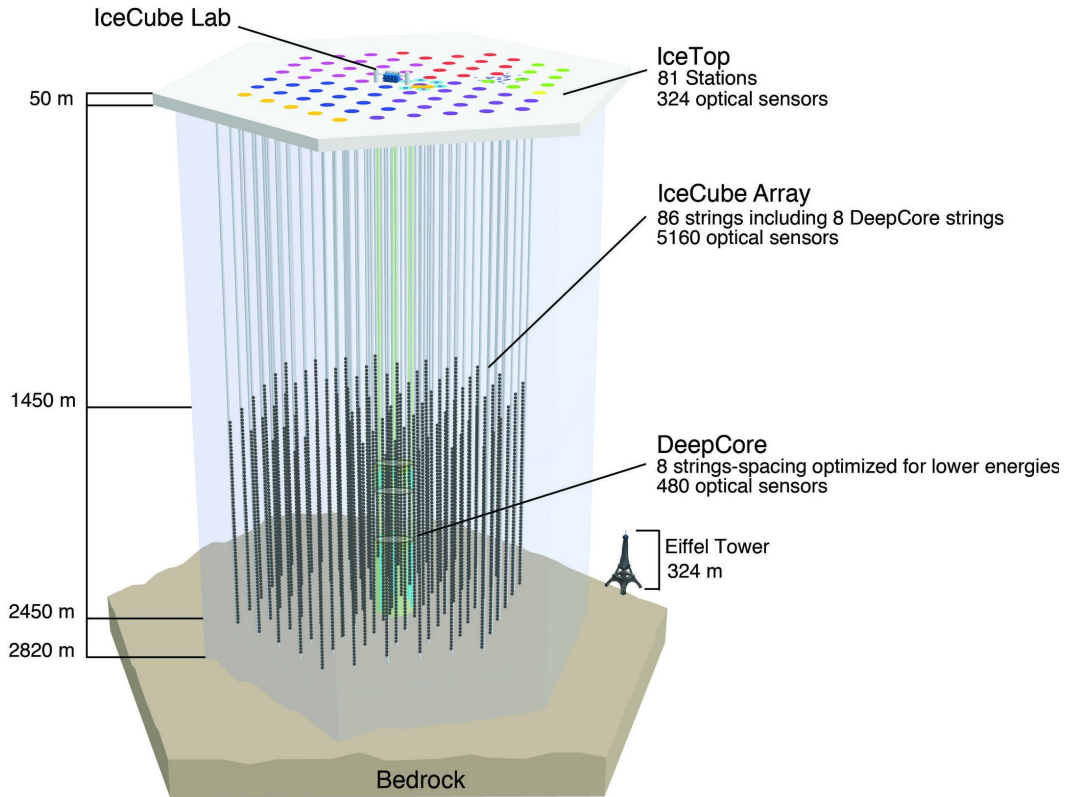


Figure 3.1: Overview of the IceCube Neutrino Observatory. IceCube consists of 86 strings of optical sensors with 60 sensors on each string. Near the center, eight of these strings are more densely spaced and constitute the DeepCore sub-array, which has a lower energy threshold than the rest of the detector. A surface array called IceTop consists of 81 two-tank stations with two optical sensors in each tank. The colored markers at the surface indicate the footprint of each Austral summer deployment season.

### 3.1 Detection Principle

In the standard model, neutrinos interact only via the weak force. Therefore, it is not possible to detect neutrino interactions directly. It is possible, however, to detect the light radiated by the relativistic product particles of neutrino interactions in matter. Figure 3.2 shows the neutrino interactions IceCube can detect. If a neutrino exchanges a  $W^\pm$  electroweak boson with a quark inside a proton or neutron, a charged lepton is produced and the quark (and the nucleon in which

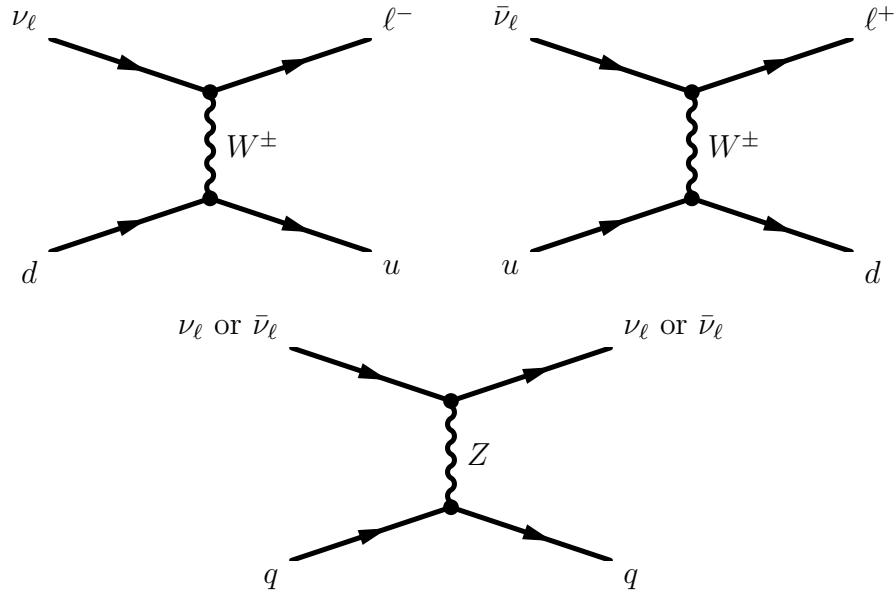


Figure 3.2: Neutrino interaction Feynman diagrams. In the upper two diagrams, a neutrino or antineutrino exchanges a  $W^\pm$  boson with a quark, changing the quark's flavor and producing a charged lepton. In the lower diagram, a neutrino or antineutrino exchanges a  $Z$  with a quark, imparting some of its energy to that quark.

it is a constituent) changes type. The  $W^\pm$  has unit charge, and therefore this is referred to as a charged current (CC) interaction. If a neutrino exchanges a  $Z$  electroweak boson with a quark, the neutrino imparts some of its energy to the nucleon, but the nucleon does not transmute. Because the  $Z$  is neutral, this is referred to as a neutral current (NC) interaction. Any neutrino interaction in ice produces a hadronic shower  $\sim 10$  m in length as the recoiling nucleus subsequently interacts with the surrounding matter.

The outcome of CC interactions depends on the neutrino flavor. In CC  $\nu_e$  interactions, the product electron or positron produces a shower of  $e^\pm$  and  $\gamma$  particles in the same location as the hadronic shower. In CC  $\nu_\tau$  interactions, the product  $\tau$  decays almost immediately. Most  $\tau$  decays are hadronic or electronic, and the decay products yield a second shower offset slightly from the first. In CC  $\nu_\mu$  interactions and a small fraction of  $\tau$  decays, however, the product muon travels a kilometer or more through the ice before decaying. The ranges of in-

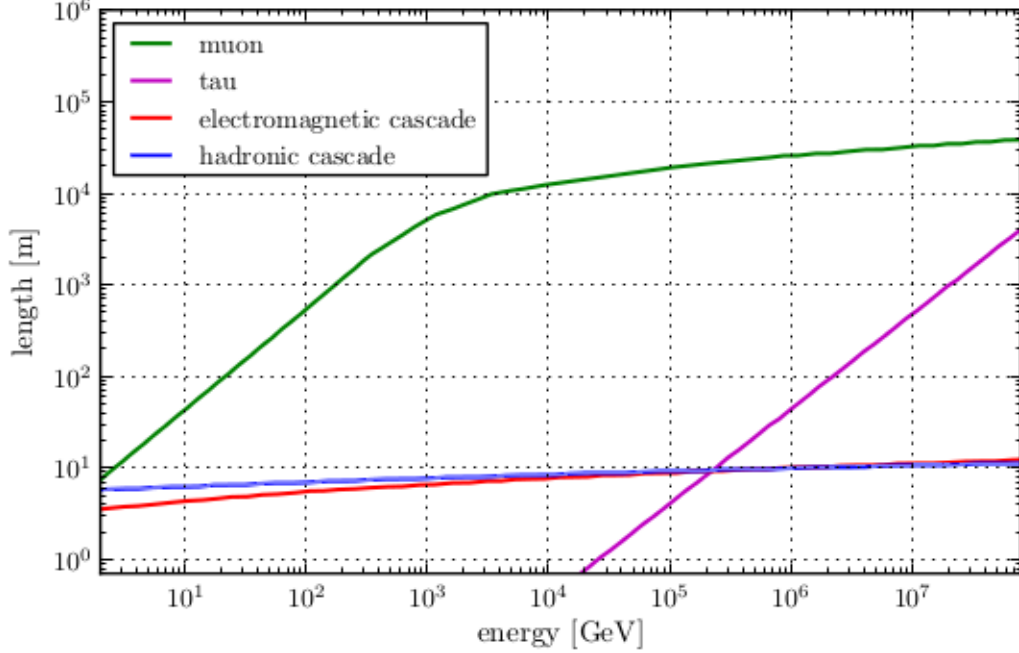


Figure 3.3: Range of neutrino interaction products in ice as a function of primary neutrino energy. For all interactions, the range increases with energy; however, this dependence is much stronger for muons and taus than for the other channels. Muons travel the farthest for most of IceCube’s sensitive energy range. Figure data from [64].

interaction product particles are shown in Figure 3.3. The long range of product muons provides a good lever arm for angular reconstruction and an enhanced effective detection volume since the interaction can occur far outside of the instrumented region. In this experiment, we search for  $\nu_\mu$  and  $\bar{\nu}_\mu$  by observing the Cherenkov light from their product muons. We restrict our attention to muons from the northern hemisphere or just above the horizon in the southern hemisphere. In these regions, any well-reconstructed muon track must be associated with a neutrino because the Earth or the ice cap itself will absorb all other cosmic ray induced backgrounds.

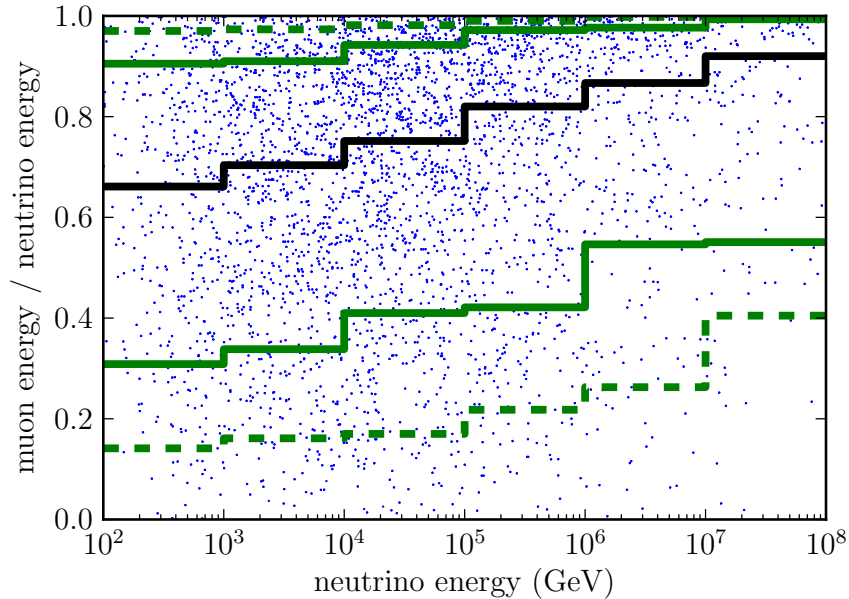


Figure 3.4: Distribution of the fraction of incident neutrino energy carried away by the muon as a function of incident neutrino energy, based on simulation (see Section 4.3 for more on simulation). Each blue dot is one simulated neutrino interaction. The black line represents the median value. Solid green lines show 68% containment of events, and dashed green lines show 90% containment.

### 3.1.1 Muon Propagation

The muon produced by a CC  $\nu_\mu$  or  $\bar{\nu}_\mu$  interaction proceeds through the ice with a fraction of the energy of the incident neutrino. In general, the probability of the muon carrying a large fraction of the neutrino energy increases with neutrino energy; the distribution of initial muon energies is shown in Figure 3.4. Because ice is a dense medium, the muon loses energy continuously through ionization and, above  $\sim 300$  GeV, stochastically through pair production, bremsstrahlung and photo-nuclear interactions. The average rate of energy loss can be approximated as

$$\frac{dE}{dx} = -a - bE. \quad (3.1)$$

The parameter  $a$  is found using the Bethe-Bloch formula [65] which describes the energy losses due to ionization. The parameter  $b$  gives the sum of the other energy losses. Both parameters vary with energy; however, in the energy range to which IceCube is sensitive, both  $a$  and  $b$  can be approximated by constants. The slow variation and relative contributions of these effects are shown by Figure 3.5. We can find the range  $x$  of a muon with initial energy  $E_0$  by integrating (3.1):

$$x \approx \frac{1}{b} \ln \left( 1 + \frac{b}{a} E_0 \right). \quad (3.2)$$

As the muon propagates through the ice, it polarizes the matter immediately surrounding it. For speeds  $v_\mu$  greater than the speed of light in the medium  $v_\ell = c/n$ , the polarization adds coherently at an angle  $\theta_C = \cos^{-1}(v_\ell/v_\mu)$  with respect to the path of the muon. The resulting emission is known as Cherenkov radiation [66], and it is the key to particle detection in IceCube.

### 3.1.2 South Pole Ice

IceCube owes its feasibility to the extreme purity of the South Pole ice; the glacial ice is more pure than any laboratory ice [68]. However, as a naturally-occurring glacier deposited over thousands of years, it is not perfectly homogeneous. Early measurements showed that at depths shallower than  $\lesssim 1.4$  km, air bubbles cause the scattering length of light to be very small [69]. This was part of the motivation for deploying IceCube between the depths of 1.4 and 2.4 km.

Proper simulation of IceCube’s various backgrounds and potential signals requires detailed knowledge of the optical properties of the ice. The most important of these are the absorption and scattering lengths. LED flashers deployed with the optical modules [68, 70] and dust-logging devices [71] have been used to make detailed *in situ* measurements of the absorption and scattering profiles,

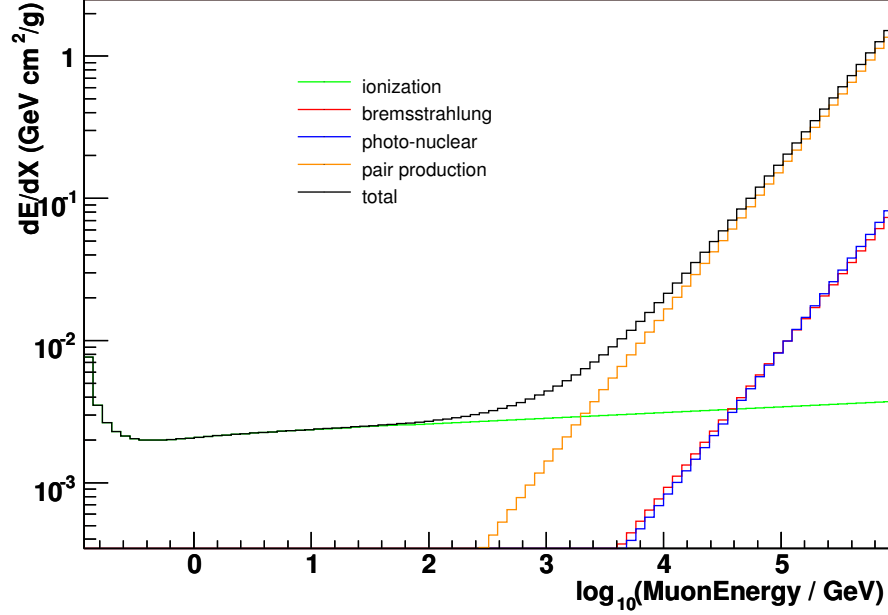


Figure 3.5: Contributions to the average rate of energy loss for muons in ice. Above IceCube’s energy threshold, Ionization losses increase slowly with muon energy. Stochastic energy losses, which dominate above  $\sim 1$  TeV, are proportional to muon energy. Figure from [67].

which are shown as functions of depth and light wavelength in Figure 3.6. More recently, ongoing studies using the LED flashers have indicated a small dependence on light propagation direction [70], but the anisotropy is not accounted for in this experiment.

In the instrumented region, the absorption and scattering lengths are well-correlated with each other and are determined primarily by the dust concentration in the ice. The larger features are thought to arise from climatic changes that vary the dust concentration in air over time. The most significant feature in both the absorption and scattering profiles occurs at a depth of about 2 km, where a thick dust layer makes any light detection nearly impossible. Transient events such as volcanic emission can result in  $\sim$  mm dust layers which do not appear to impact IceCube data.

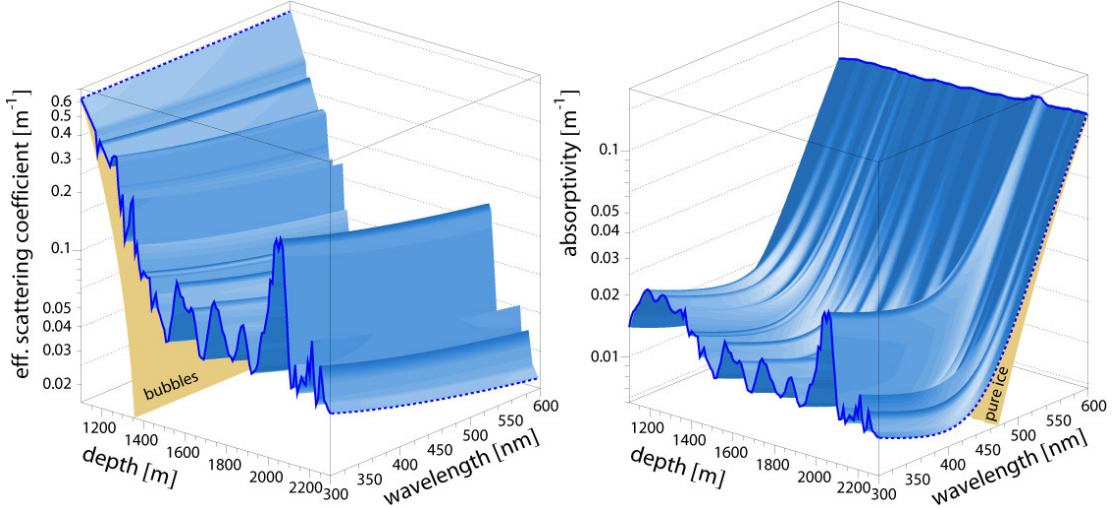


Figure 3.6: Effective scattering coefficient (left) and absorptivity (right) profiles as functions of depth and wavelength. These coefficients are the inverses of the corresponding scattering and absorption lengths. Figure from [68].

## 3.2 Optical Sensors

IceCube consists of 5160 PMTs housed along with readout electronics and calibration LEDs in glass pressure vessels called Digital Optical Modules (DOMs). The DOMs are mounted on 86 vertical strings with each string holding 60 DOMs. Each string was originally lowered into a column of water produced by a hot water drill, with the local ice later refreezing to produce a narrow column of “hole ice”. Deployment took place during the Austral summers of 2004-2005 through 2010-2011, resulting at the end of each construction season in IceCube configurations with 1, 9, 22, 40, 59, 79, and finally 86 strings. Figure 3.7 shows the layout of the detector at the conclusion of each deployment season. Data was taken during construction using the partial detector configurations. In this experiment, we perform the first search for a neutrino signal from GRBs using two new years of data: first year of 86 string operation, IC86-1, and one year using the IC79 configuration. The new dataset is added to the IC40 and IC59 datasets to obtain combined four-year results.

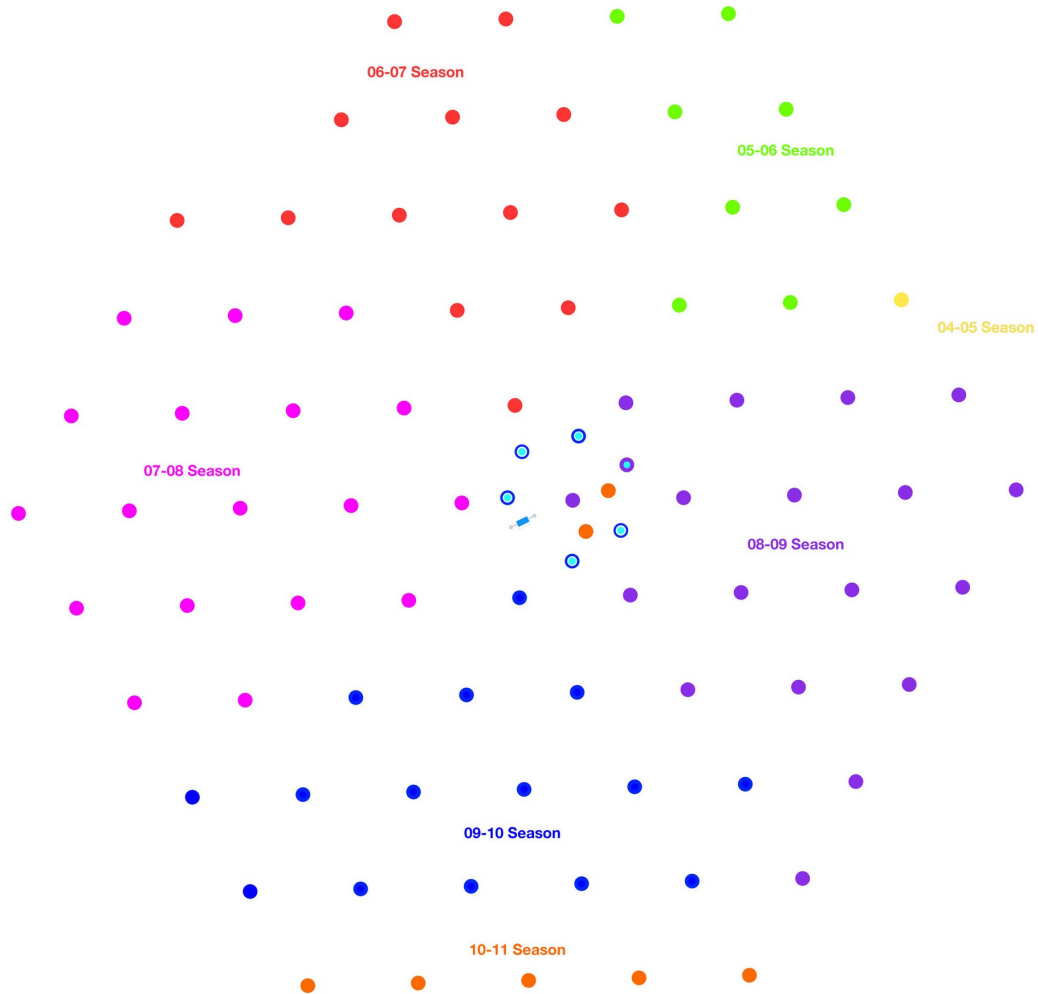


Figure 3.7: Detector layout after each deployment season. This work is the first search for neutrinos from GRBs using the nearly complete IC79 configuration (all but the orange strings) and one year of data from the completed detector, IC86-1.



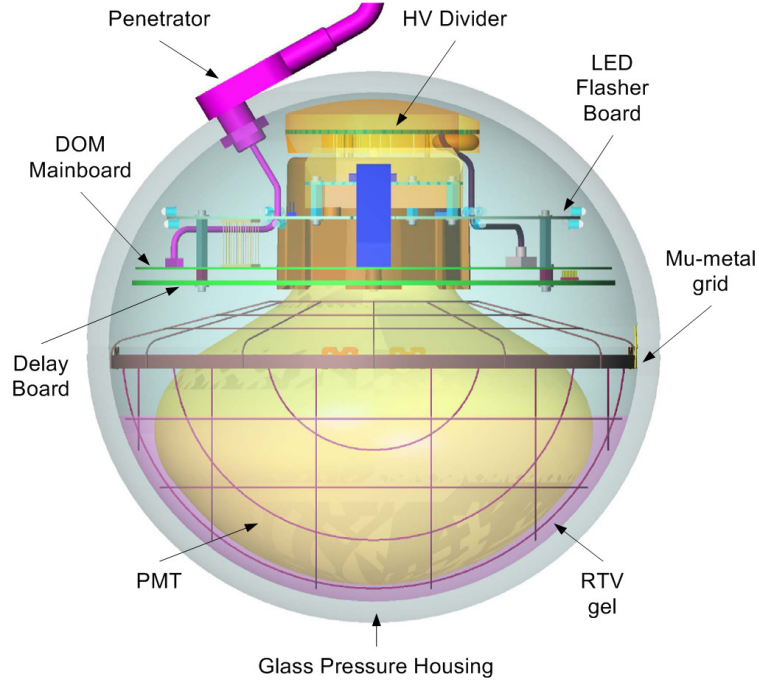


Figure 3.8: Schematic view of a DOM. Figure from [72].

The completed detector includes 78 strings on which DOMs are 17 m apart and which are laid out on a hexagonal grid, each 125 m from their nearest neighbors. The remaining strings comprise a denser infill sub-detector called DeepCore located in the center of the grid and in the deepest ice. On these strings, DOMs are only 7 m apart. The IceCube Laboratory (ICL), located in the center of the detector’s footprint at the surface, communicates with and powers the DOMs by cable. Below, we discuss the details of DOM operation and the calibration of the detector.

### 3.2.1 Contents and Operation

A schematic of the DOM is shown in Figure 3.8. Each DOM’s instrumentation and digitization hardware is housed inside a glass pressure vessel built to withstand the extreme conditions in the deepest ice: pressures up to 650 atm dur-

ing freeze-in and 300 atm after freeze-in. IceCube DOMs collect Cherenkov light using 10 inch Hamamatsu PMTs which are discussed in detail in [73]. The PMT consists of a photo-cathode for collecting individual photons, a series of dynode plates held at increasingly high voltages, and finally an anode. The cathode is coupled to the pressure vessel with optical gel. When a photon is incident upon the photo-cathode and ejects an electron, this electron is referred to as a photoelectron (PE). The strong electric field causes the electron to accelerate towards the first dynode, where it ejects many electrons. Each of these is accelerated towards the next dynode, and the process continues until a total of  $\sim 10^7$  electrons arrive at the anode. The PMT is encased by a mu-metal grid to reduce the curvature of electron paths in the PMT by Earth's magnetic field. The quantum efficiency (QE) refers to the probability of an incident photon producing a PE. IceCube's PMTs are sensitive to wavelengths of 300–600 nm, with a peak QE of 25% for incident light with a wavelength of 420 nm. The Cherenkov light spectrum is inversely proportional to wavelength, so the intensity is a factor of two larger at the small wavelength cutoff than at the large wavelength threshold.

A transformer is used to couple the anode of the PMT to the DOM mainboard, which is responsible for waveform digitization and other tasks. A block diagram of the mainboard, which is described in detail in [74], is shown in Figure 3.9. A commercial digitizer called the Fast Analog to Digital Converter (FADC) records the PMT waveform at a rate of 40 MHz. For better timing precision and dynamic range, a second type of digitizer, the Analog Transient Waveform Digitizer (ATWD), is used. The ATWD can sample at a rate of 300 MHz, but only for 422 ns, after which it requires 29  $\mu$ s to digitize and clear. To reduce dead time during digitization, two ATWDs are used in alternation. Two pulses in rapid succession can be digitized simultaneously; in rare cases where three or more pulses occur within 29  $\mu$ s, the first two are saved and others are lost.

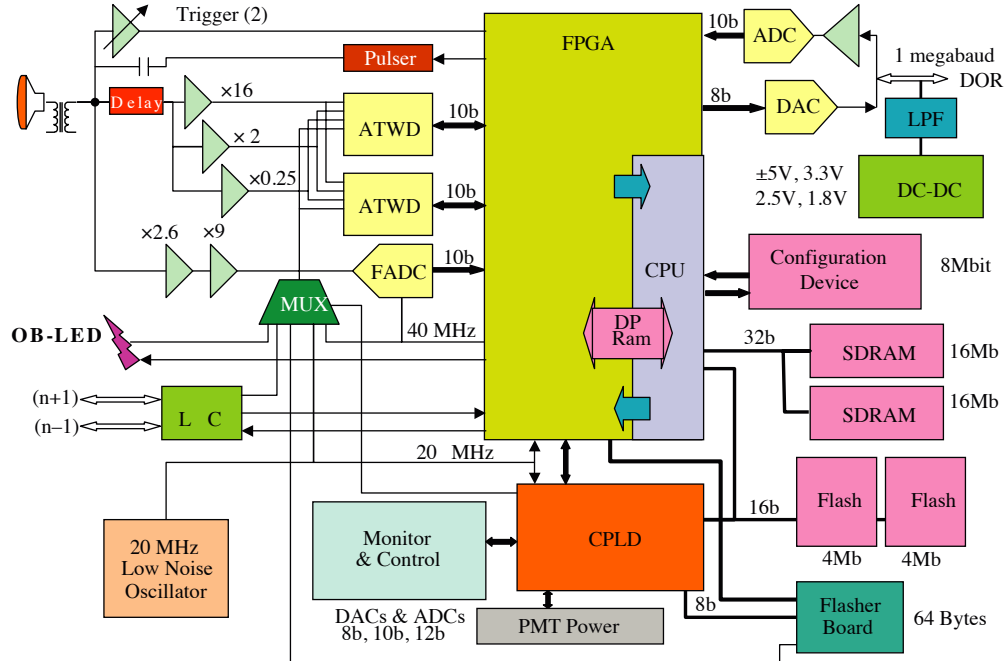


Figure 3.9: Block diagram of the DOM mainboard. The PMT, FADC and ATWDs, CPU and FPGA, 20 MHz clock, flasher board, and supporting electronics are shown. Figure from [74].

The three data-taking channels on the ATWD have decreasing gains of 16, 2 and 0.25. When a readout is performed, all saturated channels and the highest-gain non-saturated channel are recorded. A fourth channel on the ATWD can receive various calibration signals.

Each DOM sends data to the data acquisition system at the surface any time the FADC detects a signal above 0.25 PE. This is referred to as a launch. To reduce the noise data rate and the ATWD dead time, full FADC and ATWD waveforms are only recorded if one of the launching DOM's four nearest neighbors also has a launch within  $1 \mu\text{s}$ . This condition, observed locally using inter-DOM communication, is referred to as Hard Local Coincidence (HLC). When a DOM launches but HLC does not occur, it is referred to as Soft Local Coincidence (SLC). In this case, the DOM sends only the three FADC samples corresponding to the highest amplitude 75 ns of the waveform.

Launching and communication are coordinated by an on-board CPU that communicates with the other electronics through a Field-Programmable Gate Array (FPGA). Other notable hardware includes a 20 MHz oscillator for precision time-keeping and an LED flasher board used for calibration. Each DOM communicates with its neighbors and to the surface using cables entering the pressure vessel through a “penetrator” carefully designed not to disturb the pressure-resistant properties of the glass sphere as well as to maintain a water-tight seal during freeze-in.

### 3.2.2 Calibration

IceCube’s performance is contingent upon many steps of careful calibration. Timing and signal response calibration is required for obtaining self-consistent waveforms that can be used to reconstruct the physical pulses that occurred in the PMT. Geometry calibration, along with timing calibration, is crucial for obtaining the best possible reconstructions of particles passing through the instrumented volume. The calibration procedures used in IceCube are discussed below.

#### 3.2.2.1 Timing Calibration

IceCube reconstruction demands extremely precise timing calibration. DOMs keep time using a 20 MHz free-running oscillator. In order to effectively synchronize all 5160 of these clocks, a GPS-disciplined rubidium clock in the ICL provides a master IceCube Time (ICT). Once per second, a Reciprocal Active Pulsing calibration (RAPcal) procedure [74] is used to measure each DOM’s clock offset and drift rate with respect to ICT. The timing calibration begins with a 5 ns pulse transmitted from the ICL. The waveform, which is subject to dispersion in transit, is digitized in the DOM. After a fixed delay  $\delta$ , an identical 5 ns pulse is returned by the DOM and digitized in the ICL. Then the DOM transmits its

timestamp for the arrival of the RAPcal pulse along with the digitized waveform. Because reciprocal hardware is used, the returned waveform digitized in the ICL is identical, within component tolerance, to the one recorded in the DOM. By comparing the two waveforms, the RAPcal system can latch onto the same part of each waveform and directly compare ICT to the DOM time.

The ratio of time intervals between sending consecutive RAPcal pulses,  $\Delta T_{\text{ICT}}$ , and receiving them,  $\Delta T_{\text{DOM}}$ , gives the ratio of ICT and DOM clock rates:  $\nu_{\text{DOM}}/\nu_{\text{ICT}} = \Delta T_{\text{DOM}}/\Delta T_{\text{ICT}}$ . Using the round-trip time  $\rho$  between the initial RAPcal pulse and the receipt of the return pulse, the cable transit time  $\tau = \frac{1}{2}(\rho - \delta)$  is found. Then the DOM clock offset with respect to ICT is given by  $(T_{\text{DOM}} - \tau) - T_{\text{ICT}}$ . This offset varies slowly due to the drift of the DOM's local oscillator. During data taking, timestamps sent by DOM's are converted to ICT using an offset extrapolated from the previous two RAPcal offset calculations.

The sampling rate of the ATWDs is 300 MHz — faster than the 20 MHz clock. When a launch occurs, the ATWD time binning is aligned with the clock and thus with the FADC. The precise sample timing is calibrated by using the fourth channel to digitize the sinusoidal clock signal. This calibration is subject to further correction using the clock frequency ratio found above.

The master ICT is disciplined by GPS and is accurate within  $\pm 10$  ns [74]. Thus timing errors are very small compared to the rotation period of the Earth, making it possible to study astrophysical point sources — even fast transients such as GRBs.

### 3.2.2.2 Signal Response Calibration

The PMT and digitizer responses are calibrated periodically by a program called DOMcal which runs on the DOMs' CPUs. For early detector configurations, this was done monthly, but it has since been found that annual DOMcal runs are

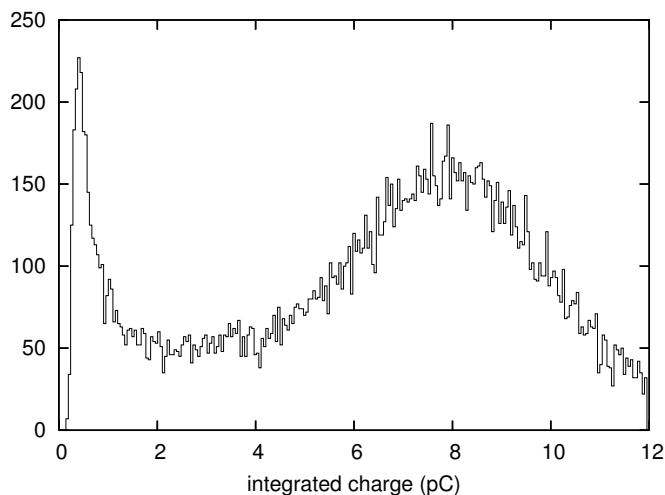


Figure 3.10: A typical DOMcal charge distribution. The peak near zero corresponds to the noise floor. The broader peak near 8 pC gives the SPE charge.

sufficient. A variable-voltage pulser on each DOM mainboard produces a PMT-like calibration pulse. The pulser itself is calibrated by finding the smallest voltage which triggers the discriminator. Once the pulser voltage is calibrated, it is used to find the mapping from input voltage to output 10-bit integer for each of the 128 bins on each channel of each ATWD. The pulser is also used to measure more precisely the gain of each ATWD channel (where the nominal gains are 16, 2 and 0.25). DOMcal is also responsible for the ATWD sampling frequency calibration mentioned in Section 3.2.2.1. During subsequent data-taking, the per-bin calibration is applied not in the DOM but rather as a step during data mass processing.

The response of the PMT itself is then characterized using individual photoelectron events. A typical charge distribution is shown in Figure 3.10. The sharp peak at low charge gives the noise pedestal. The broader peak is the single photoelectron (SPE) charge. This is done for various PMT high voltage settings. For normal operation, the high voltage is adjusted to ensure that the SPE peak corresponds to a gain of  $10^7$ .

### 3.2.2.3 Geometry Calibration

The baseline geometry is determined during deployment. Pressure sensors just above the uppermost and below the lowermost DOMs on a string are used to measure the depths of those points with respect to the water line near the surface. The distance between each DOM is measured as the string is lowered into the hole. Drill position data and conventional surveys of hole locations are used to constrain the horizontal degrees of freedom. These initial conditions give the location of each DOM within 0.5 m. Later, special flasher runs are performed in which some onboard LEDs flash and are observed by other nearby DOMs. The resulting ensemble of transmit-receive time interval measurements is used in a global fit, with the initial survey locations taken as a seed, in order to further constrain the relative positions of the DOMs.

## 3.3 Data Acquisition

Under normal, stable operation, HLC and SLC readouts are constantly being transmitted to the surface. IceCube uses a detector-global data acquisition system to identify potential physics events — i.e., observations of Cherenkov light as opposed to PMT noise — and to prepare event data for initial processing and transmission to the north.

### 3.3.1 Trigger

When DOMs enter an HLC or SLC state, they autonomously transmit waveform data to a DOMHub computer in the ICL. Each DOMHub communicates with and supplies power to one string of DOMs. The Data Acquisition system (DAQ) monitors launches on all DOMHubs, waiting for any of several of conditions that trigger the construction of an IceCube event. This experiment relies on events

passing a simple multiplicity trigger (SMT). Specifically, we use the SMT-8 trigger, which occurs when eight HLC launches are received during a  $5\ \mu\text{s}$  window. The trigger window slides, and any overlapping trigger windows (including those from different triggers designed to target other signal types) coalesce into a single event. The event also includes data from the  $4\ \mu\text{s}$  before and  $6\ \mu\text{s}$  after the time during which at least one trigger condition was met. After  $6\ \mu\text{s}$  during which no trigger condition is satisfied, the event data is finalized, packaged into a data bundle called a *frame*, and sent to the Processing and Filtering (PnF) system.

### 3.3.2 Processing and Filtering

Even with an overburden of 1.4 km of ice, the large downgoing cosmic ray-induced muon flux causes IceCube's SMT-8 to trigger at a rate of over 2 kHz. While the full dataset is useful for certain analyses, the bandwidth available on NASA's satellites requires that full event data is only sent to the North for a subset of events. Therefore, a series of processing and filtering (PnF) steps are performed first at the Pole and then further in the North. Event reconstruction methods applied in processing will be discussed in detail in Chapter 4, and the use of reconstructed quantities to reject backgrounds will be discussed in Chapter 5. In this section, we discuss the operational aspects of the PnF system.

Each event frame produced by the DAQ is subjected to a set of computationally straightforward initial reconstructions such as an energy proxy consisting of the summed charge recorded in the DOMs and an angular reconstruction that assumes that the trigger was produced by a muon track. Parameters such as reconstructed trajectory, quality of reconstruction, and total collected charge are used to select events that are most likely to be useful in physics analyses. Several filters are in use, each with different physics goals. For events that pass at



least one filter, full waveforms<sup>1</sup> and initial reconstruction results are sent to the North. For remaining events, only the reconstruction results are sent. Because the same scripts are run for every event, the PnF system distributes processing across a cluster of computing nodes in the ICL. When computing nodes finish processing an event, the event is pushed into a buffer that time orders them before compressing the data for upload.

Full waveform data is written to tape in the ICL for every trigger regardless of filter results. The tape backups are shipped annually to the northern hemisphere for storage. If a serious online processing flaw is discovered, the data can be recovered from these tapes. However, to date this contingency plan has never been used.

All datasets used in this experiment require events to pass the muon filter, which reduces the data rate to 30 Hz. This filter targets high energy downgoing muons and potentially well-reconstructed upgoing muons. A relatively small ( $\sim 4$  Hz) data stream of the most likely neutrino candidates in that sample is selected by the Online Level 2 filter. These events receive more advanced reconstructions that yield enough information to select a high-purity neutrino-induced upgoing muon sample online. The acceptance of this stream is limited by the availability of CPU time on the processing cluster and the constraint that events requiring more than 30 s to reach the time-ordering buffer must be extremely rare. While the Online Level 2 filter was originally designed for low-latency follow-up of multiplets (spatially and temporally coincident neutrino events), it was also found to be suitable as a starting point for the IC86-1 GRB search.

After the data arrive in the North, a series of “offline” mass processing steps take place. The so-called Offline Level 2 repeats the basic processing chain

---

<sup>1</sup>More recently, a data compression scheme was introduced. Each waveform is fit as a sum of pulse templates; if the fit is good, then only the pulse time and amplitude parameters are transmitted.

used at the South Pole, but because more computing resources are available, some reconstructions are added or are performed with more seed iterations. Muon-based analyses can take advantage of Muon Level 3, an additional processing pass which reduces the data rate to about 1 Hz before performing additional CPU-intensive reconstructions. This was the starting point for the IC79 GRB search.

### 3.3.3 Experiment Control and Monitoring

Under stable operation, the detector divides data into eight hour runs, with data stored in  $\sim 130$  files per run. All filtered data is transferred to servers in the northern hemisphere. Satellite bandwidth is available for a fraction of each day, and barring problems with satellite connectivity, data arrive with a typical latency of  $\lesssim 1$  day.

Detector run information is stored in an internal database called IceCube Live. Various statistics such as run status, duration and event count are available at a glance on its web interface. A more detailed monitoring system embedded in IceCube Live allows the detector to be monitored more thoroughly. The stability of the array as a whole is ensured by careful examination of the continuity of trigger and filter rates. Maps of per-DOM launch rates and other parameters are used to identify new or recurring issues with individual DOMs. The monitoring system ensures that any operational problems are corrected quickly. Knowledge of verified stable operation is ultimately synthesized into a “good run list”, which enumerates runs that are thought to be reliable and stable for physics analysis. Calibration runs or runs in which unforeseen issues are found are not included in the good run list. Occasionally a run is excluded from this list but is still adequate for certain analyses, such as those of transients like GRBs. For example, if a GRB occurs during a run and, later, a power outage causes several DOMHubs to crash, the detector cannot be considered stable throughout the run but the

data obtained during the GRB is valid for a GRB-neutrino coincidence search. Such runs are carefully reintroduced into analyses when possible.

Most day-to-day detector operation is managed by specially trained personnel temporarily living at the South Pole station. The winterovers, so-called because they stay for a full year including the dark Austral winter, respond to various issues such as crashed computing nodes or failing runs. Sometimes remote login is sufficient to resolve problems; other times hands-on work in the ICL is required.

## Chapter 4: Event Processing

The pipeline from detector data to physical results can be divided into two overarching steps: processing and analysis. Processing, which was introduced in the previous chapter, distills raw data into physical quantities. For a muon track search, this involves reconstructing the originating angle and energy of the muon and providing proxies for the quality of the angular reconstruction. The properties of the muon are needed for the association of any particular event with a GRB. Quality parameters are used to reject the misreconstructed downgoing cosmic ray-induced muons that dominate the IceCube filter rate. Analysis consists of the interpretation of the ensemble of events and will be discussed in detail in later chapters. Here, we describe the processing chain, charting the route from individual DOM readouts to bundles of muon track properties suitable for analysis. Then we describe the generation of simulated datasets representing possible signals and known cosmic ray-induced backgrounds.

### 4.1 Pulse Series Construction

The raw digitized waveforms provided by the FADC and ATWD chips are not immediately useful for testing muon trajectory and energy hypotheses. Instead, the arrival times of photons incident on the photocathode are reconstructed first. This intermediate step produces a series of reconstructed pulses, each of which is parameterized as a time and a number of PEs, for each stable DOM that includes at least one launch within the trigger window. Then subsequent reconstructions of the properties of a muon can be framed much more simply in terms of the likelihood of observing PEs at given locations and times, rather than in terms of the likelihood of producing the complex and extremely detailed observed digitized waveforms.

### 4.1.1 DOM Cleaning

Some DOMs do not participate in reconstruction due to various hardware-related issues. Poor communication with the surface, power-up failures, or high-current problems can cause a DOM to be marked as bad. Broken local coincidence connections can lead to DOMs that are bad for HLC launches but usable for SLC launches. Sometimes DOMs are found to be bad during operation, but more commonly they are bad ever since deployment. Occasionally, technicians are able to recover DOMs remotely so they can begin or resume data-taking. For IC86-1,  $\sim 100$  DOMs ( $\sim 2\%$  of the array) were marked bad for HLC launches, but  $\sim 20$  of these could still produce SLC launches. All data from marked bad DOMs is masked prior to pulse reconstruction.

### 4.1.2 Waveform Calibration

Raw waveforms from remaining DOMs are used to calculate calibrated waveforms. The first step is to subtract the per-bin baseline ADC counts corresponding to zero input voltage. Baselines are measured by forcing DOM launches and averaging the ADC counts for many waveforms, excluding any waveforms consistent with the presence of a pulse within the readout window. Physics waveforms are normalized in units of mV by multiplying baseline-subtracted counts by the per-bin gains measured by DOMCal. Then the start times of the waveforms are calculated by correcting for the average transit time of a pulse through the PMT and the different delays introduced by the electronics that precede the FADC and ATWDs. Lastly, since the transformer that couples the PMT to the mainboard acts as a high-pass filter, it introduces droop in the trailing edge of the waveform. A temperature-dependent model of the reaction of the toroid in the transformer is used to correct for this effect in each time bin.

### 4.1.3 Waveform Fitting

An algorithm called `wavedeform` [75] is used to unfold calibrated waveforms into series of reconstructed pulses. The shapes of the calibrated waveforms are dominated by the shaping functions of the front-end amplifiers (Figure 4.1). The shaping functions are therefore used as templates to form a basis for decomposing the waveforms. The pulse amplitudes and times of arrival are found by finding a set of pulses that combine linearly to provide a good fit to the FADC and the three ATWD channels simultaneously.

Fitting by interference — adding large positive and negative pulses together — would yield unphysical PE counts. `Wavedeform` avoids this problem by using a Non-Negative Least Squares algorithm in which all coefficients must be positive. In particular, the Lawson-Hanson algorithm [76] is used. The structure of this algorithm also provides a useful mechanism for avoiding overfitting using a large number of small pulses. In each iteration, only one pulse is added: the one which most reduces the error of the fit. The algorithm naturally terminates when adding a positive pulse at any time bin would increase the fit error. In the IceCube processing chain, the fit is terminated early by requiring that the error reduction from adding an additional pulse must be better than a certain threshold. This provides a good balance between representing waveform data well and allowing a physical interpretation of the reconstructed pulses.

### 4.1.4 Pulse Series Cleaning

When the DAQ triggers, there is a window of at least  $10\ \mu\text{s}$  during which all HLC and SLC readouts are stored. This results in the inclusion of unrelated noise readouts which can reduce the quality of particle reconstructions. Therefore, the pulse series produced by `wavedeform` are subject to a cleaning step which tries to eliminate irrelevant noise readouts. For IC79, this was done by retaining only the

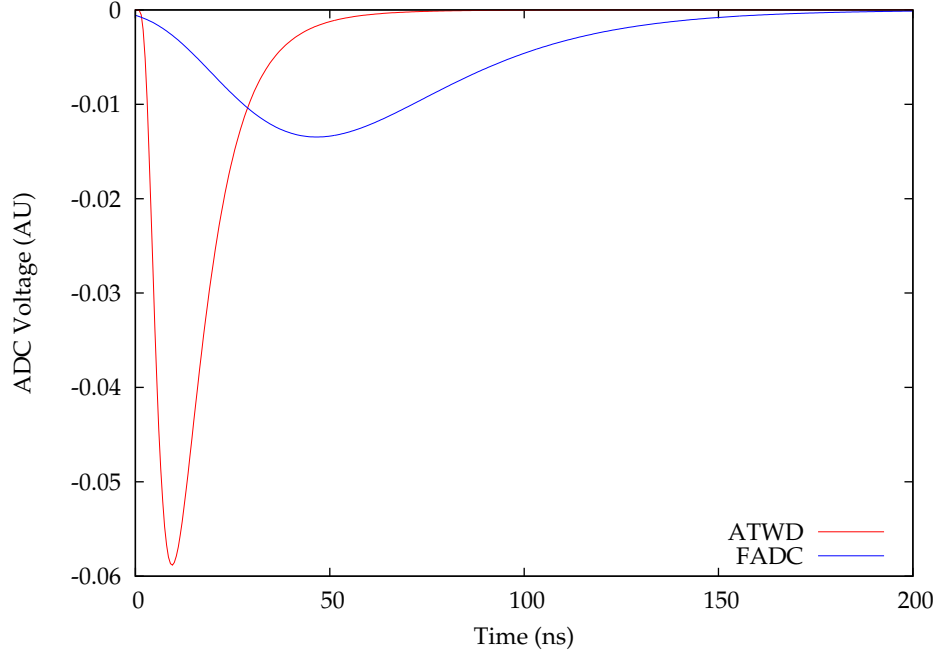


Figure 4.1: ATWD and FADC shaping functions. PMT pulses are elongated to ensure that each pulse covers several digitizer bins. The signal is widened more for the FADC because of its lower sampling rate. The highest-gain ATWD channel is represented here; there are small difference for lower-gain ATWD due to differences in the amplifier chains.

$6\ \mu\text{s}$  of data containing the largest number of pulses. In IC86-1, a more sophisticated approach was used based on the  $r$ - $t$  causality condition. This condition is satisfied if a pulse is within 150 m and  $1\ \mu\text{s}$  of another. In the seeded  $r$ - $t$  cleaning algorithm, only HLC pulses satisfying the  $r$ - $t$  condition with other HLC pulses serve as a seed and are certain to be kept. Then other pulses (either HLC or SLC) are considered in three iterations in which pulses are added to the kept set if they satisfy the  $r$ - $t$  condition with another pulse that is already in the kept set at the start of the iteration.

## 4.2 Reconstruction algorithms

Armed with pulse series for each DOM contributing data for an event, a series of angular reconstructions are performed using increasingly realistic models of Cherenkov light propagation. Angular reconstructions make use of only the earliest reconstructed pulse time since it is assumed that any later pulses must have been delayed by scattering. More realistic models require more processing time and are more sensitive to the seed, but they provide better angular resolution. The progression used in processing obtains good final results by allowing each reconstruction to take the previous as a seed. Modified angular reconstructions are performed to obtain parameters that can be used to reject poorly-reconstructed backgrounds such as cosmic ray muons passing near the boundary of the instrumented volume and emitting light upwards (“corner clippers”) or multiple independent muons passing through the instrumented volume at the same time (“coincident muons”). Finally, additional reconstructions are performed to estimate the uncertainty of the best angular reconstruction and the energy of the muon passing through the detector.

### 4.2.1 LineFit

The initial angular reconstruction obtains an approximate solution quickly by using the unphysical simplifying assumption that the muon produces a plane wave of light traveling in the same direction as the muon. If DOMs at positions  $\vec{r}_i$  observe first pulses (hereafter referred to as hits) at times  $t_i$ , then a least-squares fit yields the vertex  $\vec{r}$  through which the muon passes,

$$\vec{r} = \langle \vec{r}_i \rangle - \vec{v} \cdot \langle t_i \rangle, \quad (4.1)$$



and its velocity  $\vec{v}$ ,

$$\vec{v} = \frac{\langle \vec{r} \cdot t_i \rangle - \langle \vec{r}_i \rangle \cdot t_i}{\langle t_i^2 \rangle - \langle t_i \rangle^2}, \quad (4.2)$$

where angled brackets denote an average over DOMs. The LineFit speed  $v = |\vec{v}|$  is useful as a quality parameter, while the vertex location  $\vec{r}$  and the direction of  $\vec{v}$  serve as an easily calculated seed for subsequent reconstructions.

This method has recently been improved [77] using two enhancements that reduce the impact of highly scattered light. First, the fit excludes any hit for which there exists another hit at least 778 ns earlier within a radius of 156 m. Second, the fit is performed in two iterations, where the first iteration uses a Huber penalty function [78] to give less weight to hits more than 153 m from the muon location at the time of the hit. The final iteration is a standard least-squares fit as described above, but excluding hits that contributed reduced weights or were excluded in the first iteration. The numerical thresholds were tuned using simulated muon events (see Section 4.3 for simulation methods). Compared to a single least-squares fit using all available hits, the resulting ImprovedLineFit reconstruction provides a better seed for more advanced reconstructions and a better quality parameter  $v$ .

#### 4.2.2 Single Photoelectron (SPE) Fit

All more advanced angular reconstructions are based on a maximum likelihood method. If the probability of observing a hit at  $(\vec{r}_i, t_i)$  given a muon passing through vertex  $\vec{r}$  at time  $t$  with velocity  $\vec{v}$  is given by a probability distribution function (PDF)  $P(\vec{r}_i, t_i | \vec{r}, t, \vec{v})$  then the likelihood for a pattern of hits  $\{\vec{r}_i, t_i\}$  is

$$\mathcal{L}(\{\vec{r}_i, t_i\} | \vec{r}, t, \vec{v}) = \prod_i P(\vec{r}_i, t_i | \vec{r}, t, \vec{v}). \quad (4.3)$$

The most likely muon trajectory is found by minimizing the negative natural logarithm of the likelihood with respect to  $\vec{r}$ ,  $t$  and  $\vec{v}$ . However, the likelihood has a degeneracy where modifying the vertex passing time  $t$  can be compensated for by shifting  $\vec{r}$  along the direction of  $\vec{v}$ . This degeneracy is resolved by fixing the vertex passing time, assuming that  $|\vec{v}| \approx c_{\text{vacuum}}$ , and expressing the likelihood in terms of the vertex  $\vec{r}$  and an angle of incidence with zenith  $\theta$  and azimuth  $\varphi$ :

$$\mathcal{L}(\{\vec{r}_i, t_i\} | \vec{r}, \theta, \varphi) = \prod_i P(\vec{r}_i, t_i | \vec{r}, \theta, \varphi). \quad (4.4)$$

This formulation is accommodated by a module called *gulliver*, which uses a numerical minimizer to find a local optimum given a seed and a hit time PDF. For a very dense brute-force scan of the independent variables  $\vec{r}$ ,  $\theta$  and  $\varphi$ , this method is the best way to estimate the muon trajectory. Unfortunately, it has some practical drawbacks. In practice, it is too CPU-intensive to cover the entire available 5-dimensional parameter space. Instead, numerical minimizers examine the likelihood behavior in the vicinity of the seed parameters to search for a local optimum. A poor seed may prevent the minimizer from finding the global optimum. Furthermore, a detailed PDF that accounts for the measured inhomogeneous and anisotropic ice properties would be very CPU-intensive and would produce a complex likelihood space that would be difficult for numerical minimizers to navigate.

While recent work has enabled the use of detailed PDFs constructed from spline fits to the measured ice properties (still at a cost of significantly larger processing times), in this experiment we restrict ourselves to a simplified PDF derived from the Pandel function [79]. The geometric quantities involved are displayed in Figure 4.2; the Pandel function is compared with detailed simulations in Figure 4.3.

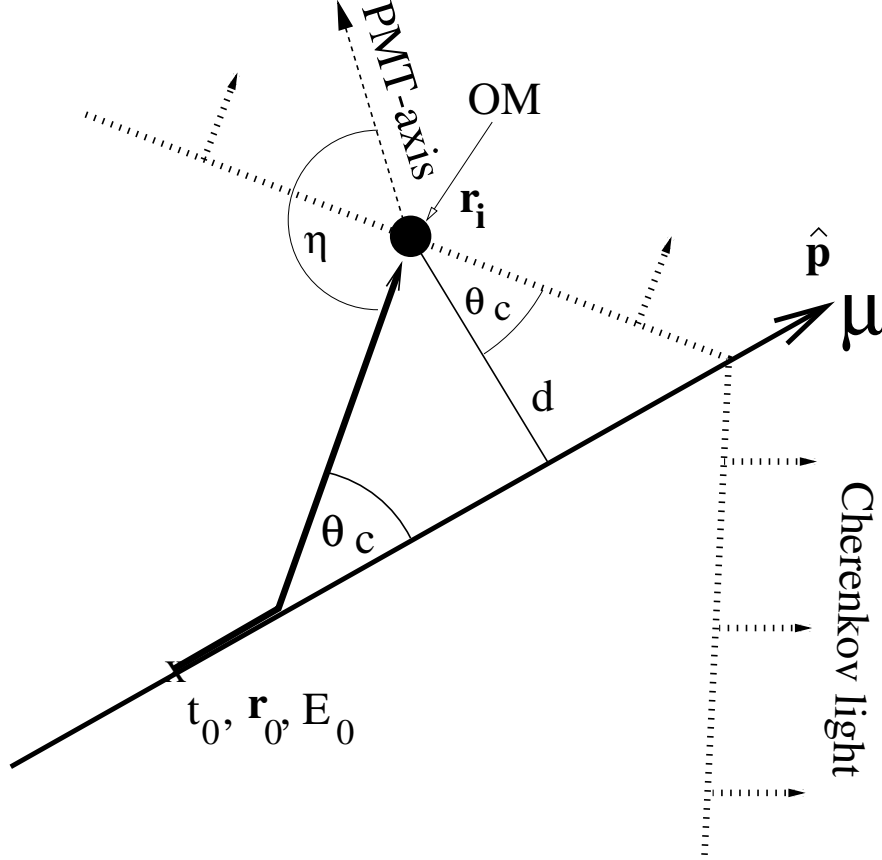


Figure 4.2: Geometry of light propagating from a muon track to a DOM. Here  $\vec{r}_0$  is the vertex position elsewhere referred to as  $\vec{r}$ ;  $\hat{p}$  is the particle momentum, which is parallel to  $\vec{v}$ ;  $\theta_C$  is the angle of Cherenkov light emission with respect to  $\vec{v}$ ; and  $d$  is the impact parameter of the muon as it passes the DOM. Figure from [80].

The Pandel function is a modified form of the gamma distribution [81] that gives the time arrival PDF for isotropic monochromatic light propagating through a dense medium. It can be expressed as

$$p_{\text{Pandel}}(\Delta t) = \frac{(\Delta t)^{d_{\text{eff}}/\lambda - 1}}{\Gamma(d_{\text{eff}}/\lambda) \left(\frac{1}{\tau} + \frac{c_{\text{medium}}}{\lambda_a}\right)^{-d_{\text{eff}}/\lambda}} \exp \left[ -\Delta t \left( \frac{1}{\tau} + \frac{c_{\text{medium}}}{\lambda_a} \right) \right]. \quad (4.5)$$

Here  $\Delta t = t_i - t_{\text{geo}}$  is the difference between the observed hit time and the time

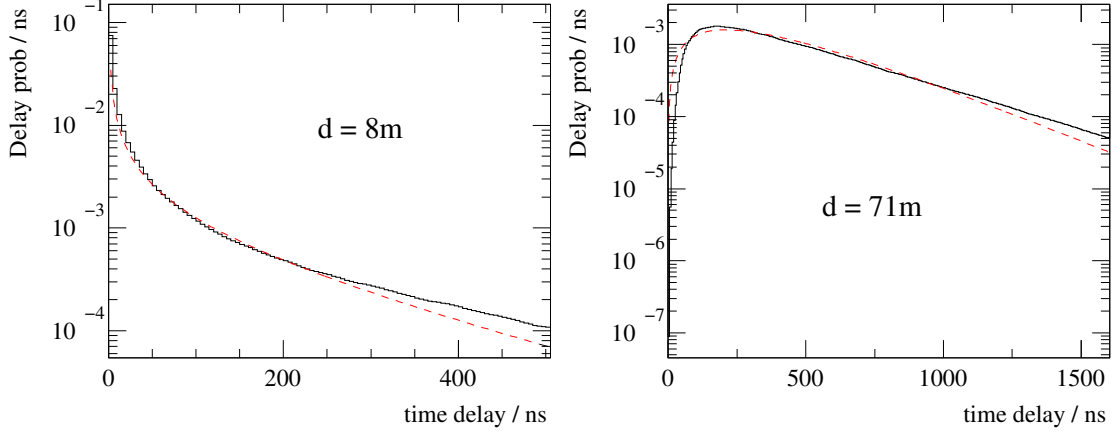


Figure 4.3: Comparison of the Pandel function (dashed curves) with detailed simulations (black curves) for tracks at two impact parameters  $d$  from a DOM. Figure from [80].

expected for an unscattered photon, which can be calculated from the geometry:

$$t_{\text{geo}} = t + \frac{|\vec{v}| \cdot (\vec{r}_i - \vec{r}) + d \cdot \tan \theta_C}{c_{\text{vacuum}}}. \quad (4.6)$$

The Pandel function makes use of the speed of light in the medium  $c_{\text{medium}}$  as well as additional numerical parameters  $\lambda_a = 98$  m,  $\lambda = 33.3$  m and  $\tau = 557$  ns. It also uses an empirical effective impact parameter that accounts for the relative effect of scattering depending the angle  $\eta$  between the unscattered light path and the PMT axis:

$$d_{\text{eff}} = a_0 + a_1 d, \quad (4.7)$$

$$a_0/[\text{m}] = 3.1 - 3.9 \cos(\eta) + 4.6 \cos^2(\eta), \quad (4.8)$$

$$a_1 = 0.84. \quad (4.9)$$

For delayed Cherenkov photons, the Pandel function is a good approximation. However, it has two problems for numerical evaluation. It has a pole at  $\Delta t = 0$  for small impact parameters  $d$ , and it is zero for  $\Delta t < 0$ . The former represents a

completely unscattered photon. The latter occurs for early noise hits that survived pulse cleaning or for physical hits that fluctuate to earlier time due to PMT timing jitter. These problems are addressed by convolving  $p_{\text{Pandel}}(\Delta t)$  with a Gaussian with a width chosen to produce the best reconstructions by accounting for both PMT jitter and the slightly early noise hits which are most likely to survive pulse cleaning.

The single PE (SPE) reconstruction is evaluated by finding the vertex  $\vec{r}$  and angle of incidence  $\theta, \varphi$  that maximize the likelihood (4.4) for the Gaussian-smoothed Pandel PDF given the observed hits. This setup includes a bias due to the use of the earliest photons with a PDF that was constructed to describe any random photon. Nevertheless, SPE provides better angular resolution than LineFit, and it provides a way of comparing results for different seeds. To guard against the possibility that a poor seed was provided by LineFit, several iterations of SPE are performed in which the vertex is fixed but the angle of incidence is varied significantly throughout the sky. The result is saved for the iteration yielding the best likelihood, and it becomes the seed for the multiple PE fit.

### 4.2.3 Multiple Photoelectron (MPE) Fit

The reconstruction based on the Pandel PDF can be improved by correcting for the biased choice to fit using the first pulse. For each DOM, the PDF is modified according to the total charge  $n_{\text{PE}}$  observed by that DOM:

$$p_{\text{MPE}}(\Delta t) = n_{\text{PE}} \cdot p_{\text{SPE}}(\Delta t) \cdot \left[ \int_{\Delta t}^{\infty} p_{\text{SPE}}(t') dt' \right]^{n_{\text{PE}}-1}. \quad (4.10)$$

The integral in (4.10) has the potential to make this reconstruction prohibitively expensive computationally, but fortunately some good approximations [82, 83] make the multiple PE fit (MPE) tractable for mass processing. The added com-

plexity makes the behavior of the likelihood more variable than SPE, so the MPE result rarely is far from that of SPE. Therefore, when SPE is far from correct, MPE usually does not help. However, because the MPE PDF is closer to physically correct, MPE tends to improve the reconstruction when SPE does provide a good seed. MPE is the most accurate reconstruction available in the processed datasets used for this experiment.

#### 4.2.4 Angular Error Reconstruction

In past work [6, 7], the angular error was estimated by evaluating the MPE likelihood in a  $4^\circ \times 4^\circ$  grid around the MPE result and fitting a paraboloid to the optimum. The width of the paraboloid implied the approximate per-event angular uncertainty. For this experiment, however, the IC86-1 dataset was the first to be analyzed. To facilitate a relatively early unblinding of the data and in anticipation of a future near-realtime search, only online reconstructions were used. This required the use of a less CPU-intensive, though less accurate, angular error estimator. For consistency, the same fast estimator was used with the IC79 dataset.

The Cramer-Rao relation gives a lower bound on the true resolution based on the behavior of the per-DOM PDFs near the final fit result. Specifically, it relates the covariance of each track parameter to the inverted Fisher information matrix:

$$\text{cov}(\mu_m, \mu_k) \geq I(\vec{\mu})^{-1}, \quad (4.11)$$

where  $\vec{\mu}$  represents the five independent track parameters:  $x$ ,  $y$  and  $z$  of the vertex plus  $\theta$  and  $\varphi$  of the reconstructed direction. The Fisher information matrix is given

by

$$I_{mk}(\vec{\mu}) = - \left\langle \left[ \sum_i \frac{\partial^2}{\partial \mu_k \partial \mu_m} \right] \ln p(\Delta t_i | \vec{\mu}) \right\rangle, \quad (4.12)$$

where the  $i$  represents each hit DOM,  $p(\Delta t_i | \vec{\mu})$  is the Pandel-based MPE PDF, and the angle brackets indicate an average over possible values of  $\Delta t_i$ , weighted by  $p(\Delta t_i | \vec{\mu})$ . We are specifically interested in the Cramer-Rao variances  $\sigma_\theta^{CR} = \sqrt{(I^{-1})_{\theta\theta}}$  and  $\sigma_\varphi^{CR} = \sqrt{(I^{-1})_{\varphi\varphi}}$ . We ultimately use a circularized per-event error given by

$$\sigma_\nu = \frac{1}{\sqrt{2}} \sqrt{(\sigma_\theta^{CR})^2 + (\sigma_\varphi^{CR})^2 \sin^2 \theta_{\text{MPE}}}. \quad (4.13)$$

Formally, the Cramer-Rao relation holds when the sum in (4.12) is over all DOMs, weighted by the probability of obtaining a hit. However, the implementation used in IceCube simply sums over hit DOMs. Empirically, it was found that this method produces a per-event error estimator with comparable performance to the paraboloid estimate.

#### 4.2.5 Bayesian Up/Down Fit

Additional angular reconstructions are performed to obtain useful background-rejection parameters. The first of these is the Bayesian up/down fit. We know that IceCube triggers at 2.2 kHz due to downgoing cosmic ray muons; after several steps of background rejection, only  $\lesssim 4$  mHz of northern hemisphere atmospheric muon neutrinos remain. Therefore, before examining detailed event data there is strong *prior knowledge* that any given event is very likely to be downgoing. The

Bayesian reconstruction biases the likelihood using a zenith-dependent prior,

$$p(\theta) = A_0(\cos \theta)^{A_1} \exp\left(-\frac{A_2}{\cos \theta}\right), \quad (4.14)$$

where the numerical constants  $A_0 = 2.39655 \times 10^{-7}$ ,  $A_1 = 1.67721$  and  $A_2 = 0.778393$  were fit to the observed distribution of downgoing muons and  $p(\theta) = 0$  in the northern hemisphere. For well-reconstructed upgoing events, forcing a downgoing reconstruction gives a smaller log-likelihood than an unbiased reconstruction. For poorly-reconstructed downgoing events that are initially misreconstructed as upgoing, the biased reconstruction may have a similar likelihood value. Therefore, the Bayesian log-likelihood ratio is useful for rejecting misreconstructed downgoing muons.

Best results are obtained when the delay time PDF matches in the unbiased and biased reconstructions. For IC79, this required four iterations of the biased and unbiased SPE reconstructions. For IC86-1, the online reconstructions only included 2 iterations of each.

#### 4.2.6 Split Reconstructions

Another strategy for rejecting poor reconstructions, especially for coincident muons, is to split the observed hits into two groups and repeat the reconstruction. Here we make use of two splits. First, the hits are divided in time. The average time of per-DOM first pulses are found, and the hits are divided into early and late subseries. The second split is based on geometry. Hits are divided by a plane drawn through the center of gravity of all hits and normal to the MPE result. Then for each subseries of hits, LineFit and some iterations of SPE are performed — four iterations in the IC79 Muon Level 3 and two in the IC86 Online Level 2.



## 4.2.7 Energy Reconstruction

The energy of an incoming neutrino cannot be calculated precisely in this search because in general the location of the interaction vertex is not known. Product muons can travel several km through the ice and lose an unknown fraction of their original energy by the time they arrive at the detector. However, the energy of the muon as it passes through the detector can be estimated, providing an approximate lower bound on the neutrino energy.

In this experiment, we use a reconstruction called MuE [84] to do this calculation. As discussed in Section 3.1.1, at energies above  $\sim 1$  TeV, the muon energy is directly proportional to its rate of energy deposition via Cherenkov radiation. The estimate provided by MuE uses an empirically determined parameterization of the photon density along the reconstructed track:

$$\lambda_c = 3 \times 10^4 \text{ m}^{-1} \cdot (1.22 + 1.36 \times 10^{-3}(E/\text{GeV})). \quad (4.15)$$

The expected number of photons incident at a DOM is given by this expression along with a function describing the lateral distribution of the photons as a function of distance from the track. At small distances, it is assumed that scattering is negligible, and at large distances a diffusive approximation is used. The two limiting cases are stitched together to provide one smooth function which enters as an additional term in the modified Pandel function used for track reconstruction above. The energy-sensitive log-likelihood is then maximized again, taking the muon energy  $E$  to be the independent variable. The best-fit value is taken as a proxy for the neutrino energy in the unbinned likelihood analysis as described in Section 6.1.3.

## 4.3 Simulation

Experimental data from a detector such as IceCube only tell part of the story. In order to interpret the data, we need to know what we would *expect* the various backgrounds and potential signals to look like. Neutrino and cosmic ray simulations generate data in the same format as actual experimental data so that analyzers can optimize their methods and interpret their results. Most effects pertaining to particle simulation are probabilistic. Therefore, we use Monte Carlo simulation to produce datasets that are representative of possible signals and known backgrounds.

### 4.3.1 Neutrino Simulation

Neutrino simulation is used to study both known atmospheric neutrino backgrounds and potential astrophysical signals. The simulation chain begins with a software package called neutrino-generator which is based on another package called ANIS [85]. The program makes use of neutrino-nucleon interaction cross sections, shown for muon neutrinos in Figure 4.4, from CTEQ5 [86]. It assumes that the Earth can be represented by the Preliminary Reference Earth Model [87], shown in Figure 4.5. Because the cross section is small, it is most efficient to assume a neutrino origin on the Earth’s surface and an interaction vertex in or near the detector and then to determine the probability of such an event occurring. The cross section and Earth models are used to find this probability. They also are used to apply energy losses to the neutrino in a random but representative way as it propagates through the Earth.

Once the interaction energy is known, the interaction products are determined according the Standard Model physics of deep inelastic scattering, given the calculated neutrino energy upon arrival at the vertex. Any hadronic or elec-

tronic cascades are assumed to be point-like. Muons produce extended tracks and are discussed below in Section 4.3.3.

All calculations made with neutrino-generator datasets need to account for per-event weights that depend on the randomization parameters — dataset size, volume in which interaction vertices are chosen, etc. — and cross section-dependent effects in the Earth and ice, in addition to the neutrino spectrum that is being simulated. Neutrino-generator makes this possible using a quantity called OneWeight with units  $\text{GeV cm}^2 \text{sr}$  that encapsulates most of these effects. For a diffuse flux  $d\Phi/dE$  and total number of generated events  $n_{\text{gen}}$ , event  $i$  has a weight

$$w_i = \frac{\text{OneWeight}_i}{n_{\text{gen}}} \times \left. \frac{d\Phi}{dE} \right|_{E_i}. \quad (4.16)$$

The weight  $w_i$  has units  $s^{-1}$ , and the sum of weights for a dataset  $\sum_i w_i$  is the rate of neutrino events in Hz. The statistical error on this value is  $(\sum_i w_i^2)^{1/2}$ .

The standard weighting scheme works well for a diffuse flux from unresolved sources throughout the sky, but in this experiment we search for a signal from point sources with models that give per-GRB differential fluences  $dF/dE$  in units  $\text{GeV cm}^{-2}$ . We use the standard diffuse datasets to produce pseudo-point source datasets by selecting, for each GRB, events in a circle of radius  $\sim 11^\circ$  about the burst location and taking up a fraction  $f = 1\%$  of the sky. Then the weights are given by

$$w_i = \frac{\text{OneWeight}_i}{n_{\text{gen}}} \times \frac{1}{4\pi f_c} \times \left. \frac{dF}{dE} \right|_{E_i}. \quad (4.17)$$

Here,  $f_c$  is the corrected fraction of the sky, which is reduced for GRBs close enough to the horizon that simulated events are only available in part of the circle. For these datasets,  $\sum_i w_i$  is the predicted number of observed neutrinos. The statistical error is again  $(\sum_i w_i^2)^{1/2}$ .

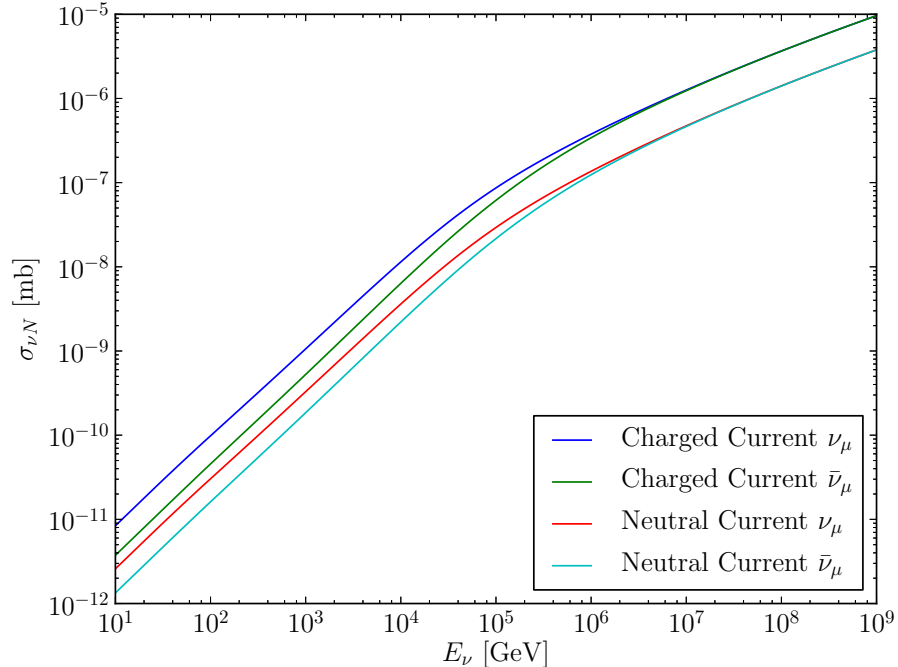


Figure 4.4: CTEQ5 [86] neutrino-nucleon cross sections for muon neutrinos as a function of neutrino energy. This analysis is only sensitive to muons produced in charged current interactions; however, all possible interactions must be accounted for in determining energy losses and the probability of absorption as the neutrino propagates through the Earth.

In this experiment we use the Honda 2006 [88] form for  $d\Phi/dE$  with (4.16) to simulate atmospheric neutrinos, while (4.17) is used to study various proposed neutrino signals from GRBs.

### 4.3.2 Cosmic-Ray Simulation

As we have seen, downgoing cosmic ray-induced muon events comprise the bulk of IceCube datasets prior to significant background rejection. This background is simulated using a software package called CORSIKA [89], which simulates cosmic rays interacting in the upper atmosphere according to the composition and energy spectrum from the Polygonato model [90] as parameterized by [91]. Its output consists of the coordinates and momenta of the resulting shower particles. In IceCube we only track the muons from these showers because no other particle

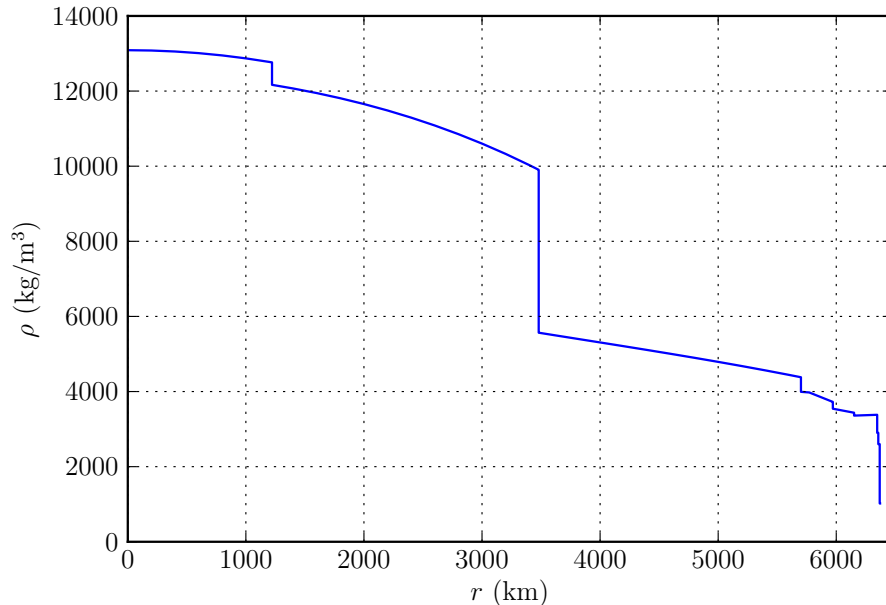


Figure 4.5: Density profile of the Earth in the Preliminary Reference Earth Model [87]. While this is the most relevant feature for neutrino propagation, the model also includes profiles for pressure, gravity and other parameters.

can reach the detector through the 1.4 km overburden of ice. The treatment of these muons is identical to the products of CC muon neutrino interactions, and is discussed below in Section 4.3.3.

In a transient coincidence analysis, off-time data (away from the time window during which the transient was active) provides a large sample for studying backgrounds even at tight cut levels. Thus, in this experiment, simulation of cosmic ray-induced muons is not crucial to understanding our results. However, because the simulation is done in the same way for cosmic ray and neutrino product muons, ensuring that cosmic ray simulation agrees reasonably well with real data provides a good check of our understanding of the detector and of our simulation methods.

### 4.3.3 Detection Simulation

A software package called Muon Monte Carlo (MMC) [67] is used to propagate muons (and, relevant to some other experiments, taus) through the ice. MMC simulates the muon energy losses discussed in Section 3.1.1. At energies relevant to this experiment, stochastic losses are dominant. The output of MMC is a series of cascades — one for each stochastic energy loss — and a finite bare muon track extent.

Because of the comparable absorption and scattering lengths in ice — both of which vary with depth and wavelength — tracking every photon resulting from a cascade or a muon track is prohibitively computationally expensive. Instead, a tool called Photonics [92] is used to tabulate photon propagation results, accounting for the depth and wavelength dependent ice properties described in Section 3.1.2, for use in simulation. For a given cascade depth, cascade direction and receiver location, Photonics level 1 tables give the expected PE rate as a function of time with respect to an un-scattered ray. Photonics level 2 tables provide this function for semi-infinite bare muon tracks originating at and terminating at each of a grid of vertex locations and track directions. Finite tracks are obtained by subtracting a track originating at the end point from a track originating at the start point. Note that the probability of a photon yielding a PE depends on photon wavelength and PMT quantum efficiency and is already accounted for in the Photonics tables.

The next step in the simulation chain is hit-maker. For each DOM, this module superimposes the Photonics PE-observation time profiles for each cascade (hadronic, electronic, or muon-stochastic) as well as for the bare muon track. The summed PE-observation profile is sampled to produce a series of hits, each of which corresponds to an integer number of PEs. Additionally, hit-maker produces pre-pulses, which are low amplitude early pulses occurring when a photon passes

through the photocathode and initiates a PMT cascade at the first dynode earlier than allowed by the PE drift velocity; late pulses, which occur when electrons reflect off the first dynode and then back off the photocathode before finally producing an ordinary but late PMT cascade; and after pulses, which are produced by atoms and molecules ionized by electrons in the PMT and which have a slower drift velocity because they are so much heavier than electrons. Hit-maker accounts for the PMT time jitter when producing hits. An additional set of hits is added by noise-generator, which simulates Poissonian noise hits.

PMT-simulator turns the series of hits into a raw PMT waveform. This is the true waveform, which is not accessible in real data. DOM-simulator is the module that folds the true waveform with the digitizer response, accounting for calibration details discussed in Section 3.2.2.2. It also tests for crossing of the discriminator launch threshold, and when a launch occurs, it tests for the HLC condition based on nearby DOMs.

From this point on, waveform data is treated analogously to real data. Trigger-sim receives full waveforms for HLC launches and three FADC bins for SLC launches. Triggering logic is applied exactly as it is in the online systems, and the result is event data frames that can be used just like real experimental data. Unlike experimental data, however, simulation data includes information about the true properties of simulated particles. This allows for the estimation of many important performance metrics such as angular resolution, energy resolution, and effective area.

## Chapter 5: Neutrino Selection

In this analysis, we are searching for a neutrino signal in coincidence with gamma-ray bursts in the northern hemisphere. Specifically, we limit the search to the region  $\text{zenith} > 85^\circ$  ( $\text{declination} > -5^\circ$ ). In this band, muons produced by cosmic rays interacting in the upper atmosphere are stopped by the intervening matter, while neutrinos may reach the South Pole glacier and produce muons that pass through the detector. Thus, restricting ourselves to this part of the sky has the advantage that we can be confident that any well-reconstructed event pointing back to this region is in fact a neutrino event. The irreducible background for this analysis consists almost exclusively of well-reconstructed atmospheric neutrinos.

IceCube’s SMT-8 trigger produces events at a rate of over 2 kHz, but most of these events are well-reconstructed downgoing muons. They are easily rejected from this analysis by cutting on reconstructed zenith angle. A series of additional cuts are required to remove atmospheric muon events that are misreconstructed as upgoing. The most common causes of misreconstructed events are muons passing just outside the detector and emitting light inwards, and coincident muons from separate cosmic ray showers passing through the detector at the same time. In this chapter, we begin by describing the event parameters used to distinguish between well-reconstructed and misreconstructed events. Then we describe the simple initial cuts which reject the most obvious misreconstructed events. Finally, we will discuss an original, custom implementation of boosted and randomized decision tree forests — machine learning methods that allow us to achieve a high-purity final sample comprised almost exclusively of atmospheric (and possibly astrophysical) neutrinos at a rate of  $\sim 3.8$  mHz.



## 5.1 Event Quality Measures

In this section, we discuss event parameters which can be used to distinguish between well-reconstructed and misreconstructed events. Cut parameters fall into three broad categories: fit quality parameters, fit stability parameters, and event topology parameters. Throughout this section, plots of parameter distributions (Figures 5.1 through 5.14) will consist of IC79 data and simulation events remaining after applying the initial data-reduction cuts described in Section 5.2 (the last cuts before machine learning is applied). The distributions are most interesting at this level because the events which are easiest to reject are already cut away. Distributions from IC86 are nearly indistinguishable and are not shown. In each plot, backgrounds are normalized to Hz per bin and plotted against the left vertical axis. These include simulated atmospheric neutrinos (“NuGen Honda2006”, see Section 4.3.1), simulated cosmic ray induced muons (“CORSIKA”, see Section 4.3.2), the sum of these simulated atmospheric backgrounds (“Total MC”), and off-time data taken when no GRB was taking place (“Testing data”). A high-energy ( $E^{-2}$ ) neutrino signal is plotted against the right vertical axis in arbitrary units.

The overall data rate shows a  $\sim 50\%$  excess relative to simulated backgrounds because CORSIKA does not yet reproduce all of the ways in which real data can lead to misreconstructions and survive the initial quality cuts. This is typical for intermediate cut levels in IceCube analyses. Nevertheless, the shapes of the measured and simulated background distributions agree well. This gives us confidence that our simulations are sufficiently realistic to justify tuning the analysis to accept events similar to well-reconstructed simulated neutrinos while rejecting backgrounds characterized by the high-statistics (relative to the small on-time signal window) off-time dataset.

### 5.1.1 Fit Quality Parameters

Each event is reconstructed using LineFit as a first guess; iterations of the SPE maximum likelihood fit for refinement; and an MPE fit which yields a final reconstruction. In each case, the reconstruction yields not only a best-fit track direction, but also some information about how well the resulting direction hypothesis fits the observed light arrival pattern in the detector.

Charged leptons that generate enough light to be detected by IceCube are in general relativistic. The SPE and MPE fits assume a particle moving at the speed of light, but LineFit returns a best-fit velocity. Well-reconstructed events tend to have a LineFit velocity near the speed of light, while misreconstructed events tend to have a lower velocity. The LineFit velocity distribution for data, simulated backgrounds, and simulated signal at intermediate cut level is shown in Figure 5.1.

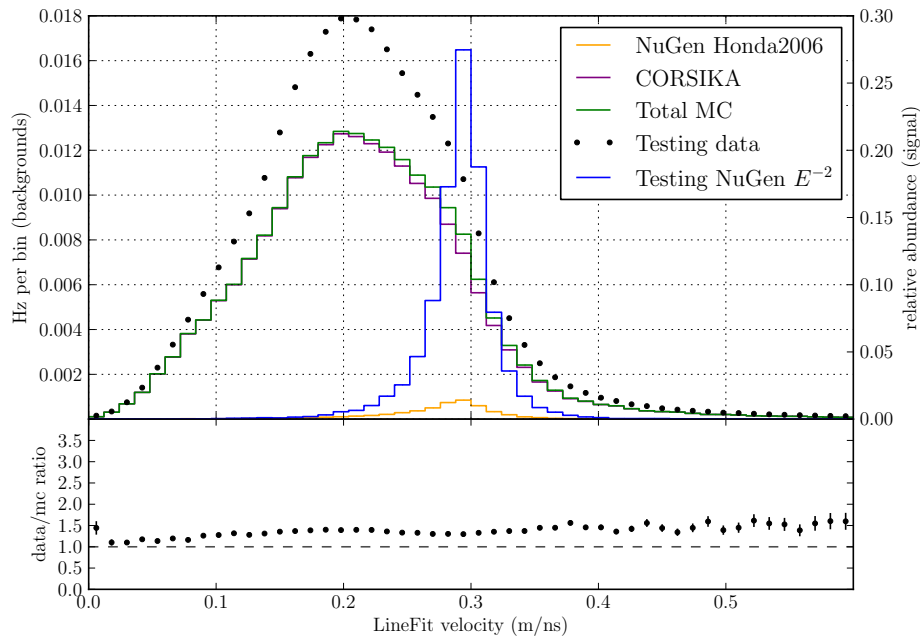


Figure 5.1: LineFit velocity distributions at intermediate cut level.

The maximum likelihood reconstructions return  $\text{logl}$ , the negative of the log-likelihood of the fit. These parameters are also measures of the fit quality. However, the parameter is normalized differently depending on the number of DOMs included in the fit. Therefore, we use a reduced log-likelihood parameter. The obvious choice of such a parameter is given by

$$\text{rlogl} = \frac{\text{logl}}{N_{\text{dof}}} = \frac{\text{logl}}{N_{\text{ch}} - 5},$$

where  $N_{\text{ch}}$  is the number of DOMs, or channels, included in the fit, and  $N_{\text{dof}} = N_{\text{ch}} - 5$  is the number of degrees of freedom in the fit. However, the performance of  $\text{rlogl}$  as a means to distinguish well-reconstructed events still varies with event energy. It was found that  $\text{plogl}$ , which is defined as

$$\text{plogl} = \frac{\text{logl}}{N_{\text{dof}} + 1.5} = \frac{\text{logl}}{N_{\text{ch}} - 3.5},$$

performs more consistently across the energy range to which IceCube is sensitive.  $\text{plogl}$  may be evaluated for any likelihood fit;  $\text{plogl}_{\text{SPE1}}$ , evaluated for the first iteration of SPE fit, appears to provide the best signal-to-background discrimination by a small margin. The distributions of this parameter are shown in Figure 5.2.

After the best fit directional reconstruction is established, either the paraboloid or Cramer-Rao fits are used to estimate the angular uncertainty. These fits probe the depth of the optimum in the reconstruction likelihood space. Thus, the estimated angular uncertainty is also a measure of fit quality. Well-reconstructed tracks tend to have smaller uncertainties. The distributions of the Cramer-Rao error are shown in Figure 5.3.

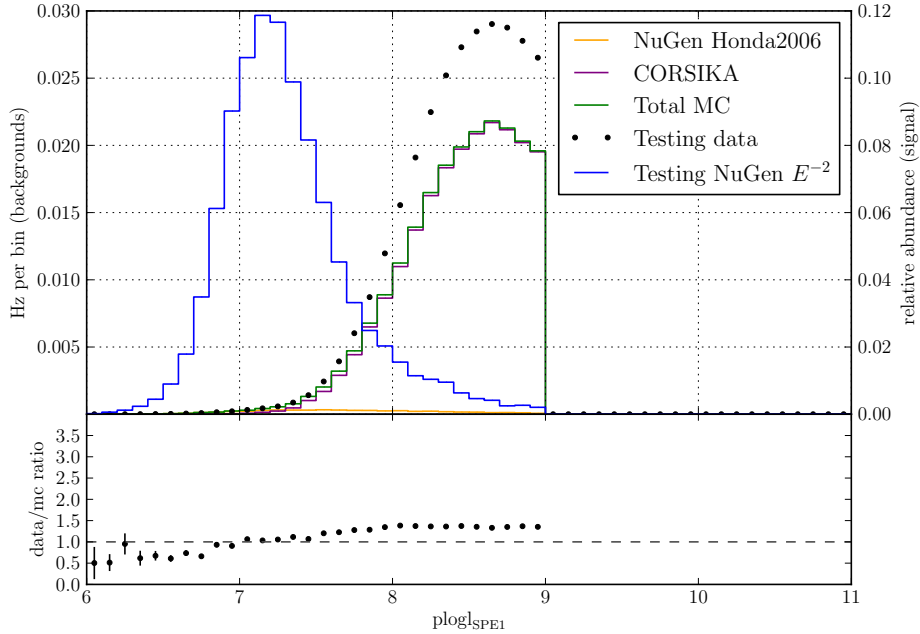


Figure 5.2:  $p\log_{10}l_{\text{SPE1}}$  distributions at intermediate cut level.

### 5.1.2 Fit Stability Parameters

Stability of the fit result under varied reconstruction hypotheses is another powerful way to discriminate between well-reconstructed and misreconstructed events. The simplest parameter of this type is the angular separation between the LineFit and MPE fit results. LineFit assumes an analytically simple ice model with no scattering, whereas MPE uses a more realistic treatment of absorption and scattering. These fits agree more closely for well-reconstructed tracks than for misreconstructed ones. The LineFit-MPE angular separation distributions are shown in Figure 5.4.

As indicated above, nearly all IceCube events are due to downgoing muons. The Bayesian up/down fit forces a downgoing reconstruction by using a Bayesian prior which harshly penalizes upgoing fits. For well-reconstructed events, this tends to yield a much worse log likelihood. For misreconstructed events, the log

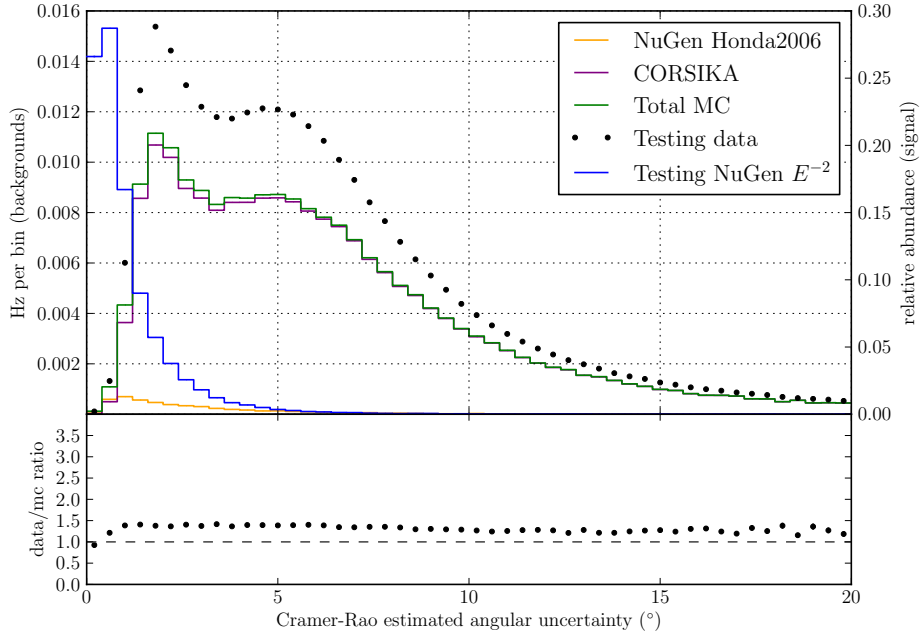


Figure 5.3: Cramer-Rao angular uncertainty distributions at intermediate cut level.

likelihood is only slightly worse. Thus the *Bayes ratio* is an independent measure of fit stability. Specifically, we use  $\log\text{-Bayes-ratio} = \log l_{\text{Bayes}} - \log l_{\text{SPE}}$ . The distribution of this parameter is shown in Figure 5.5.

One more test of fit stability is done using the split pulse series reconstructions. For a stable track fit, each pair of two pulse subseries yields a pair of reconstructions that agree well with each other. For misreconstructed events, especially coincident events, the pulse subseries fits are not well correlated. Figures 5.6 and 5.7 show the angular separation distributions for the time- and geometry-split pulse series. A related parameter is the minimum zenith of all four split reconstructions. For truly upgoing events, split-min-zenith agrees well with the zenith distribution of the events; for misreconstructed and coincident downgoing events, split-min-zenith tends to fall in the downgoing region. The split-min-zenith distribution is shown in Figure 5.8. Finally, the log-Bayes-ratio can be found for

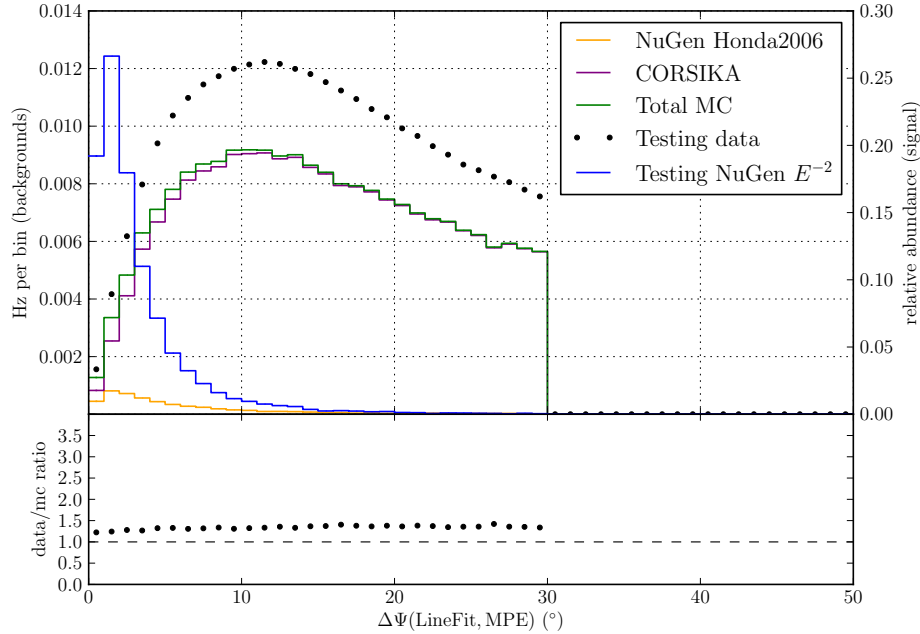


Figure 5.4:  $\Delta\Psi(\text{LineFit}, \text{MPE})$  distributions at intermediate cut level.

each pulse subseries fit. The split-min-log-Bayes-ratio behaves similarly to the ordinary log-Bayes-ratio; distributions are shown in Figure 5.9.

### 5.1.3 Event Topology Parameters

Parameters describing the distribution of light about the reconstructed track, or the event topology, serve as another discriminator between well-reconstructed and misreconstructed events. Some of these invoke the concept of a *direct hit*. A direct hit is defined as a DOM in which the first pulse arrives at approximately the expected time given the reconstructed track. In the standard processing used in this analysis, the allowed arrival time for a direct hit is  $-15 \text{ ns} < t_{\text{res}} < 75 \text{ ns}$ . The first topology parameter is  $N_{\text{dir}}$ , the number of direct hits. A larger number of direct hits suggests a better reconstruction. The  $N_{\text{dir}}$  distributions are shown in Figure 5.10.

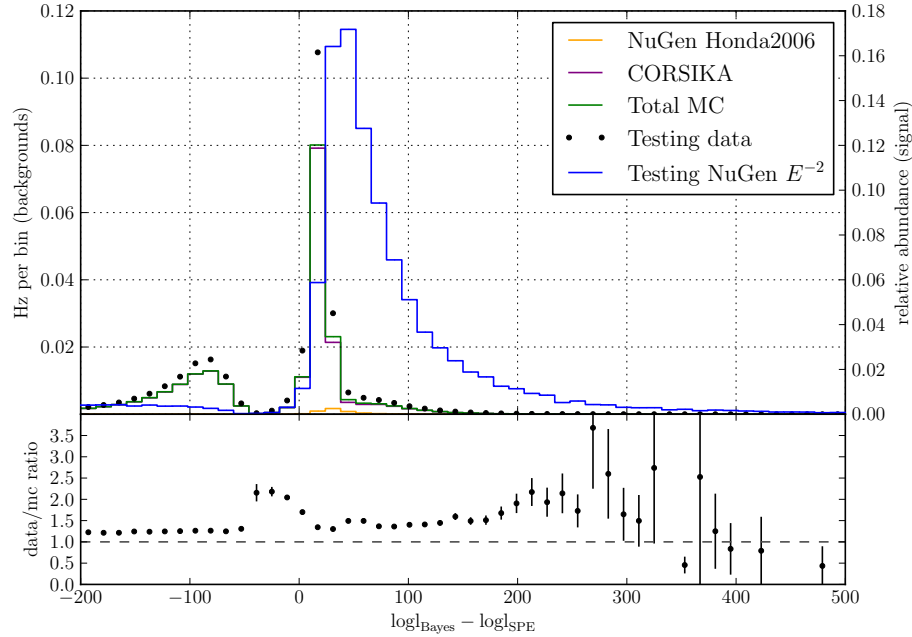


Figure 5.5: Log-Bayes-ratio distributions at intermediate cut level.

Each DOM used in a track reconstruction can be assigned a position along the track by projecting each DOM radially inward onto the track. The largest distance between these positions for any two direct hits is referred to as  $L_{\text{dir}}$ , which is a measure of the “lever-arm” of the fit. The  $L_{\text{dir}}$  distributions are shown in Figure 5.11.  $N_{\text{dir}}$  and  $L_{\text{dir}}$  are also combined to form the direct ellipse parameter, which is defined as  $(L_{\text{dir}}/60 \text{ m})^2 + (N_{\text{dir}}/15)^2$ . The direct ellipse distributions are shown in Figure 5.12.

Two more parameters are defined using the track positions of all DOMs used in the reconstruction and located within 150 m of the track.  $L_{\text{empty}}$  is the maximum distance along the track in which no such DOMs are found. Well-reconstructed muon tracks typically have relatively smooth light patterns and thus small values for  $L_{\text{empty}}$ ; distributions are shown in Figure 5.13. The separation is the distance along the track between the first and last quartile of DOMs ordered by the time of the first pulse arrival. Separation, like  $L_{\text{dir}}$ , is a measure of the “lever-arm”,

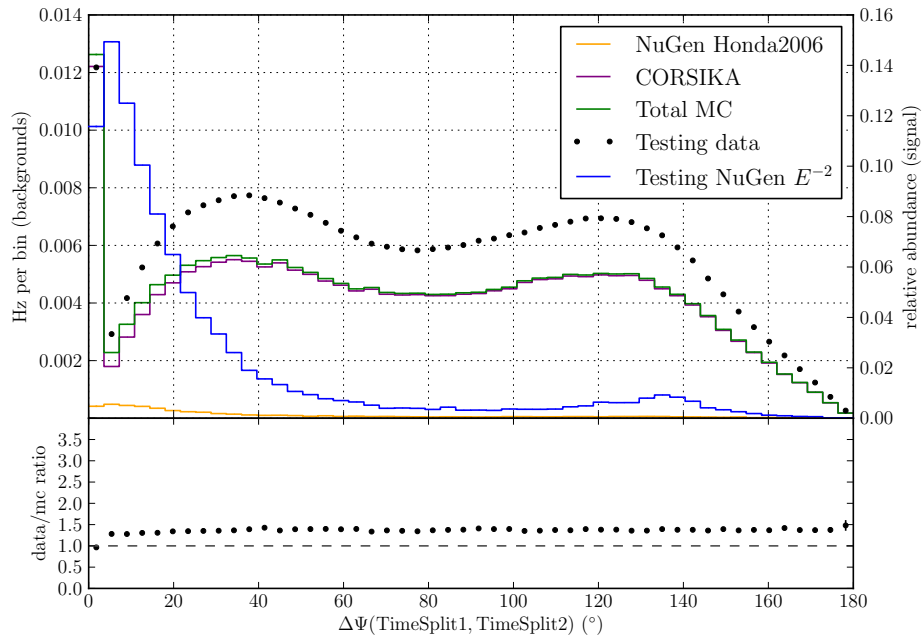


Figure 5.6:  $\Delta\Psi(\text{Time Split 1, Time Split 2})$  distributions at intermediate cut level.

so larger values correspond to better reconstructions; distributions are shown in Figure 5.14.



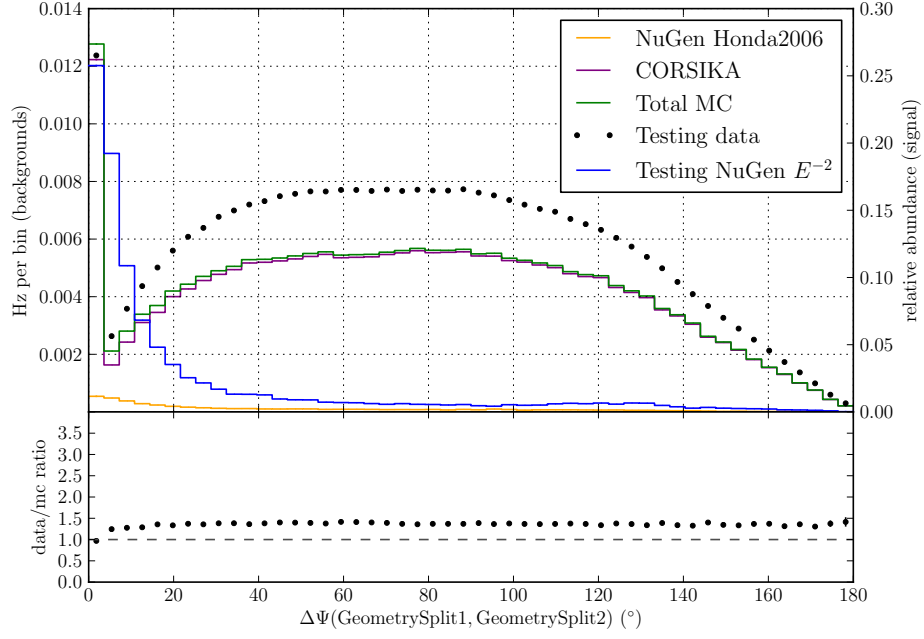


Figure 5.7:  $\Delta\Psi(\text{Geometry Split 1, Geometry Split 2})$  distributions at intermediate cut level.

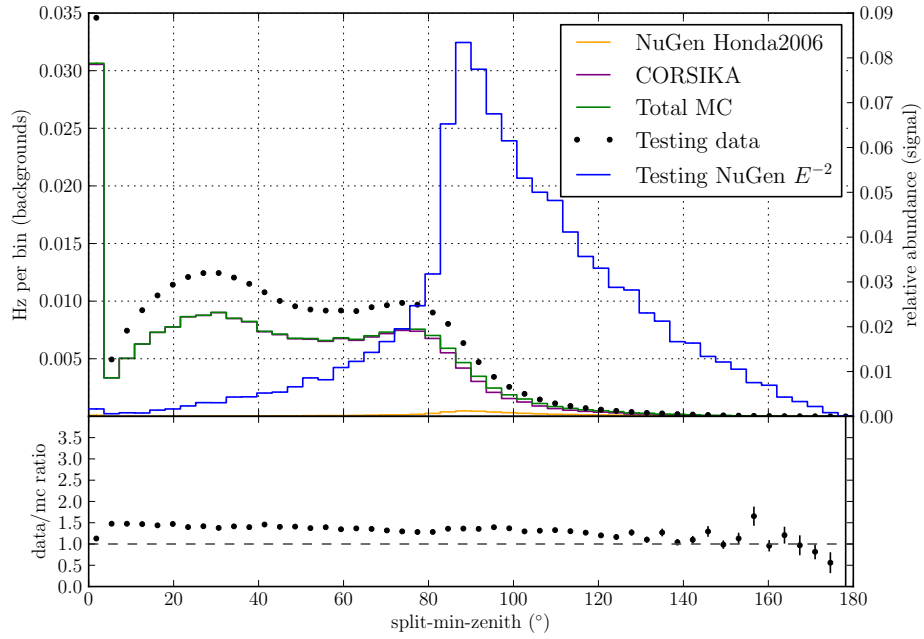


Figure 5.8: Split-min-zenith distributions at intermediate cut level.

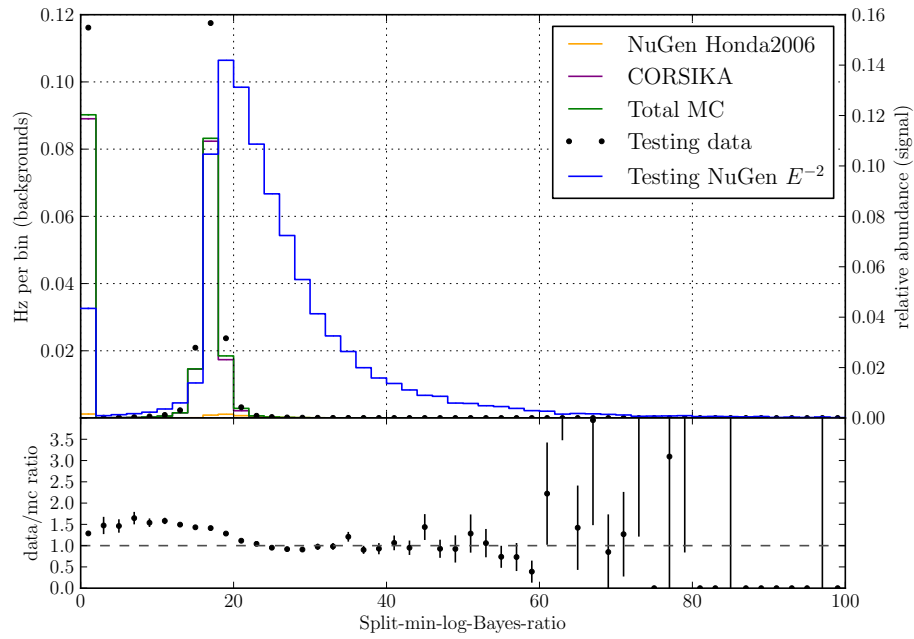


Figure 5.9: Split-min-log-Bayes-ratio distributions at intermediate cut level.

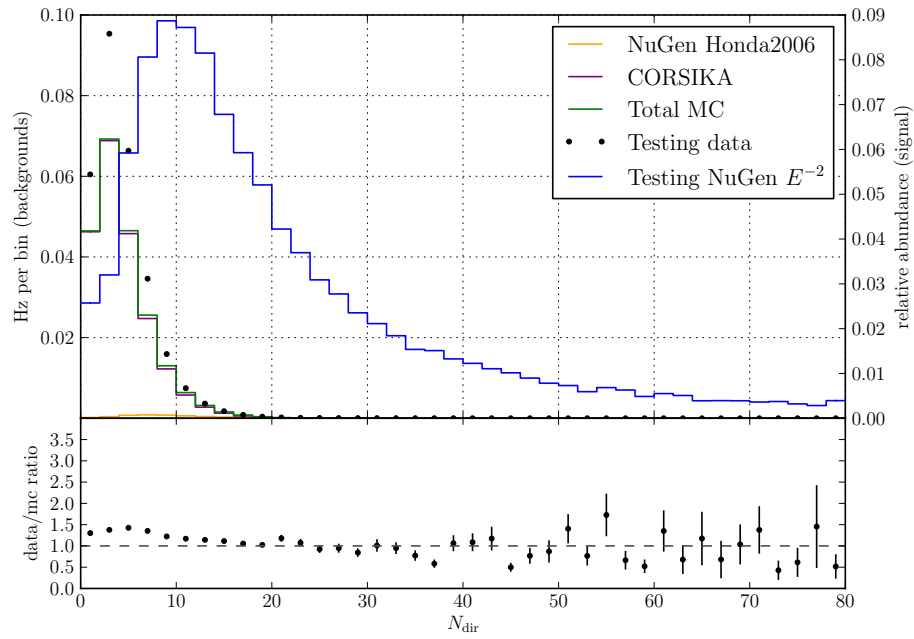


Figure 5.10:  $N_{\text{dir}}$  distributions at intermediate cut level.

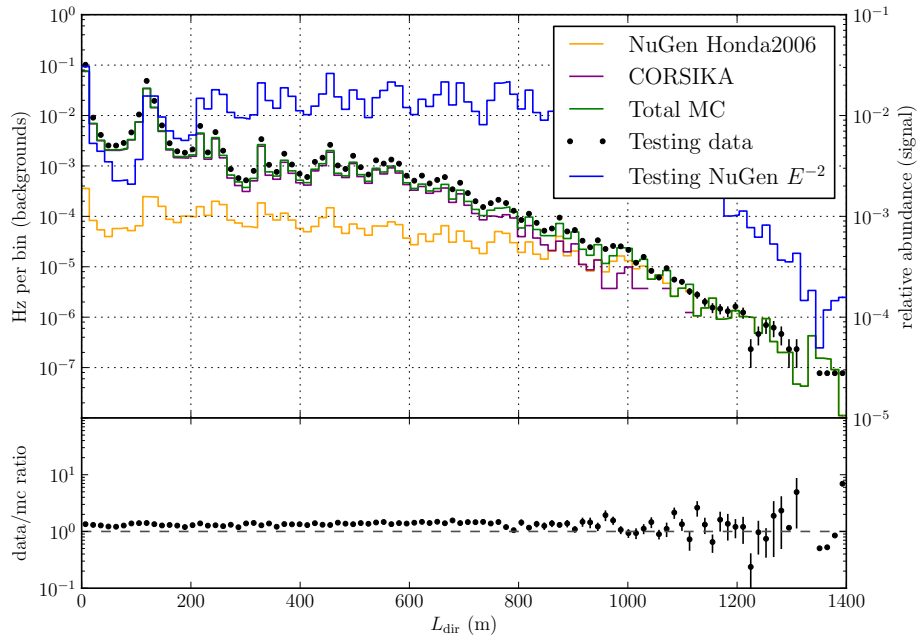


Figure 5.11:  $L_{\text{dir}}$  distributions at intermediate cut level.

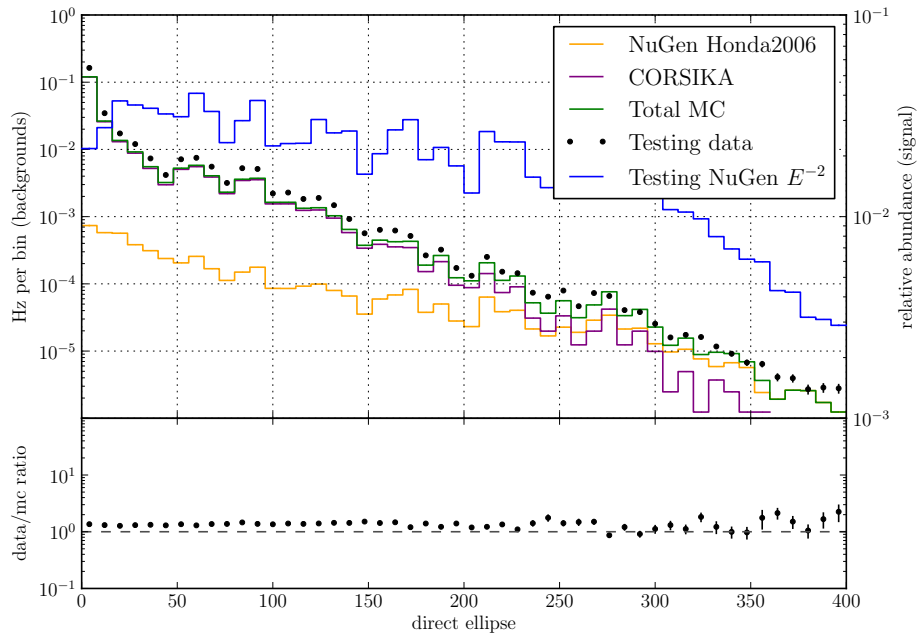


Figure 5.12: Direct ellipse distributions at intermediate cut level.

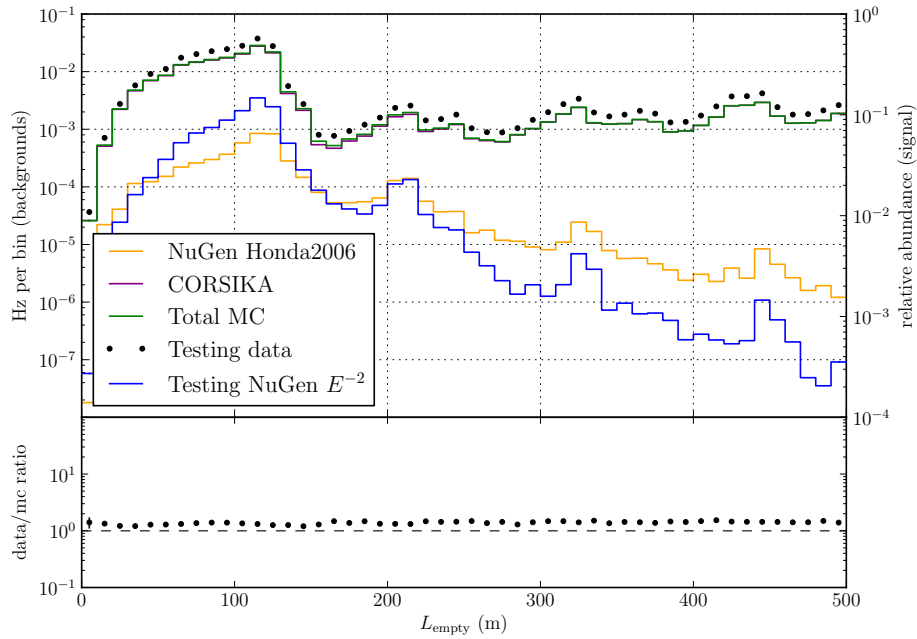


Figure 5.13:  $L_{\text{empty}}$  distributions at intermediate cut level.

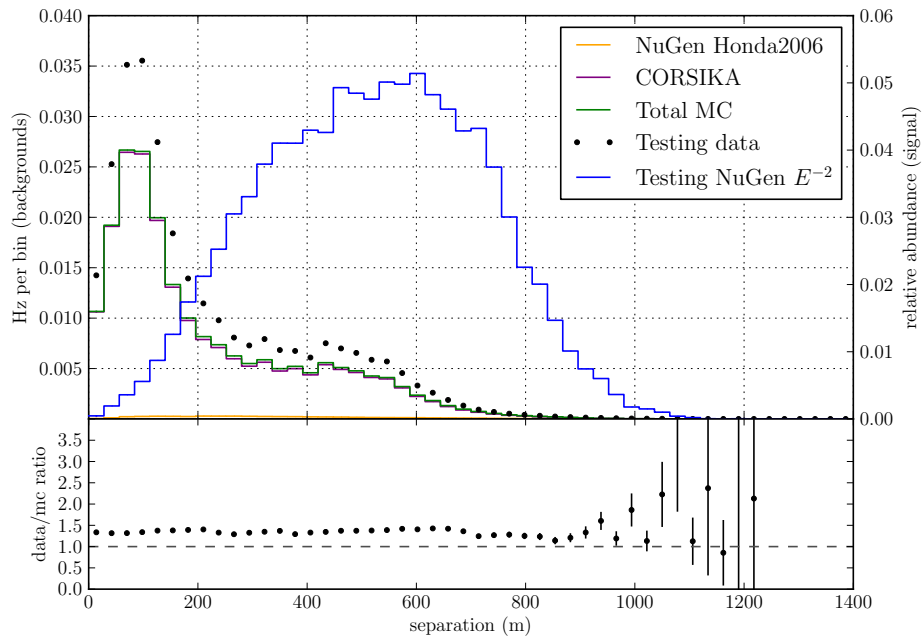


Figure 5.14: Separation distributions at intermediate cut level.

## 5.2 Initial Data-Reduction Cuts

In this section, we discuss the initial cuts that reduce the data sample from the  $> 2$  kHz SMT-8 trigger rate to below 1 Hz. This is done in three steps. At the South Pole, the PnF system described in Section 3.3.2 applies the Muon Filter to reduce the data rate to 30 Hz. Then an analysis-level filter is applied. For IC79, the Muon Level 3 filter is applied in the North to reduce the data rate to 0.9 Hz. For IC86-1, we use the Online Level 2 filter, which reduces the data rate to 3.5 Hz at the South Pole. Before transferring the data to the University of Maryland, an additional quality cut is applied to reduce the data rate to just under 0.3 Hz. These cuts yield datasets that are computationally practical to use with machine learning methods while retaining 95% of simulated signal neutrinos that pass the Muon Filter.

### 5.2.1 Muon Filter

The Muon Filter reduces the data rate to about 30 Hz, yielding a small enough data volume for transfer to the north via satellite. First, the following base cut is applied prior to any maximum likelihood reconstructions:

$$N_{\text{ch}} \geq 8 \text{ and } (N_{\text{ch}} \geq 10 \text{ or LineFit zenith} > 70)$$

Then the SPE1 maximum likelihood reconstruction is performed. For events with  $\theta_{\text{SPE1}} > 78.5^\circ$ , a plogl-like cut is applied. For events with  $\theta_{\text{SPE1}} < 78.5^\circ$ , a zenith-dependent  $Q_{\text{tot}}$  cut is applied. For IC79 and IC86-1, the cuts were slightly different; they are summarized below.

- IC79

$$[\theta_{\text{SPE1}} \leq 60^\circ \text{ and } \log(Q_{\text{tot}}) \geq 0.6 \cos(\theta_{\text{SPE1}}) + 2.5]$$

$$\text{or } [60^\circ < \theta_{\text{SPE1}} \leq 78.5^\circ \text{ and } \log(Q_{\text{tot}}) \geq 3.9 \cos(\theta_{\text{SPE1}}) + 2.5]$$

$$\text{or } [78.5^\circ < \theta_{\text{SPE1}} \text{ and } \log l_{\text{SPE1}} / (N_{\text{ch}} - 2) \leq 8.1]$$

- IC86-1

$$[\theta_{\text{SPE1}} \leq 60^\circ \text{ and } \log(Q_{\text{tot}}) \geq 0.6 \cos(\theta_{\text{SPE1}}) + 2.6]$$

$$\text{or } [60^\circ < \theta_{\text{SPE1}} \leq 78.5^\circ \text{ and } \log(Q_{\text{tot}}) \geq 3.9 \cos(\theta_{\text{SPE1}}) + 2.6]$$

$$\text{or } [78.5^\circ < \theta_{\text{SPE1}} \text{ and } \log l_{\text{SPE1}} / (N_{\text{ch}} - 3) \leq 8.7]$$

The stream of events passing these cuts are transferred via satellite to the data warehouse at the University of Wisconsin (UW) Madison, where they can be accessed for further processing and analysis.

## 5.2.2 Analysis Level Filter

At the time of the development of the IC79 analysis, muon-channel offline processing at UW-Madison had already reached an advanced stage. The Muon Level 3 processing builds upon the offline Level 2. At this point, the final MPE reconstruction is complete, so we can restrict our focus to upgoing events which are useful in this analysis. The following cut is applied before running the final reconstructions:

$$\text{Direct Ellipse} > 2 \text{ and } \text{plog} l_{\text{MPE}} \leq 12 \text{ and } \text{Separation} > 0 \text{ and } L_{\text{empty}} \leq 500$$

$$\text{and } \Delta\Psi(\text{SPE4}, \text{MPE}) \leq 50^\circ.$$

This cut reduces the data rate to 0.9 Hz, with a 98% efficiency with respect to the muon filter for an  $E^{-2}$  spectrum for events reconstructed within  $3^\circ$  of the true direction based on simulation.

At the time of the development of the IC86-1 analysis, the offline processing was not yet ready for use. However, we were able to make use of the Online Level 2 stream produced by PnF at the South Pole for use in the gamma and optical rapid follow-up programs. The following cut is applied before running the final reconstructions:

$$\theta_{\text{SPE1}} < 75^\circ \text{ and } \{\log_{10} Q_{\text{tot}} > 3.3 - 1.3(\theta_{\text{SPE1}}/1.309)^6\}$$

or

$$75^\circ \leq \theta_{\text{SPE1}} < 80^\circ \text{ and } \{\log_{10} Q_{\text{tot}} > 1.95 \text{ or } \text{rlog}_{\text{SPE1}} < 7.3\}$$

or

$$80^\circ \leq \theta_{\text{SPE1}} \text{ and } \{\text{llog}_{\text{SPE1}}/(N_{\text{ch}} - 2) \leq 7.3 \text{ or } N_{\text{ch}} > 70 \\ \text{or } [(L_{\text{dir}})_{\text{SPE1}}/180]^2 + [(N_{\text{dir}})_{\text{SPE1}}/10]^2 \geq 1\}.$$

This cut reduces the data rate of upgoing-reconstructed events to 3.5 Hz, with a 98% efficiency with respect to the muon filter for an  $E^{-2}$  spectrum for events reconstructed within  $3^\circ$  of the true direction based on simulation.

### 5.2.3 Basic Quality Cut

After the analysis level cuts, there is still room for very simple cuts to substantially reduce the background rate while preserving the majority of well-

reconstructed simulated signal events. The purpose of these cuts is to allow the decision tree forests described below in Section 5.3 to work only on the most difficult backgrounds.

For IC79, the following cut was applied to events which passed the Muon Level 3:

$$\text{plogl}_{\text{SPE1}} < 9 \text{ and } \Delta\Psi(\text{LineFit, MPE}) < 30^\circ \text{ and Cramer-Rao error} < 180^\circ.$$

For IC86-1, the following cut was applied to events which passed the Online Level 2:

$$\text{plogl}_{\text{MPE}} < 8.25 \text{ and } \Delta\Psi(\text{LineFit, MPE}) < 30^\circ.$$

### 5.3 Neutrino Level Cut

After the cuts described in the previous section, the data rate is under 1 Hz, but most remaining events are still misreconstructed cosmic ray muon events. We seek to retain well-reconstructed upgoing events only, while rejecting all others as backgrounds. This is a binomial classification problem. Recently, decision tree forests [93] have emerged as a popular classification strategy. A custom, hybrid Python-C++ decision tree forest implementation called `pybdt` was developed for this analysis and is now used in several IceCube analyses. In this section, we describe decision tree forests in detail. While decision tree forests may be used for multinomial or continuous classification (i.e. regression), we will restrict our attention to binomial classification.



### 5.3.1 Decision Trees

A decision tree consists of a binary tree with a cut on one parameter specified at each node except the *leaf nodes*, which have no child nodes. A leaf node may be either a *signal leaf* or a *background leaf*. The rest of the nodes may be referred to as *split nodes*. An event of unknown class is classified by tracing its path through the tree until a leaf node is reached. An example decision tree is shown in Figure 5.15.

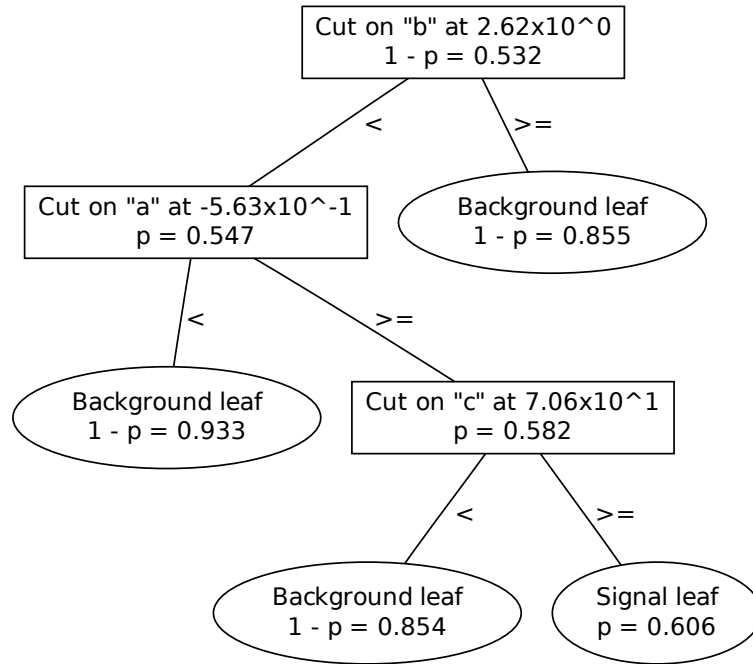


Figure 5.15: An example decision tree.

Decision trees are generated by a process called *training*, discussed in detail below; event ensembles of known class are split into *training* and *testing* samples, where the former is used to construct trees and the latter is used to validate them. The tree in Figure 5.15 was constructed for a toy dataset in which events are characterized by three parameters *a*, *b* and *c*. In the figure, split nodes are

indicated by rectangles and leaf nodes are indicated by ellipses. For split nodes, the cut parameter name and value are shown. The value  $p$  is the *signal purity*: the ratio of signal weight ( $w_S$ ) to total signal + background weight ( $w_S + w_B = W$ ) for training sample events passing through a given node. The class of each leaf node is determined by its signal purity. If  $p \geq 1/2$ , it is a signal leaf; otherwise, it is a background leaf.

### 5.3.1.1 Decision Tree Training

Decision tree training is a recursive process. At a given node, starting with the root node, an ensemble of signal training events and background training events remains. The separation at a node is given by the gini separation criterion:  $S_G(p) = p \cdot (1 - p)$ . For any proposed split, some signal and some background events will descend to the left and to the right. If the purity and total weight in the left and right nodes are  $p_L$ ,  $W_L$ ,  $p_R$  and  $W_R$  respectively, then the separation gain is given by

$$\Delta S = W \cdot S_G(p) - W_L \cdot S_G(p_L) - W_R \cdot S_G(p_R).$$

Each event parameter is histogrammed, and the algorithm considers placing a cut at each bin boundary in each histogram. The cut which yields the largest separation gain  $\Delta S$  is selected.

The use of the gini separation gain is illustrated for toy cut parameter distributions in Figure 5.16. The red curve shows the separation gain for a possible cut at each histogram bin boundary. The optimal cut is given by the peak of the red curve, which sits between the signal and background distributions. Training at a given node can be visualized as finding the overall maximum of the separation gain curves for all event parameters.

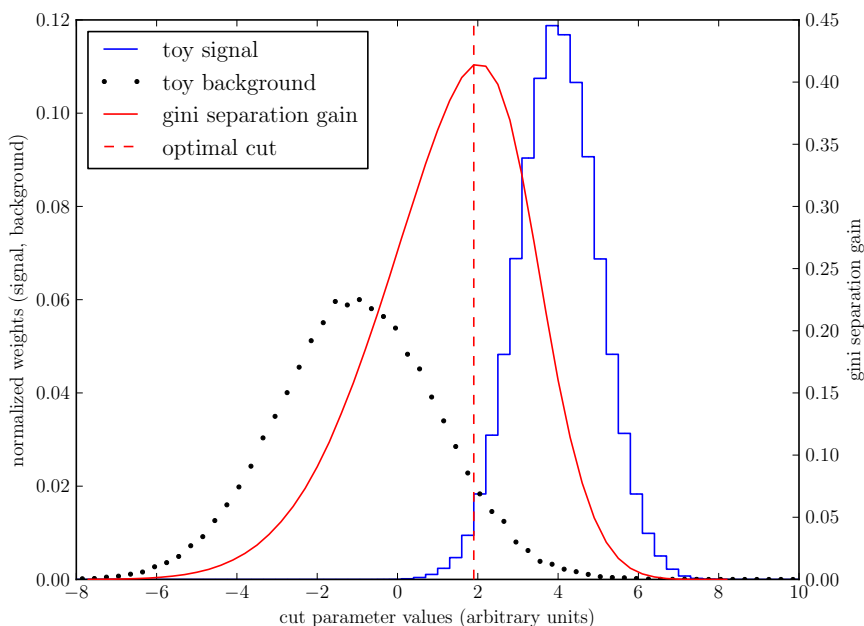


Figure 5.16: Cut selection using the gini separation gain.

Once an optimal cut is selected, the algorithm repeats recursively on the left (less than the chosen cut value) and right (greater than the chosen cut value) subsamples. Training continues until one of the following stopping criteria is reached:

- The user-specified maximum tree depth is reached.
- A node has either only signal or only background training events remaining.
- The best available split would result in a node with less than a user-specified minimum number of events remaining.

### 5.3.2 Boosted and Randomized Decision Tree Forests

The performance of a single decision tree is limited by its depth and the degree to which its training samples represent the true underlying distributions.

Without making many levels of cuts, less-typical events will be misclassified by any given tree. However, very deep trees have the drawback that they are finely-tuned to the details of the less-typical events in the training sample such that their performance on testing or unknown samples is not consistent with their performance on the training sample. This is referred to as *overtraining*.

In order to achieve better signal-background separation without incurring overtraining, decision tree forests are used. A forest consists of many decision trees — hundreds are used in this analysis — each with a weight  $\alpha$ . A forest yields a score on the interval  $[-1, +1]$  rather than a discrete signal or background classification. It is up to the analyzer to select a cut on this score which gives the appropriate signal efficiency and background rejection for their analysis. Each tree in the forest yields a score of either  $+1$  for signal or  $-1$  for background for any event. The forest score for an event  $i$  is a weighted average of its scores from each tree  $m$ :

$$-s_i = \frac{\sum_m \alpha_m \cdot (s_i)_m}{\sum_m \alpha_m}.$$

The trees in the forest differ because they are trained under slightly different conditions. Two techniques are commonly used for this purpose: boosting and randomization. One or both of these may be used to generate a forest.

### 5.3.2.1 Boosted Decision Tree Forests

Boosted decision tree forests<sup>1</sup> are generated by adjusting the relative weights  $w_i$  of training sample events in between each individual tree training. This process is called boosting because it “boosts” the weights of misclassified training events.

---

<sup>1</sup>Boosted decision tree forests are sometimes referred to as Boosted Decision Trees or BDTs, but here we use the term “forest” explicitly to emphasize that boosting affects the forest, not the operation of individual decision trees.

In `pybdt`, the AdaBoost algorithm [94] is used. After a tree is trained, we compare the training sample scores  $s_i$  (either +1 or -1 for each event) with the known event identities  $y_i$ . We define a function to indicate whether an event is classified incorrectly:  $I(s, y) = 0$  if  $s = y$  and 1 otherwise. Then we calculate the error rate for the tree:

$$e = \frac{\sum_i w_i \cdot I(s_i, y_i)}{\sum_i w_i}$$

and the boost factor for the tree:

$$\alpha = \beta \cdot \ln \left( \frac{1 - e}{e} \right).$$

Here,  $\beta$  is a user-specified boost strength (typically between 0 and 1). The weights are adjusted using this boost factor:

$$w_i \rightarrow w_i \cdot e^{\alpha \cdot I(s_i, y_i)}.$$

Then the weights are renormalized so that  $\sum_i w_i = 1$ . The new weights are used to train the next tree. After that, the weights are boosted yet again. Boosting is cumulative; the weights are never reset to their original values. When boosting is used, the per-tree weights used for scoring are the boost factors  $\alpha$ .

It is interesting to note that when boosting is used, the most important trees for rejecting the bulk of the background are the first few that are trained. The tree weights as a function of tree number are shown in Figure 5.17. As the individual event weights are more and more distorted, the trees become specialized on difficult classes of events. Thus the bulk of events are handled well by a small number of higher weighted trees, and the more difficult ones are handled by a large number of lower weighted trees.

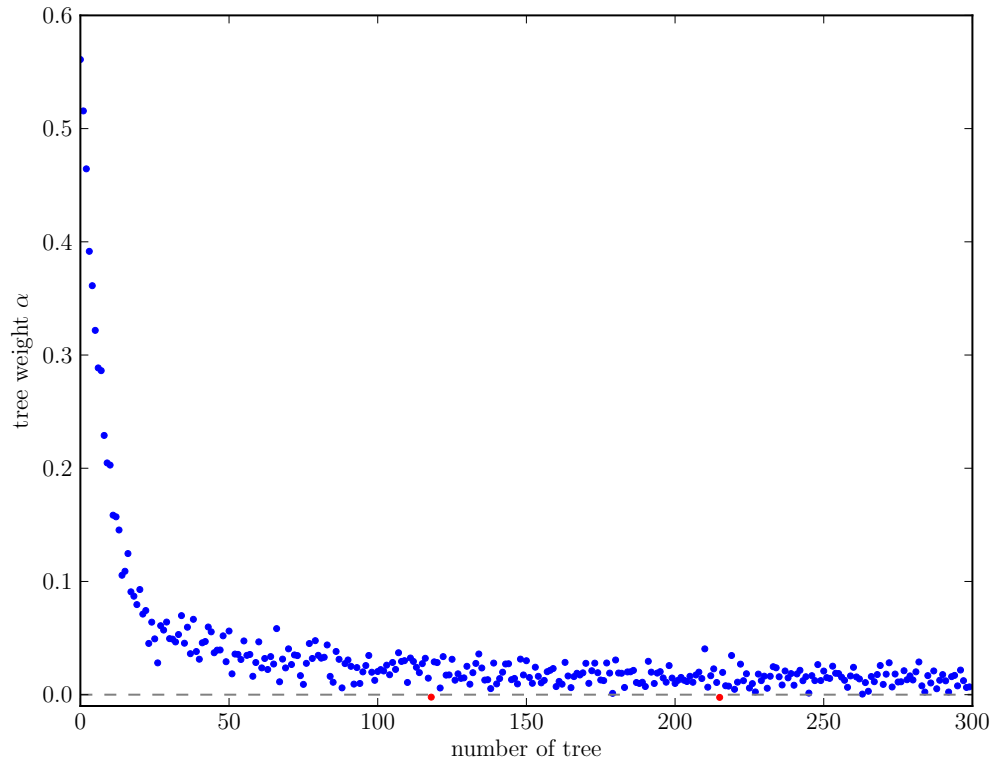


Figure 5.17: Decision tree weights as a function of tree number. The red dots indicate trees with negative weight. This is only possible when randomization (discussed in Section 5.3.2.2) is used.

### 5.3.2.2 Random Decision Tree Forests

Random decision tree forests, also known simply as random forests, are generated by using randomization rather than boosting to differentiate trees. Often, either boosting with no randomization or randomization with no boosting is used. However, there is no technical reason that these techniques cannot be combined, and the implementation in `pybdt` allows the user to use both if desired. Two types of randomization are available in `pybdt`:

Cut parameter randomization. The user provides an integer `num_cut_variables`, which must be less than the total number of event parameters being used. Then during training, *at each node*, only this many parameters are randomly selected to be considered for choosing a split.

Training event randomization. The user provides a fraction `frac_random_events` between 0.0 and 1.0. Then during training, *for each tree*, only this fraction of the full training sample is randomly chosen to be used for training.

Random forests are naturally less prone to overtraining than boosted decision tree forests because every tree is trained under different conditions. Randomization may also be used as a way to reduce overtraining in boosted decision tree forests.

When randomization is used and boosting is not, each tree in the forest receives equal weight in determining the score of an event.

### 5.3.2.3 Pruning

Overtraining can arise asymmetrically within a given decision tree. After some split, one branch of the tree may contain additional useful splits, while the other disproportionately contains less productive splits that are over-tuned to the training samples. Therefore, it can be useful to prefer a larger maximum depth and to remove parts of trees that add little discrimination power compared to the tree complexity they add. This is referred to as *pruning* [95]. When a decision tree is pruned at some node, its child nodes are destroyed. The node becomes a leaf whose class is determined by the signal purity as described in Section 5.3.1.1.

In `pybdt`, a very simple *same leaf* pruning algorithm is automatically applied by default. This algorithm searches for split nodes for which each child node is a leaf. If both leaves are of the same class, the tree is pruned at that split. This is repeated until no such splits remain.

Next, *cost complexity pruning* may be applied. This algorithm identifies subtrees that add more leaves but not much separation. It defines a pruning sequence in which the first step prunes the most expendable subtree, and the last step would leave only the root node. The user provides a pruning strength: the percentage of the pruning sequence to execute.

At each step, the next node to prune is determined as follows. For each split node, the weighted separation gain  $g = W \cdot S_G$  is calculated. Then the pruning cost  $\rho = (g - g_L - g_R)/(n_{\text{leaves}} - 1)$  is found. Here  $L$  and  $R$  refer to the left and right child nodes, and  $n_{\text{leaves}}$  is the total number of leaves in the subtree below this split. The split node with the smallest  $\rho$  is pruned next. Since this changes the number of leaves, the pruning costs are recalculated at each step before picking the next node to prune. The entire pruning sequence is calculated on a copy of the tree before executing the pruning sequence on the actual tree.

### 5.3.3 Final Sample

For both IC79 and IC86-1, the final sample is found by applying a cut on the decision tree forest score. Score distributions for IC79 and IC86-1 are shown in Figure 5.18. For each configuration, many classifiers are tested using simulated datasets along with off-time data — events which occurred at least two hours from any Northern hemisphere GRB. Once a classifier is chosen, the value of the score cut is determined using the discovery potential, which is described in Section 6.3.4. Below, the classifier selection and the performance of the final samples are discussed.

#### 5.3.3.1 IC86-1 Classifier

We begin with IC86-1, which was analyzed earlier. For that detector configuration, the behavior of the boosted decision tree training parameter space was probed using a grid search of three parameters. Each forest had 400 trees, and each split was chosen by considering 20 evenly spaced cut values of each variable. Maximum depths of 2–4, boost strengths  $\beta$  of 0.1 to 0.5, and pruning strengths of 0–20% were tested.

Our goal is to make a quantitative comparison of the performance of slightly



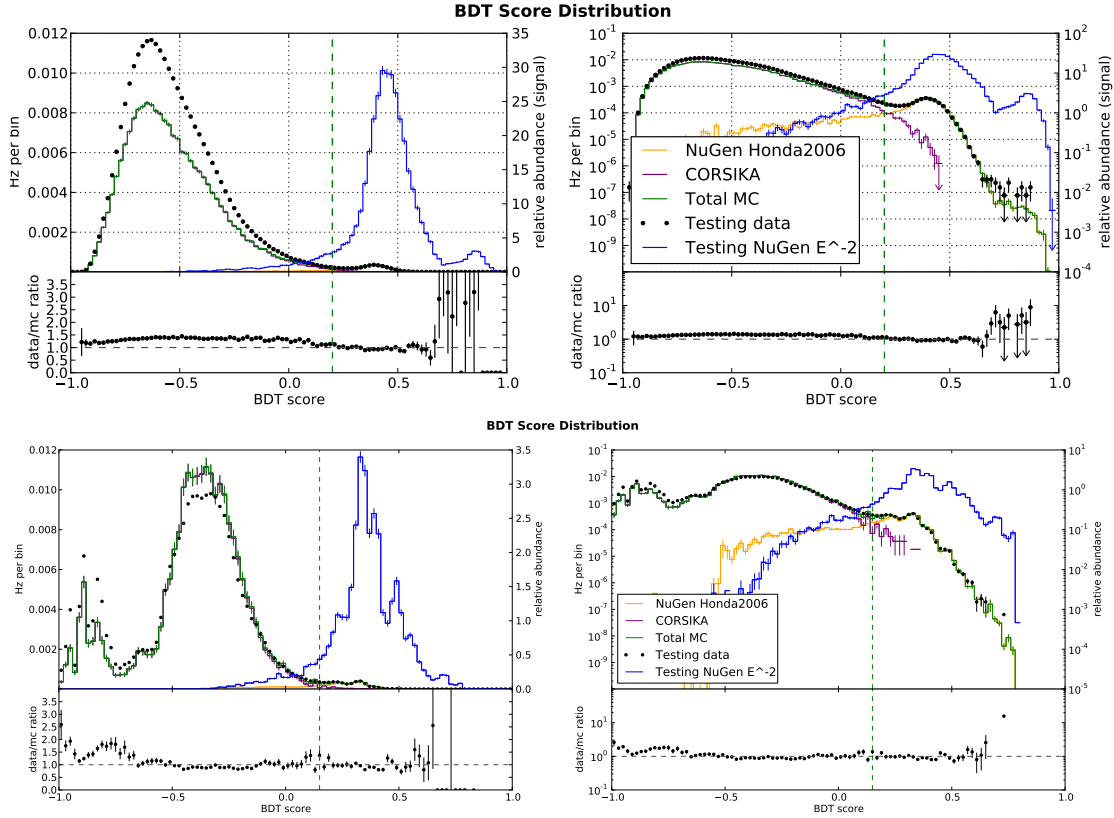


Figure 5.18: Score distributions for IC79 (top) and IC86-1 (bottom). The left and right plots use linear and log vertical scales, respectively. Background is studied using off-time data as well as simulated atmospheric neutrinos (“NuGen Honda2006”) and muons (“CORSIKA”). The sum of the atmospheric backgrounds is shown in green and compared to off-time data in the plots adjoined below. All backgrounds are normalized to Hz per bin on the left vertical axis; a possible  $E^{-2}$  signal neutrino population is normalized in arbitrary units on the right vertical axis. Data and simulated backgrounds agree well near the final cut values (indicated by dashed vertical lines); agreement is less correct for lower scores and more difficult to measure due to a small number of surviving events for very high scores.

different classifiers. Normally, we would use the full unbinned likelihood analysis described in Section 6.3.4 to calculate discovery potentials, but for comparing a large number of classifiers this method is too computationally expensive. Instead, we follow the prescription in [96] to calculate a proxy for the discovery potential as a function of score cut for each classifier by treating the search as a simple counting experiment. We suppose that the signal window is 1% of the Northern hemisphere

with total on-time window of 7000 s. The expected number of background events  $\mu_b$  falling in this window is therefore the data rate  $\times 0.01 \times 7000$  s. The signal is approximated as an  $E^{-2}$  spectrum with an arbitrary but fixed normalization; the expected number of signal events  $\mu_s$  is taken to be simply one second times the signal rate based on simulation.

Poisson statistics are used to find the least detectable signal  $\mu_{\text{LDS}}$ , which is the expected number of signal events giving a total expected number of events  $\mu_{\text{LDS}} + \mu_b$  that, in 90% of experiments, would yield a  $5\sigma$  upward fluctuation in the number of observed events relative to the background-only expectation of  $\mu_b$  events. The background-only and signal+plus+background distributions are

$$P_{\text{Poisson}}(N; \mu_b) = \frac{\mu_b^N}{N!} \cdot \exp(-\mu_b), \quad (5.1)$$

and

$$P_{\text{Poisson}}(N; \mu_s + \mu_b) = \frac{(\mu_s + \mu_b)^N}{N!} \cdot \exp(-(\mu_s + \mu_b)) \quad (5.2)$$

respectively. The observed number  $n_{5\sigma}$  of events constituting a significant upward fluctuation is found by numerically solving

$$P_{\text{Poisson}}(\geq n_{5\sigma} | \mu_b) < 5.73 \times 10^{-7}, \quad (5.3)$$

and the least detectable signal is found by numerically solving

$$P_{\text{Poisson}}(\geq n_{5\sigma} | \mu_{\text{LDS}} + \mu_b) = 10\%. \quad (5.4)$$

Finally, the discovery potential, which is also a function of score cut, is given by  $D = \mu_{\text{LDS}}/\mu_s$ . The result for the chosen classifier is shown in Figure 5.19. This

function quantifies the feasibility of obtaining a significant result, and therefore it decreases with decreasing  $\mu_b$  and increases with decreasing  $\mu_s$ . Because the classifiers are trained to assign signal events higher scores, there is an optimal score cut value which minimizes  $D$ . However, the precise coordinates of the optimum are subject to fluctuations because the Poisson probability distribution function used to calculate  $\mu_{LDS}$  is only defined for integer event counts, yielding a ragged curve for  $D$ . Nevertheless, stronger classifiers tend to produce smaller minimum values of  $D$ .

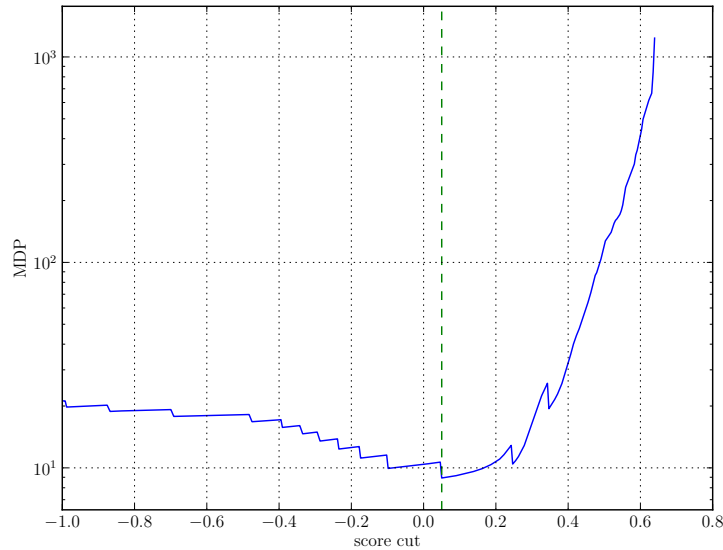


Figure 5.19: Discovery potential proxy as a function of final score cut value for the classifier used for IC86-1. The curve is ragged due to the use of the Poisson probability distribution, which is only defined for integer event counts, in the calculation of the least detectable signal.

The dependence of the discovery potential proxy on training parameters is shown in Figure 5.20. Fluctuations in the discovery potential obscure the results somewhat, but the general trend is that the power of the classifier increases with tree depth and is relatively independent of the boost strength and pruning strength. We expect deeper trees to improve classification by providing more op-

portunities to explore the event feature space, so this trend is intuitive. However, deeper trees also introduce overtraining. For forests trained with a maximum tree depth of 4, a significant data/MC disagreement emerged for moderately high scores. The classifier went beyond discriminating between well-reconstructed and misreconstructed events, and it started to expose small but non-negligible differences between simulated and real events. Overtraining persisted even for large pruning strengths, so ultimately the maximum tree depth was set to 3. The pruning strength was also increased to 30% to further reduce overtraining. The boost strength was set to 0.5.

The performance of the selected classifier can be quantified in a number of ways. The signal efficiency as a function of neutrino energy is shown for a range of score cuts in Figure 5.21. The optimal cut is found using the unbinned likelihood method described in the next chapter (see Section 6.3.6 for cut optimization specifically). For IC86-1, the cut was set at score  $> 0.15$ . The angular resolution for the resulting selection is shown in Figure 5.22. These plots both show improving performance with increasing energy until  $\sim 10$  PeV, beyond which performance degrades slightly. This is due to worse performance of the MPE reconstruction at ultra-high energy. Finally, the effective area as a function of energy, which can be convolved with a neutrino spectrum to obtain an event rate, is shown for different zenith bands in Figure 5.23.

Because the signal window is very small in time and space, this event selection tolerates more background and less thorough data processing than selections used in other analyses such as the search for clusters of northern muon neutrinos from astrophysical point sources [97]. We obtain a larger signal efficiency and effective area with only a very moderate penalty in the neutrino purity (simulated estimate of the ratio of the atmospheric neutrino rate to the total atmospheric neutrino plus atmospheric muon rate) and in the angular resolution.

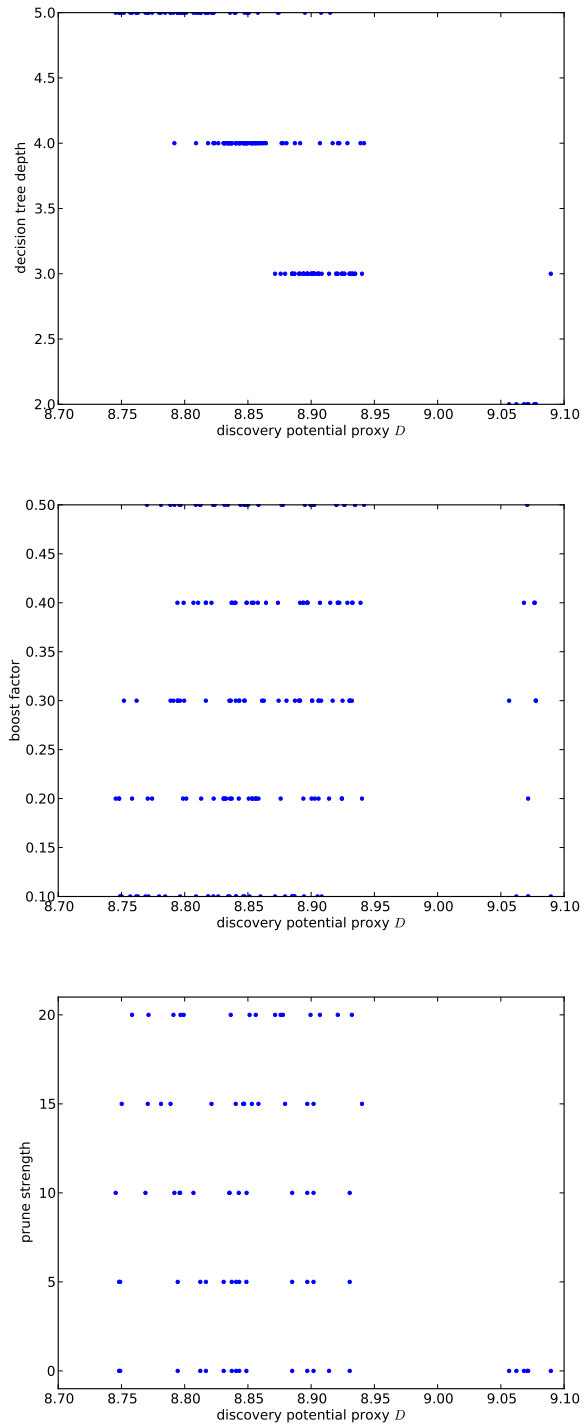


Figure 5.20: Dependence of the discovery potential (labeled MDP here for “model discovery potential”) on the boost strength (top), maximum tree depth (center) and prune strength (bottom).

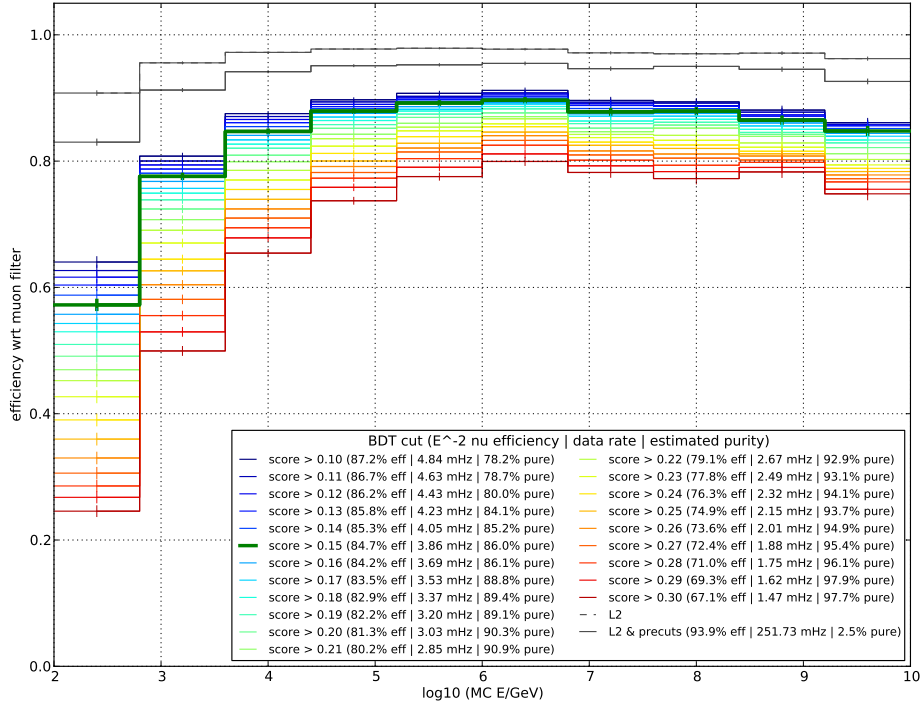


Figure 5.21: IC86-1 efficiency as a function of neutrino energy for a range of score cut values. The final optimized cut is highlighted in bold. The legend indicates overall efficiency with respect to the muon filter for well-reconstructed events with an  $E^{-2}$  spectrum, the data rate in mHz, and the purity of the sample estimated from simulation as the simulated atmospheric neutrino rate to the total atmospheric neutrino plus atmospheric muon rate.

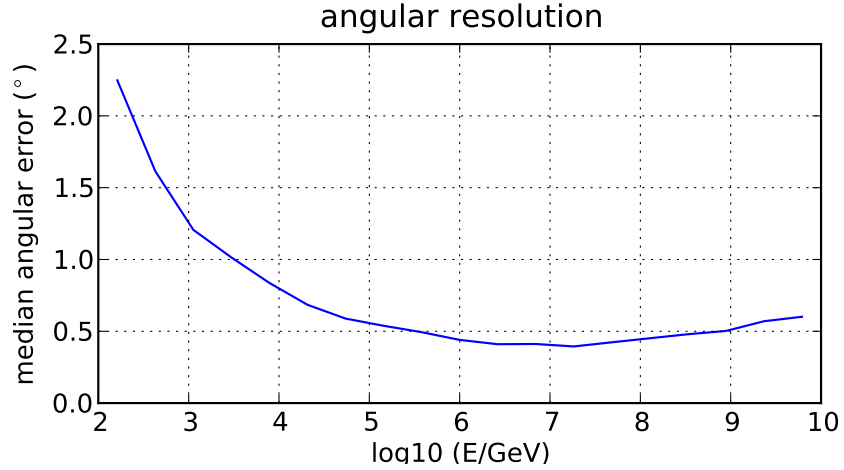


Figure 5.22: IC86-1 angular resolution as a function of energy. Specifically, we calculate the median opening angle between the true and reconstructed neutrino origin for simulated events. Note that the weaker performance at lower energies is due to both the small number of DOMs participating in reconstructions and the opening angle between the product muon and neutrino that produced it.

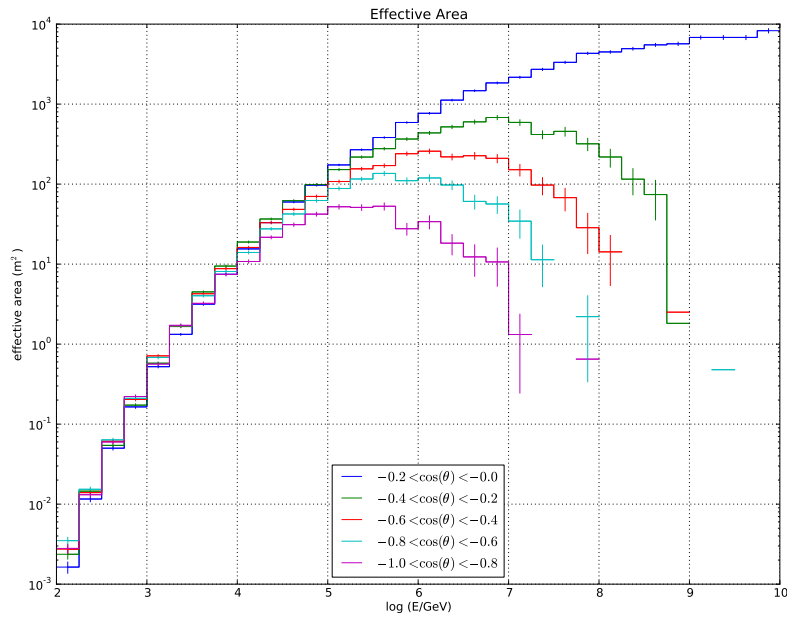


Figure 5.23: IC86-1 effective area as a function of energy for different zenith bands. Near the horizon ( $\cos \theta \approx 0$ ), the effective area is strictly increasing with energy. Closer to the North Pole, it reaches a peak and starts to decrease as absorption of neutrinos inside the Earth begins to dominate.

### 5.3.3.2 IC79 Classifier

The IC79 search was performed after the analysis of the first year of data from IC86. As a result, we were able to use lessons learned in earlier work to streamline the selection of an optimal or near-optimal decision tree classifier. Specifically, we seek to maximize the tree depth while avoiding overtraining. We do not, however, probe the training parameter space in detail. Any of a wide range of parameter choices will extract nearly all useful information from the processed data. The fine-tuning of most training parameters offers only very small improvements, typically within statistical errors.

One important improvement in the IC79 analysis chain was the addition of randomization features to `pybdt`. While the use of boosting and randomization together is unconventional, it addresses a few challenges encountered in the development of the IC86-1 classifier. Most importantly, it greatly reduces the tendency of deep trees to be overtrained even when the pruning strength is reduced. It also reduces the required number of trees and produces smoother score distributions (see again Figure 5.18).

The final classifier for IC79 used 300 trees with a maximum depth of 5. 30% of training events were used to train each tree, and 8 event features were considered at each node. The boost strength was set to 0.3 and the prune strength was set to 25%.

During the optimization of the final cut, we found that near the horizon there was a background of high energy misreconstructed events represented poorly by atmospheric muon simulation. The overall rate of these events was low, causing them to be largely ignored by the decision training algorithm. However, as we will see in Section 6.1.3, good data/MC agreement is essential in the high-energy tail because otherwise we cannot use atmospheric neutrino simulation to extend the background energy PDF. We addressed the disagreement by boosting the input



training weights of off-time data events with reconstructed energies larger than 10 TeV according to  $w_i \rightarrow w_i \cdot (\text{MuE}/10 \text{ TeV})^2$ . This modification significantly reduced the poorly simulated background with no observable effect on the bulk of the datasets.

Using the full unbinned likelihood method described in the next chapter, the final cut for IC79 was set at score  $> 0.20$  (see Section 6.3.6). The signal efficiency, angular resolution and effective area of the IC79 final selection are shown in Figures 5.24 through 5.26. The behavior is generally similar to that of the IC86-1 selection, but there are some noteworthy differences. The signal efficiency is a flatter function of energy because, while the online level 2 selection used with IC86-1 was optimized for very high energies, the muon level 3 used with IC79 was developed specifically for a broad energy acceptance. The angular resolution is slightly better for IC79, especially at ultra-high energies, because offline processing can tolerate the performance of more reconstruction iterations. The effective area is very slightly smaller in IC79.

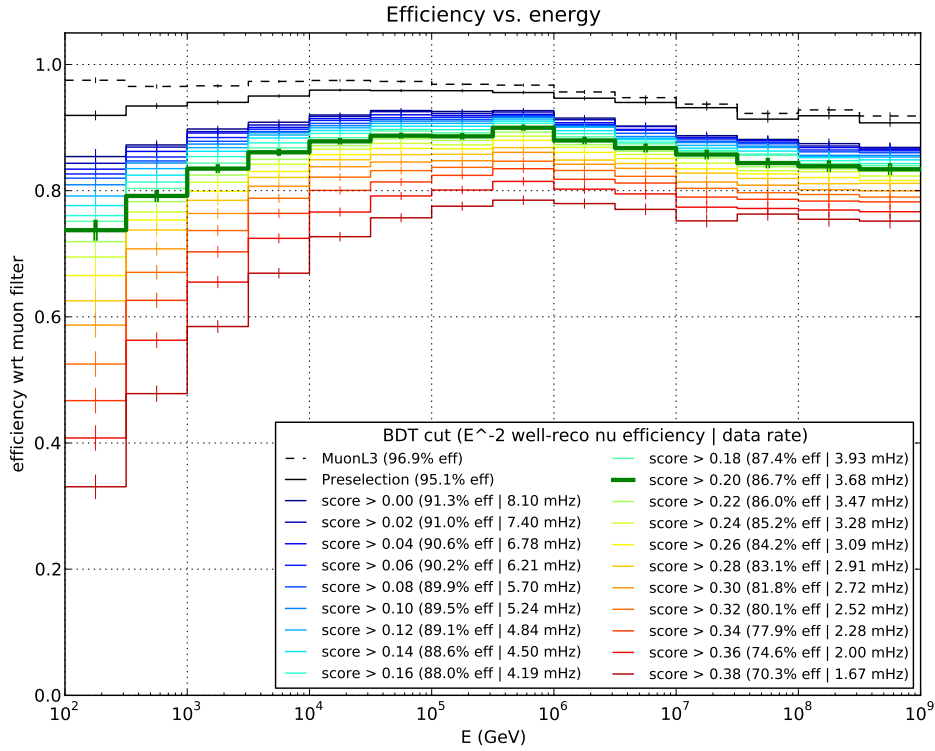


Figure 5.24: IC79 efficiency as a function of neutrino energy for a range of score cut values. The final optimized cut is highlighted in bold. The legend indicates overall efficiency with respect to the muon filter for well-reconstructed events with an  $E^{-2}$  spectrum and the data rate in mHz. The purity (not shown) is comparable to that of IC86-1.

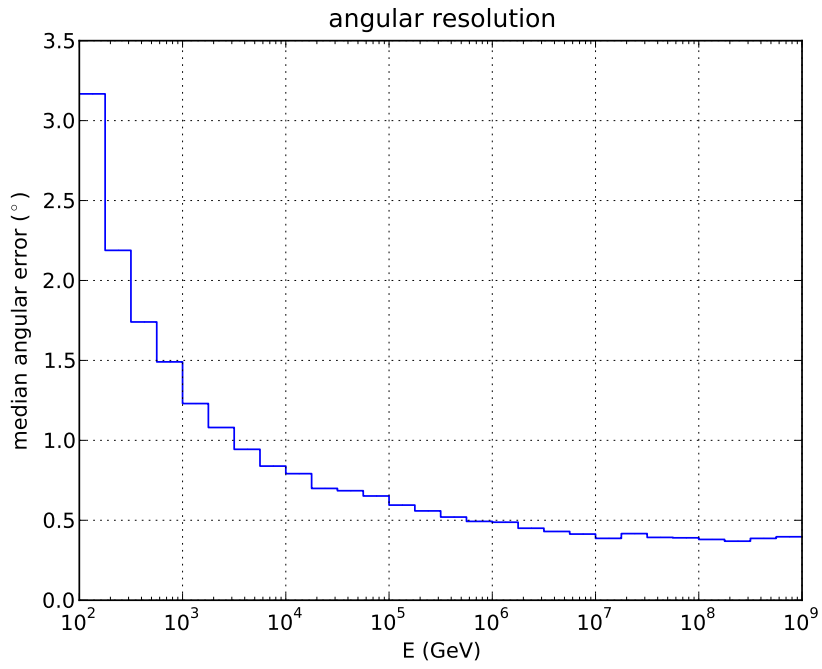


Figure 5.25: IC79 angular resolution as a function of energy.

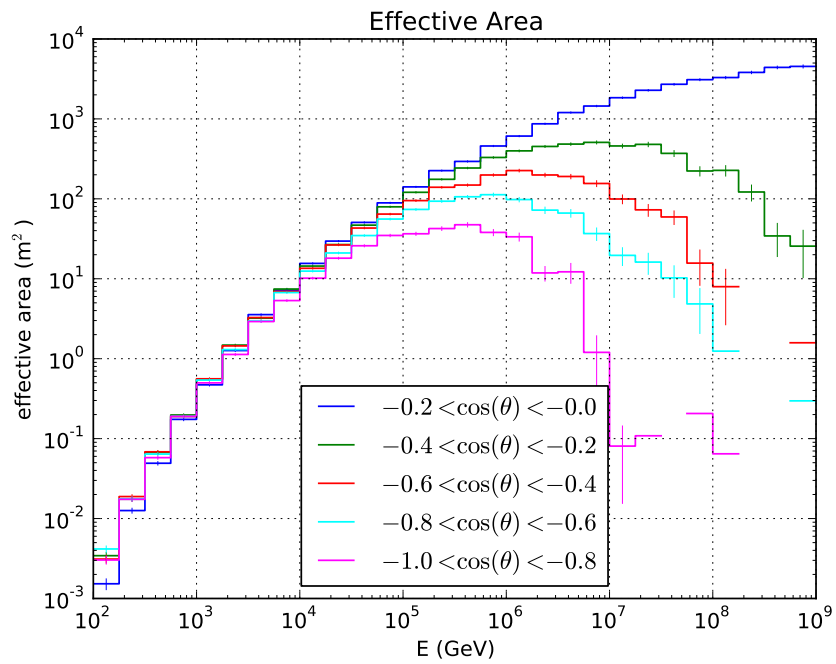


Figure 5.26: IC79 effective area as a function of energy for different zenith bands.

## Chapter 6: Unbinned Likelihood Analysis

The final event sample in this experiment consists largely of atmospheric (and possibly some astrophysical) muon neutrinos. Determining which, if any, are correlated with GRBs is an inversion problem. We would like to know the strength of the hypothetical signal, but because we expect occasional accidental correlations between atmospheric neutrinos and GRBs, we need a method that estimates the *most likely* signal strength given any particular observed ensemble of events.

One possible approach would be to conduct a simple counting experiment similar to the toy experiment used for cut optimization in the previous chapter. Any event is either inside or outside of the signal bin; for a GRB search, this would typically be a spatial and temporal window for each burst [51, e.g.]. Signal bin events are counted, and the significance of the observation relative to the expectation from background is determined using the Poisson distribution.

In this search, as in other recent Icecube GRB searches [6, 7], we instead use an unbinned analysis. Rather than placing a hard cut at the boundary of the signal region, we make estimate the probability of each individual event arising from signal or background. In this chapter, we develop these probability distribution functions (PDFs), the test statistic which gives the signal strength of the ensemble of events, and a frequentist statistical method for calculating the significance of an observed or simulated signal relative to the background expectation.

### 6.1 Probability Distribution Functions

IceCube events contain three main features which may be used to distinguish statistically between atmospheric backgrounds and a possible high-energy neutrino fluence from GRBs: time of arrival, reconstructed direction, and recon-

structed energy. These are discussed in turn below.

### 6.1.1 Time PDFs

The most straightforward PDF is the time PDF. Signal events are expected during the gamma emission, while background events are expected to be evenly distributed regardless of burst timing. Some models make detailed predictions for the neutrino “light curve”; however, the total fluence is so low that IceCube has no sensitivity to the time profile of neutrino arrival. Therefore, we assume a signal time PDF that is constant during the  $T_{100}$  for each burst. In order to have some sensitivity to events just outside the gamma measurement window and to soften the edges of the time bin to account for possible small errors in time measurement, the signal time PDF falls to zero with a Gaussian profile outside of  $T_{100}$ . The width  $\sigma_T$  of the Gaussian is set to the  $T_{100}$  of the burst, unless  $T_{100}$  is outside of the range  $[2, 30]$  seconds, in which case the width is set to the nearest edge of this range. The Gaussian is truncated<sup>1</sup> at  $4\sigma_T$  before  $T_1$  and after  $T_2$ , so the total width of the on-time window, and the domain for which the time PDFs are normalized, is  $T_{\text{search}} = T_{100} + 8\sigma_T$ . The time PDF ratio as a function of event time offset from burst T1 is shown in Figure 6.1 for sample burst durations of 0.5, 20, and 100 s.

### 6.1.2 Direction PDFs

Signal events are expected to originate from the burst location in the sky, within the reconstruction uncertainties of the burst and the neutrino. Previous searches have used a circular two-dimensional Gaussian signal direction PDF. In those searches, the Gaussian had a width of  $\sigma_{\text{direction}} = \sqrt{\sigma_\nu^2 + \sigma_{\text{GRB}}^2}$ . In light of

---

<sup>1</sup>The choice of cutoff here is arbitrary; in Section 6.2 we will see why this choice has a negligible effect on the analysis.

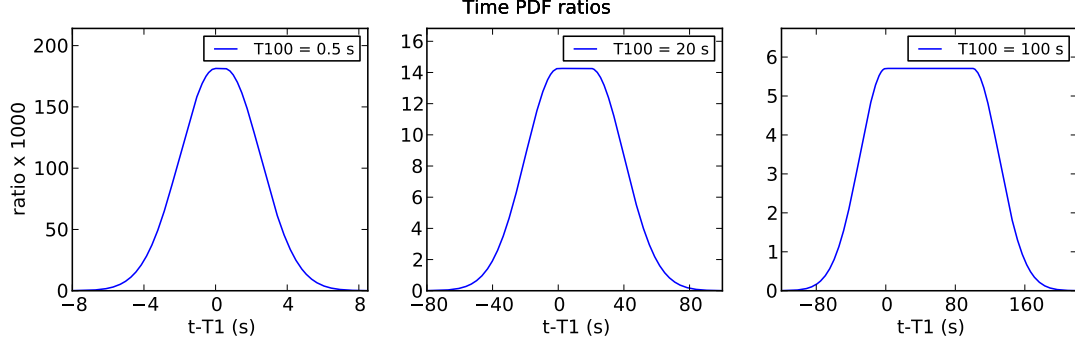


Figure 6.1: Time PDF ratio as a function of event time offset from burst T1 for sample burst durations.

the poor localization of Fermi GBM bursts and in anticipation of future searches involving poorly-localized cascade-signature neutrino events, the analysis code has been updated to make use of the first-order term in the Kent distribution [98]. This distribution is analogous to a Gaussian distribution, but its domain is a sphere rather than an infinite plane. Substituting  $\kappa = 1/\sigma_{\text{direction}}^2$ , the signal space PDF can be expressed as

$$S_{\text{direction}} = \frac{\kappa}{4\pi \sin \kappa} \exp[\kappa \cos(\Delta\Psi(\text{event}, \text{GRB}))] \quad (6.1)$$

Fermi-GBM burst localization errors are best described by combining per-burst statistical errors in quadrature with a systematic error that was studied using bursts that were better localized by other satellites such as Swift. The systematic error can be modeled as a weighted sum of Gaussian errors:  $2.6^\circ$  with 72% weight and  $10.4^\circ$  with 28% weight. For GRBs only localized by Fermi-GBM, our analysis code accounts for this relatively large systematic error by propagating it into the

direction PDF:

$$\kappa_{2.6} = \frac{1}{\sigma_\nu^2 + \sigma_{\text{GBM,stat}}^2 + (2.6^\circ)^2} \quad \text{and} \quad \kappa_{10.4} = \frac{1}{\sigma_\nu^2 + \sigma_{\text{GBM,stat}}^2 + (10.4^\circ)^2}; \quad (6.2)$$

$$S_{\text{direction}} = 0.72 \times S_{\text{direction}}^{\kappa_{2.6}} + 0.28 \times S_{\text{direction}}^{\kappa_{10.4}}. \quad (6.3)$$

The rate of background events varies with declination due primarily to three effects:

1. The detector geometry prefers horizontal events which tend to pass nearby more strings.
2. Atmospheric neutrino absorption is more likely with increased path length through the Earth.
3. Coincident and corner-clipping cosmic ray muon backgrounds are more readily rejected when reconstructed as more upgoing, and less readily rejected when reconstructed as more horizontal.

All three of these effects lead to a higher background rate near the horizon than near the North Pole. The hexagonal grid geometry of the detector also leads to an azimuthal asymmetry in the background rate, but since it varies by  $\lesssim 20\%$ , it is negligible for this analysis. Therefore, the background direction PDF is a spline fit to the normalized histogram of event declination values, as shown in Figure 6.2.

### 6.1.3 Energy PDFs

Popular GRB models imply a prompt neutrino spectrum that is harder (less steeply falling with energy) than the atmospheric neutrino spectrum. Therefore, reconstructed event energy is a powerful third quantity with which to distinguish between atmospheric backgrounds and a possible signal. The use of energy

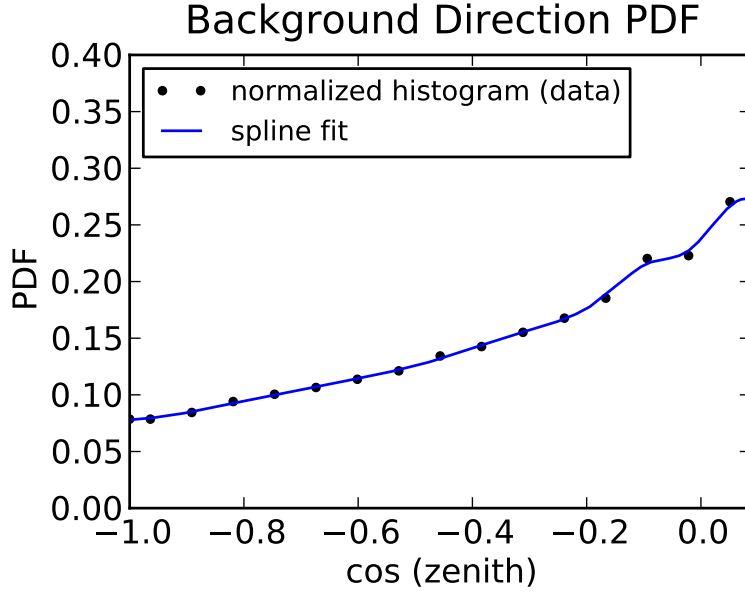


Figure 6.2: Background direction PDF. The normalized histogram of reconstructed zenith for off-time data events is shown as black dots; a spline fit, shown as a blue curve, is used to evaluate the function for a given reconstructed zenith. In detector coordinates, the North Pole is at zenith = 180°. Since IceCube is positioned so close to the geographic South Pole, declination corresponds closely to zenith: declination = 180° – zenith.

PDFs simultaneously allows better sensitivity to a high energy signal and better resilience against atmospheric background events than a simple counting experiment could provide.

The energy PDFs are functions of the MuE reconstructed energy. This analysis is optimized for a signal hypothesis of an  $E^{-2}$  spectrum. This is a conservative choice, as present models (see Chapter 2) give even harder spectra. The signal energy PDF is the normalized histogram of reconstructed energies of neutrino simulation weighted to an  $E^{-2}$  spectrum.

The background energy PDF requires a more complex treatment. In most aspects of this experiment, the background is characterized exclusively using off-time data. However, to allow for high weighting of a possible ultra-high energy signal, the background energy PDF must be extended to higher energies than the



statistics in the off-time data sample allow. This requires the use of background simulation. In this analysis, atmospheric neutrinos are the dominant background, so atmospheric neutrino simulation is used to extend the background energy PDF to very high energies. This approach is only justified by close data/MC agreement near the transition between datasets. To obtain a continuous and smooth background PDF, a small correction factor is applied to the high energy tail to align it with the rest of the distribution.

Numerically, the energy PDF ratio is treated as a single function: a spline fit to the ratio of the normalized MuE distributions for signal and background, as shown in Figure 6.3

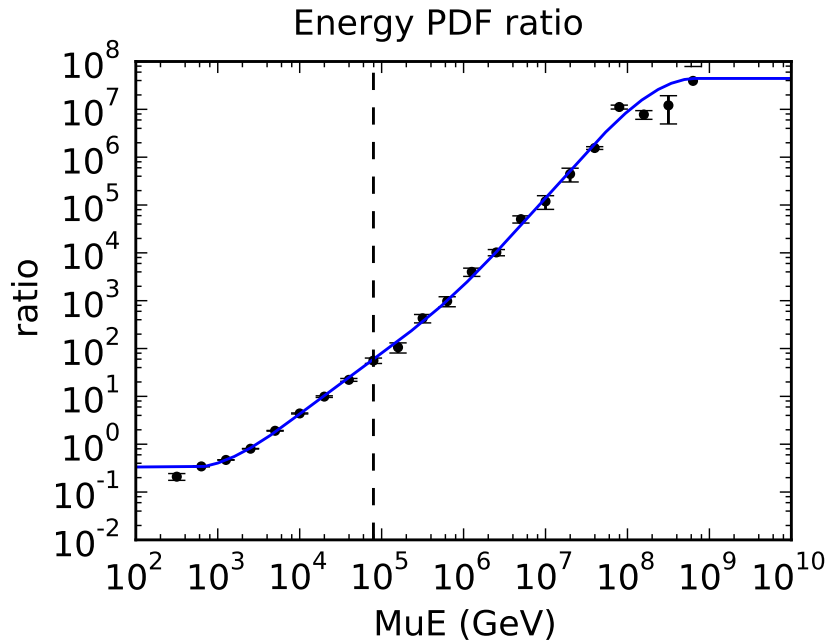


Figure 6.3: Signal-to-background energy PDF ratio as a function of reconstructed muon energy. The black dots show the ratio of separately-normalized MuE histograms in simulated signal and in backgrounds. Backgrounds are measured in off-time data below  $\sim 10^5$  GeV and in atmospheric neutrino simulation at higher energies. The transition is indicated by the dashed black line. A spline fit to the ratio of histograms, shown as a blue curve, is used to evaluate the PDF ratio for a given value of MuE.

## 6.2 Test Statistic

The test statistic is the quantity used to compare hypothetical or actually observed experimental outcomes with each other. In a counting experiment, the test statistic is the number of events observed. In an unbinned analysis, the test statistic is derived from a likelihood ratio that is used to find the best fit signal rate for a given set of observed events.

Let  $N$  represent the number of events observed and  $n_s + n_b$  represent the expected total rate of signal plus background events. The probability of observing  $N$  events is given by the Poisson distribution:

$$P_{\text{Poisson}}(N; n_s + n_b) = \frac{(n_s + n_b)^N}{N!} \cdot \exp(-(n_s + n_b)). \quad (6.4)$$

Now let  $x_i$  represent the properties of observed event  $i$ ,  $P(x_i)$  represent the probability density of observing an event with properties  $x_i$ , and  $\{x_i\}$  represent the set of events. The likelihood of seeing the set of events  $\{x_i\}$  given an expected rate  $n_s + n_b$  is the product of  $P_{\text{Poisson}}$  and the per-event probability densities:

$$\mathcal{L}(N, \{x_i\}; n_s + n_b) = \frac{(n_s + n_b)^N}{N!} \cdot \exp(-(n_s + n_b)) \cdot \prod_{i=1}^N P(x_i). \quad (6.5)$$

Taking the natural logarithm, this can be expressed as

$$\ln \mathcal{L}(\{x_i\}; n_s + n_b) = -n_s - n_b - \ln N! + \sum_{i=1}^N \ln[(n_s + n_b)P(x_i)]. \quad (6.6)$$

Note that the probability of measuring a signal event is  $n_s/(n_s + n_b)$ , and likewise the probability of measuring a background event is  $n_b/(n_s + n_b)$ . Let  $S(x_i)$  be the probability density for event  $i$  with properties  $x_i$  to be a signal event; likewise, let  $B(x_i)$  be the probability density for event  $i$  to be a background event. Then the

normalized probability density  $P(x_i)$  of observing event  $i$  can be written as

$$P(x_i) = \frac{n_s S(x_i) + n_b B(x_i)}{n_s + n_b}. \quad (6.7)$$

Substituting this into (6.6), we obtain

$$\ln \mathcal{L}(\{x_i\}; n_s + n_b) = -n_s - n_b - \ln N! + \sum_{i=1}^N \ln[n_s S(x_i) + n_b B(x_i)]. \quad (6.8)$$

In this analysis, we measure the background expectation  $\langle n_b \rangle$  using off-time data, so we can remove  $n_b$  from the argument to the likelihood function:

$$\ln \mathcal{L}(\{x_i\}; n_s) = -n_s - \langle n_b \rangle - \ln N! + \sum_{i=1}^N \ln[n_s S(x_i) + \langle n_b \rangle B(x_i)]. \quad (6.9)$$

The background-only likelihood is obtained by setting  $n_s = 0$ :

$$\ln \mathcal{L}_0(\{x_i\}) = -\langle n_b \rangle - \ln N! + \sum_{i=1}^N \ln[\langle n_b \rangle B(x_i)]. \quad (6.10)$$

The best-fit  $n_s$  for an observed ensemble of events is found by finding the value  $\hat{n}_s$  which maximizes  $\mathcal{L}$ . Since  $\mathcal{L}_0$  is independent of  $n_s$  and the logarithm is a monotonic function, the best-fit  $\hat{n}_s$  is also the value which maximizes  $\ln(\mathcal{L}/\mathcal{L}_0)$ .

This log likelihood ratio is our test statistic  $T$ :

$$T := \ln \left[ \frac{\mathcal{L}(\{x_i\}; \hat{n}_s)}{\mathcal{L}_0(\{x_i\})} \right] = -\hat{n}_s + \sum_{i=1}^N \ln \left[ \frac{\hat{n}_s S(x_i)}{\langle n_b \rangle B(x_i)} + 1 \right]. \quad (6.11)$$

$T$  is well-suited for comparing different possible or observed experimental outcomes because it includes information about both the number of signal events and the extent to which they are more likely to be signal than background.

In this analysis,  $S(x_i)$  and  $B(x_i)$  are composed of the PDFs detailed in

Section 6.1. Specifically,

$$S(x_i) = S_{\text{time}}(t_i) \cdot S_{\text{direction}}(\vec{x}_i) \cdot S_{\text{energy}}(E_i); \quad (6.12)$$

$$B(x_i) = B_{\text{time}}(t_i) \cdot B_{\text{direction}}(\vec{x}_i) \cdot B_{\text{energy}}(E_i). \quad (6.13)$$

The use of the likelihood ratio in deriving (6.11) avoids any ambiguity due to the choice of units and scale (i.e. linear vs logarithmic) in the PDFs.

Note that (6.11) makes clear why it is appropriate to truncate the time PDFs somewhat arbitrarily at  $\pm 4\sigma_T$ . Far from any burst time window,  $S_{\text{time}} \approx 0$ . Thus the truncation only changes the normalization of  $B_{\text{time}}$ ; a different choice of cutoff would be balanced by a commensurate change in  $\langle n_b \rangle$ , leaving the overall likelihood function unchanged.

### 6.3 Frequentist Method

We use frequentist statistics to characterize the performance of the analysis and to calculate fluence constraints and statistical significances from actual observations. In this approach, the significance of an observed test statistic  $T_{\text{obs}}$  is the probability of obtaining an equal or larger value based on a distribution calculated by MC generation of background-like pseudo-experiments. The response of the analysis to a possible signal is studied using MC generation of pseudo-experiments containing both typical ensembles of background events and simulated neutrino signal events. Below we discuss the MC injection of events into pseudo-experiments and the application of this method to analysis optimization and the calculation of neutrino fluence constraints.

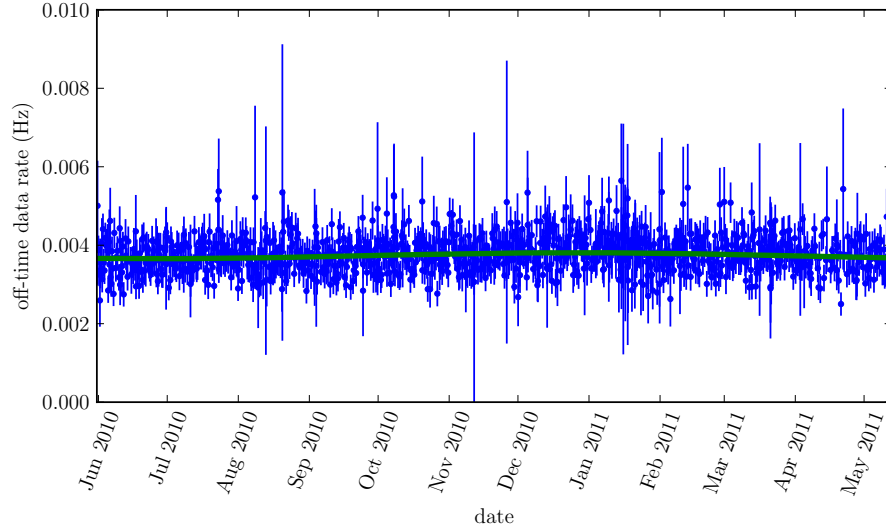


Figure 6.4: Seasonal variation of the background rate in IC79. In previous work [99,100] the overall average rate was used in the unbinned likelihood method, and the rate variation was treated as a systematic error. Here, we avoid this problem by directly accounting for the small variation of the rate.

### 6.3.1 Randomized Background Injection

Pseudo-experiments are constructed by *injecting* events and calculating the resulting  $T$ . While the true signal strength is not known and may be zero, this experiment is guaranteed to be subject to background. Therefore, all pseudo-experiments require the injection of background-like events. The properties of the background-like events are measured using off-time data events.

The expected rate is determined by counting the number of events in each detector run. In order to account for the small seasonal variation in the background, the rate is fit with a spline as a function of time. An example fit for the IC79 season is shown in Figure 6.4. The resulting function is used to calculate  $\langle n_b \rangle_m$  for each burst  $m$ . The total background rate is

$$\langle n_b \rangle = \sum_{m=1}^{N_{\text{burst}}} \langle n_b \rangle_m. \quad (6.14)$$

For each pseudo-experiment, the number of background events is determined

by randomly sampling the Poisson distribution for each burst’s expected background rate:

$$P_{\text{Poisson}}(N_m; \langle n_b \rangle_m) = \frac{\langle n_b \rangle_m^{N_m}}{N_m!} \cdot \exp(-\langle n_b \rangle_m). \quad (6.15)$$

Then the properties of each pseudo-event are constructed by randomly sampling distributions measured in the data. First a MuE energy value is chosen by randomly sampling the off-time data MuE distribution. Off-time data events are divided according to their MuE values into 10 bins with equal statistics in each bin. A zenith value is chosen by randomly sampling the zenith distribution for the energy bin corresponding to the chosen MuE. An azimuth value is assigned by selecting a random value between 0 and  $2\pi$ . The events in each energy bin are further divided into 10 bins according to zenith, again ensuring equal statistics in each bin. The angular error estimate is chosen by sampling the Cramer-Rao distribution for the energy and zenith bin corresponding to the chosen MuE and zenith values. The energy and zenith distribution and the bins used for random sampling are shown in Figure 6.5. Finally, the time offset of the event within  $T_{\text{search}}$  is randomly chosen. Once the pseudo-events are constructed, their PDF values are calculated.

### 6.3.2 Randomized Signal Injection

In order to generate pseudo-experiments containing signal-like events, simulated neutrino events are used. General-purpose datasets contain events distributed evenly throughout the sky. To represent GRBs, which are point-like, simulated events within  $11^\circ$  of each burst location are selected (1% of the sky) as described in Section 4.3.1.

Event weights from neutrino-generator are constructed such that the sum of

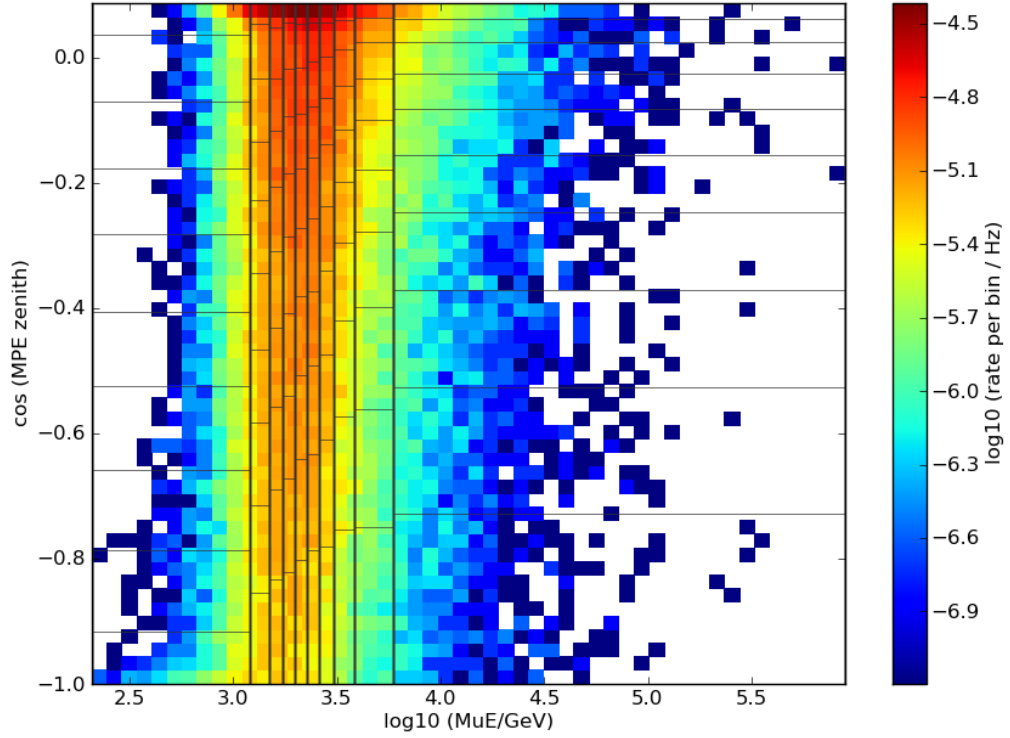


Figure 6.5: Energy and zenith distributions with bins used for generating pseudo-events.

the weights of simulated events gives the rate of such events. The weight  $w_i$  of an individual event, which is calculated using (4.17), can be treated as the Poisson rate for the occurrence of that event. The rates are very small, so the probabilities of the event occurring exactly zero or one time dominate. Therefore the probability of a signal event being injected is given by

$$p_i = \frac{w_i^1}{1!} \cdot e^{-w_i} \approx w_i. \quad (6.16)$$

In each pseudo-experiment, a random number between 0 and 1 is chosen for each event; if it is less than  $w_i$ , the event is injected.

### 6.3.3 Significance

The test statistic is used to determine the significance of an observed ensemble of events. The significance is defined as the probability of obtaining an equal or greater test statistic value from background events if the true signal strength is zero. Typically, the significance is expressed as a number of sigmas, which relates it to the Gaussian distribution. Specifically, the number of sigmas  $n_\sigma$  is given by the inverse survival function of the Gaussian distribution, evaluated at the probability  $p$ .

The background-only  $T$  distribution is obtained by performing  $10^9$  pseudo-experiments with no signal injection. The distribution is shown in Figure 6.6. In particle physics, the threshold for a discovery claim is set conventionally, if somewhat arbitrarily, at  $5\sigma$ . In order to determine the  $5\sigma$  threshold with good statistical precision,  $10^9$  background-only pseudo-experiments are performed.

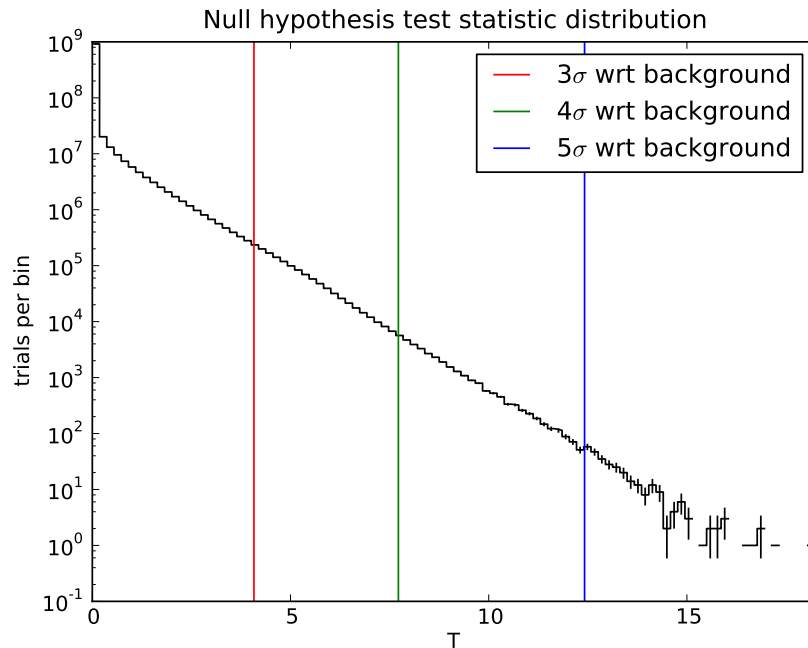


Figure 6.6: Background-only test statistic distribution.



### 6.3.4 Discovery Potential

The discovery potential is a measure that quantifies the signal strength needed to obtain a significant result given the simulated signal acceptance and measured backgrounds. It is defined as the signal normalization which yields a  $5\sigma$  result with respect to the background expectation in 50% of signal-injected pseudo-experiments. This quantity is found using a minimization routine which performs  $\mathcal{O}(10^4)$  pseudo-experiments for each signal normalization tested until the  $5\sigma$  threshold is exceeded by 50% of trials. The resulting signal normalization is determined within a tolerance of 0.01%, provided that the number of trials is sufficient to avoid fluctuations that disturb the minimization algorithm.

A related quantity is the least detectable signal (LDS): the signal normalization which yields a  $5\sigma$  result in 90% of trials. The discovery potential and LDS are useful for optimizing an analysis. The analysis is performed with the hope of observing a significant result, and the discovery potential and LDS quantify the signal strength required to do so. Therefore, these are the quantities that are used to determine whether a modification, e.g. changing the reconstructions that are used, improves or degrades the analysis. In particular, they are useful for determining the optimal final classifier score cut. The optimization curves for IC79 and IC86-1 are shown in Figure 6.7. The final neutrino level cut is the loosest one which optimizes the discovery potential and LDS.

### 6.3.5 Upper limits

Upper limits are calculated in a similar manner as the discovery potential and LDS. The exclusion confidence level (CL) for a given signal normalization is the fraction of trials which yield  $T > T_{\text{obs}}$ . For optimization purposes, the sensitivity is defined as the average 90% CL upper limit, weighted using the background-only  $T$  distribution as in Figure 6.6. This is a very low background experiment,

with almost 90% of background-only pseudo-experiments yielding  $T = 0$ . Therefore, the sensitivity is approximately equal to the best possible upper limit: the limit obtained supposing that  $T_{\text{obs}} = 0$ . It is possible to optimize an analysis for sensitivity rather than for discovery potential. The best possible limit as a function of BDT score cut is shown for each detector configuration in Figure 6.8.

### 6.3.6 Final Optimized Cuts

For both detector configurations, the discovery potential and sensitivity optima are well-correlated. Based on Figures 6.7 and 6.8, the final neutrino level cuts were placed at scores of 0.20 and 0.15 for IC79 and IC86-1, respectively. These are the loosest cuts that still approximately optimize for both discovery and sensitivity. We prefer this over the central value or an even tighter cut because, while a discovery would be excellent news, the complete absence of a signal in all past searches means that we would prefer *a priori* to let borderline events participate in the likelihood analysis rather than be cut outright.

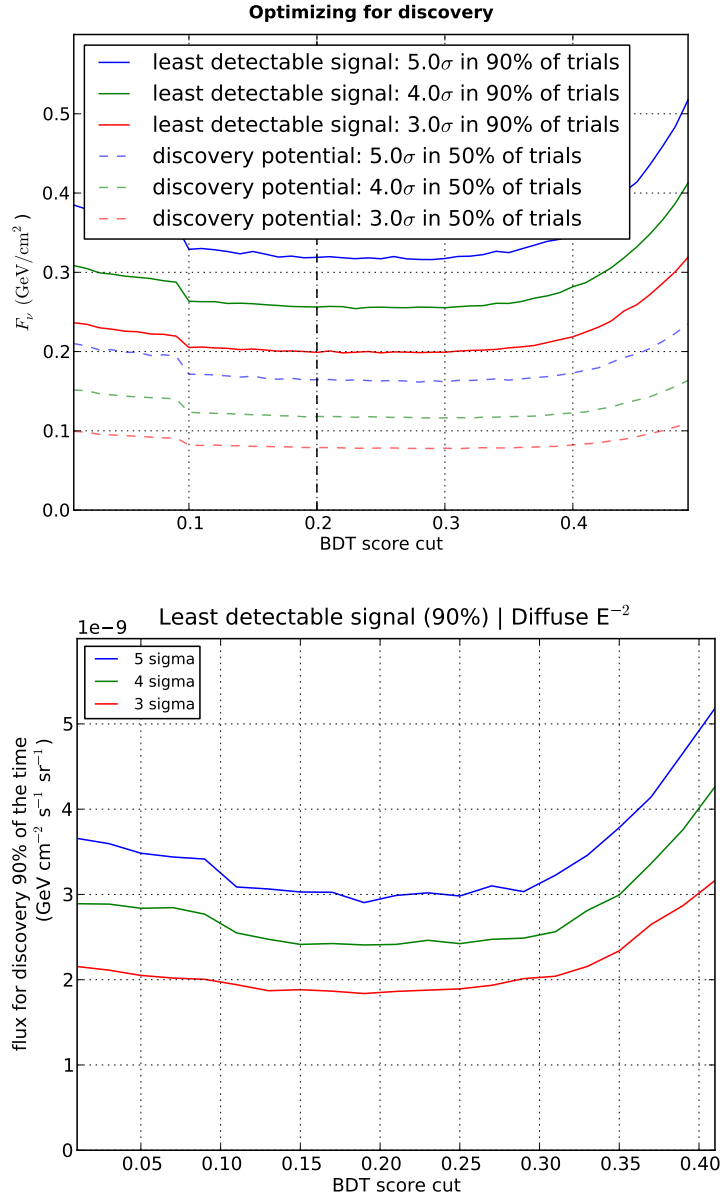


Figure 6.7: Optimizing the IC79 (top) and IC86-1 (bottom) final neutrino level cuts for discovery. Generally the statistical power — 50% for discovery potential and 90% for the LDS — alters the normalization of the curves but not their shapes. Both are plotted for IC79; only the LDS is plotted for IC86-1. The vertical axis for IC79 is the total fluence, while for IC86-1 it is scaled as a quasi-diffuse flux based on an assumed 667 bursts throughout the sky in any given year. The optima are very broad; this is encouraging prior to unblinding of the on-time dataset because it means that the results should not change dramatically if we second-guess the final cut value later. For IC79, we require scores greater than 0.20; for IC86-1, the threshold is 0.15.

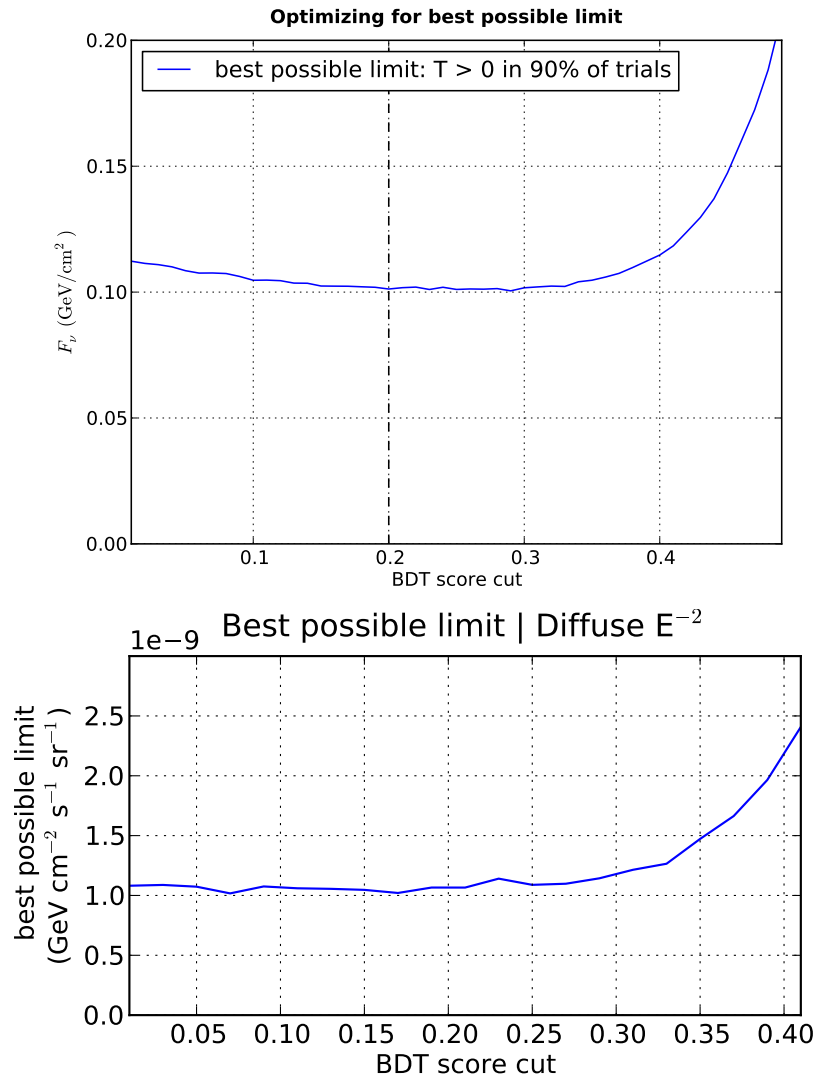


Figure 6.8: Optimizing the IC79 (top) and IC86-1 (bottom) final neutrino level cuts for sensitivity. As was the case when optimizing for discovery (Figure 6.7), the optima are very broad.

## Chapter 7: IC40 through IC86 Year 1 Constraints

In four years of data, a single low-significance muon track event was associated with a northern hemisphere GRB. In this chapter, we begin by extending the unbinned likelihood method introduced in the previous chapter so that it can be used for the multi-year combined analysis. We briefly present the significance of the result, which is consistent with the expectation from background. Then we present methods for estimating the systematic errors introduced by the use of signal simulation to calculate fluence constraints. Finally, we present the most stringent limits to date on the model scenarios discussed in Chapter 2.

### 7.1 Multi-year Unbinned Likelihood Analysis

In the IC40 and IC59 datasets, no events were observed in connection with any GRBs [6, 7]. For this reason, it was straightforward to interpret the data using a Poisson statistics approximation [100]. With the introduction of a GRB-correlated event, results should be obtained using a multi-year unbinned likelihood analysis.

#### 7.1.1 Method

Following the discussion in section 6.2, it is statistically valid to fit the total number of signal events  $n_s$  given the total measured background rate  $\langle n_b \rangle$ , provided that the PDFs  $S(x_i)$  and  $B(x_i)$  are derived from the year corresponding to each event. However, this simple treatment has two undesirable characteristics. First, because stacking additional years does not change the per-event PDF values but does increase  $\langle n_b \rangle$ , a  $T > 0$  result for a single year can become exactly  $T = 0$  when stacked with additional years. Second, a correlated event should be weighted more strongly if it occurs during a low background year, but the simple approach

compares every event to the *total* stacked background.

Therefore, we instead apply (6.11) to each detector configuration individually, obtaining separate  $T_c$  for each configuration  $c$ . The multi-year test statistic is:

$$T = \sum_c T_c = \sum_c \left\{ -(\hat{n}_s)_c + \sum_{i=1}^{N_c} \ln \left[ \frac{(\hat{n}_s)_c S_i}{\langle n_b \rangle_c B_i} + 1 \right] \right\}. \quad (7.1)$$

This addresses both concerns above; a non-null result for one season remains non-null regardless of subsequent stacking with later seasons, and each event is evaluated in the context of the background for the detector configuration which observed the event. The latter point is not as important for a track-only search, but in future combined track-cascade results, it will be needed in order for cascades to contribute.

The method described here and in Chapter 6 was implemented in an original software package called `grb11h` for the purposes of this work. An appropriately general interface was designed by a small group and implemented by me to meet not only the immediate needs of the present search but also those of other analyses that are currently being developed. As with `pybdt`, the user interface is written entirely in Python, but it employs a fast backend written in C++ for efficient Monte Carlo calculation of significances, discovery potentials, sensitivities, and model constraints.

### 7.1.2 Result

The final test statistic is equal to that found for IC79:  $T = 0.1330$ . Following the approach described in Section 6.3.3, we obtain the significance  $p = 0.33$  ( $0.44\sigma$ ). The background-only test statistic distribution and the final result are shown in Figure 7.1.

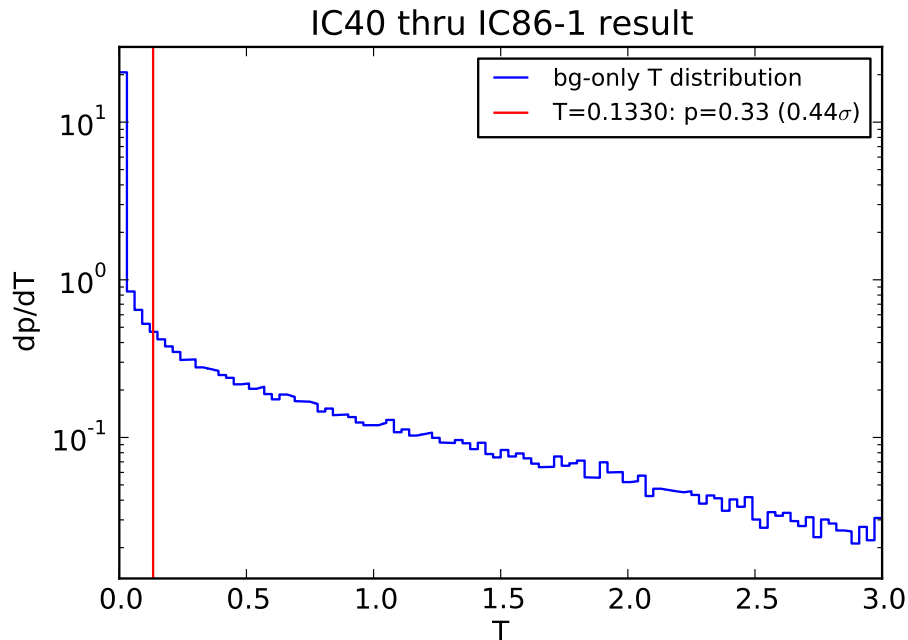


Figure 7.1: Background-only test statistic distribution for IC40 thru IC86-1 with the observed test statistic shown in red.

## 7.2 Systematic Errors

Since this analysis detects no excess of neutrinos correlated with GRBs, the final result is a Feldman-Cousins upper limit on the neutrino fluence. In general, the result is subject to systematic errors in the measured background and the simulated signal. However, since the off-time data used to characterize the background represents a much larger detector livetime than the on-time search window, errors due to background fluctuation are negligible. Signal simulation is subject to systematic errors due to uncertainties in the properties of the detector, its geological environment, and the standard model. These uncertainties propagate into the calculated limits by modulating the neutrino flux arriving at the detector as well as the amount of charge recorded by the DOMs.

In the following sections, specific sources of systematic error are discussed. Some error sources are studied using special simulation datasets with modified

settings. At the time of this writing, the most mature such datasets were produced for the IC79 detector configuration. Therefore, these errors are calculated by comparing the IC79-only limits that can be derived using the special datasets to the limit derived using the baseline dataset. In general, the error in the limit is dominated by effects on lower energy events which may be cut under less optimistic simulation settings. Thus the magnitude of each effect is spectrum dependent: softer spectra are subject to larger systematic errors. Where errors are calculated using special simulation, fireball model scenarios are treated separately and a benchmark bulk Lorentz factor  $\Gamma = 300$  is used. To estimate the error in the generic broken power law model, we calculate the error for an  $E^{-2}$  spectrum and conservatively apply the resulting value to the entire range of  $E^{-1}/E^{-2}$  break energies.

### 7.2.1 Optical Module Efficiency

The quantum efficiency of the DOMs scales the charge recorded for a given amount of light incident on the PMTs. Reducing the DOM efficiency can degrade the direction and energy reconstruction of events by decreasing the amount of charge observed and the number of DOMs participating in the reconstructions. These effects in turn reduce the number of events passing the final cut and reduce the power of the remaining events in the likelihood analysis.

The uncertainty of the DOM efficiency relative to the baseline simulation is conservatively estimated to be  $\pm 10\%$ . To determine the effect of this uncertainty on the limit, separate signal simulation is generated with higher and lower DOM efficiency settings. The results are summarized in Table 7.1



Dataset	Description	Effect relative to baseline (%)			
		ICMART	Standard	Photospheric	$E^{-2}$
9195	DOM efficiency $-10\%$	+2.1	+1.4	+1.8	+4.0
9168	DOM efficiency $+10\%$	-1.5	-2.5	-2.6	-4.3

Table 7.1: DOM efficiency systematic error summary for fireball model scenarios and for an  $E^{-2}$  spectrum.

Dataset	Description	Effect relative to baseline (%)			
		ICMART	Standard	Photospheric	$E^{-2}$
9179	Abs. & Scatt. $+10\%$	+1.7	+1.2	+2.1	+1.7
9180	Abs. & Scatt. $-10\%$	-3.5	-5.3	-5.0	-5.0

Table 7.2: Ice model systematic error summary for fireball model scenarios and for an  $E^{-2}$  spectrum.

## 7.2.2 Photon Propagation in Ice

The South Pole ice modulates the amount of light arriving at the DOMs through absorption and the quality of light arrival time information through scattering. The absorption and scattering profiles are measured as a function of depth using the flashers deployed on the DOMs. The errors on these fits are estimated to be  $\pm 10\%$ . Special simulation datasets were produced with these quantities varied together by  $\pm 10\%$ . The results are summarized in Table 7.2

## 7.2.3 Other Errors

In addition to errors that affect the charge measured for a given light deposition, neutrino simulation is subject to several errors earlier in the simulation chain. The interaction cross section for IceCube’s energy range of interest can only be inferred indirectly, as these energies have not been reached in laboratory measurements. Cross section uncertainties yield competing effects, with a higher cross section causing increased absorption in the Earth but a higher probability of interaction for events which successfully traverse the Earth. Uncertainties in

Description	Effect relative to baseline (%)			
	ICMART	Standard	Photospheric	$E^{-2}$
DOM efficiency $-10\%$	+2.1	+1.4	+1.8	+4.0
Absorption & Scattering $+10\%$	+1.7	+1.2	+2.1	+1.7
Other errors	+8	+8	+8	+8
Total	+8.5	+8.2	+8.50	+9.1

Table 7.3: Total systematic errors for fireball model scenarios and for an  $E^{-2}$  spectrum.

muon energy losses during propagation through the ice scale the amount of light deposited near the detector. Finally, uncertainties in the rock density near the detector scale the probability of a neutrino successfully passing through to produce a muon in the ice. For vertically up-going events and an  $E^{-2}$ , these effects contribute a maximum  $\sim 8\%$  uncertainty in the neutrino rate [101]. Vertically up-going events are the most affected by these sources of error. At the time of this writing, detailed simulation of these effects for the full Northern sky has not been produced. Therefore, we accept a minor loss of sensitivity by applying this value to all events and all model spectra.

#### 7.2.4 Total Systematic Error

We are interested in upper limits on the neutrino fluence. For the purposes of this result, we are therefore only interested in effects which degrade the limit. The total systematic error is obtained by adding the DOM efficiency, ice model errors, and all other errors in quadrature. The results are shown in Table 7.3. Systematic errors are included in all results presented in the following section.

### 7.3 Model Constraints

First we consider the top-down models parameterized in (2.5). There we have a total flux normalization  $\Phi_0$  in units  $\text{GeV}^{-1} \text{cm}^{-2} \text{sr}^{-1} \text{s}^{-1}$ . To evaluate

constraints using the prescription in Section 6.3.5, we need a per-burst fluence normalization  $F_0$  in units  $\text{GeV}^{-1} \text{cm}^{-2}$ . We assume that the 506 bursts analyzed in the combined search are representative of  $n_{\text{GRB}}$  bursts per year that are *potentially observable* by existing satellites. Potentially observable bursts can go unseen because they are hidden by the sun or moon; they occur outside the field of view of any satellite or during satellite downtime; or in this analysis, because they are in the southern sky. While the observable burst rate has an uncertainty up to a factor of  $\sim 2$ , here we assume  $n_{\text{GRB}} = 667$  as has been done in previous IceCube publications [7,102]. Then each burst yields a spectrum with break energies  $\varepsilon_b$  and  $10\varepsilon_b$  as in (2.5), and the per-burst normalization used to weight the simulation is

$$F_0 = \frac{4\pi \cdot 365.25 \cdot 86400 \text{ s}}{n_{\text{GRB}}} \Phi_0. \quad (7.2)$$

We then evaluate exclusion CL contours in the  $\varepsilon_b - \varepsilon_b^2 \Phi_0$  plane by applying the method described in Section 6.3.5 to a grid of choices for these parameters. The results are shown along with model predictions in Figure 7.2. We take the systematic uncertainty for an  $E^{-2}$  as an approximate estimate of the uncertainty for these models. The error is incorporated into Figure 7.2 as a shift in the vertical axis.

Next we consider bottom-up models with example spectra shown in Figures 2.4 through 2.6. Baerwald et al. [55] construct fully self-consistent models of the UHECR–gamma-ray–neutrino connection, finding that while neutron escape is strongly excluded by existing limits, some parameter spaces remain which could allow GRBs to be dominant UHECR sources. For the standard case as well as for the photospheric and ICMART neutrino flux models, we consider baryonic loading of  $1 < f_p < 200$ . For the standard and photospheric cases, we test  $100 < \Gamma < 950$ , while for ICMART we test  $50 < \Gamma < 400$ . In general, our constraints are weaker

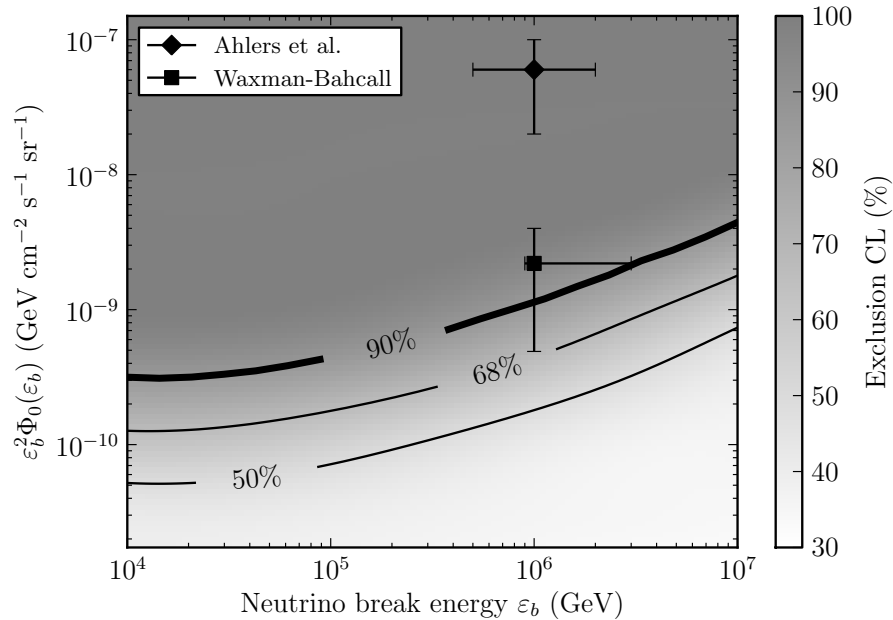


Figure 7.2: Exclusion contours showing constraints on top-down models that predict a doubly-broken power law spectrum. Neutron escape [58] is strongly excluded by our current limits; more optimistic models allowing proton escape [56] are in tension with our observations but not yet strongly excluded.

for larger  $\Gamma$ ; since ICMART predicts a reduced neutrino flux, we do not extend the scan to higher  $\Gamma$  where IceCube cannot place meaningful limits. The exclusion contours for these scans are shown in Figures 7.3 through 7.5. Since the baryonic loading scales the neutrino fluence linearly, systematic errors are incorporated into the results by scaling the vertical axis of these plots.

## 7.4 GRBs and Observed Astrophysical Neutrinos

IceCube has recently observed [103, 104] the existence of an astrophysical neutrino flux whose sources, like those of the UHECRs, are not yet known. This flux is established by neutrino events above expected backgrounds in the 10 TeV to few PeV range. The observed signal is consistent with an isotropic flux and can be

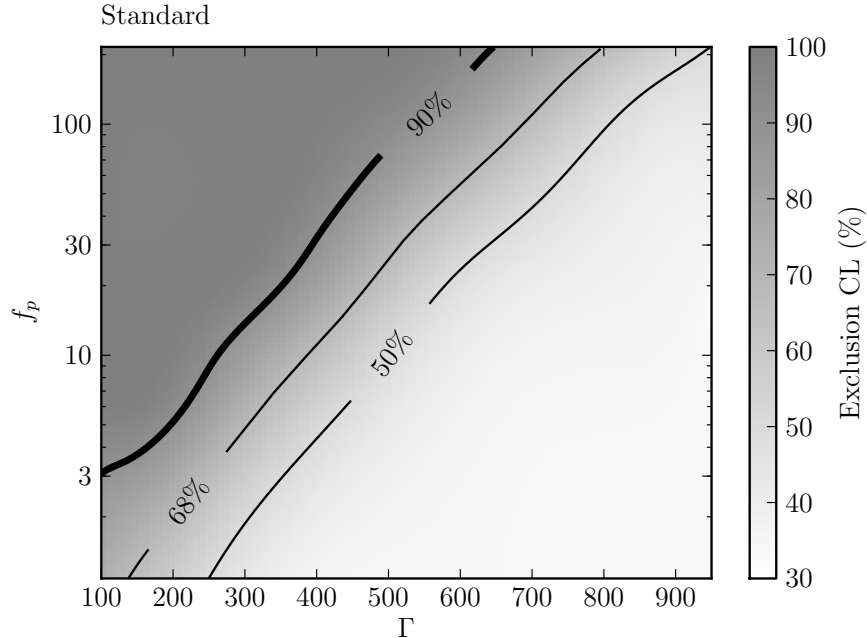


Figure 7.3: Exclusion contours for the standard fireball model.

parameterized as  $\Phi_\nu(E) = \Phi_0(E/E_0)^{-\gamma}$ . If  $E_0$  is taken to be 100 TeV, then the best fit gives a per-flavor  $\nu + \bar{\nu}$  normalization  $E_0^2 \Phi_0 = 2.06_{0.3}^{0.4} \times 10^{-8} \text{ GeV cm}^{-2} \text{ sr}^{-1} \text{ s}^{-1}$  and spectral index  $\gamma = 2.46 \pm 0.12$  [104]. To constrain the contribution to this flux from GRBs, we follow the prescription applied above to the top-down models, except this time the simulation is weighted to unbroken spectra with  $2 < \gamma < 2.6$ . Only simulated events above 10 TeV are considered; at very high energies, where the flux is already much smaller, no explicit cutoff is made. The exclusion contours are shown in Figure 7.6. It turns out that for a pivot energy  $E_0 = 100$  TeV, the constraint varies only slowly with  $\gamma$ . Regardless of the spectral index, potentially observable GRBs contribute no more than  $\sim 1\%$  of the observed astrophysical flux, at 90% CL.

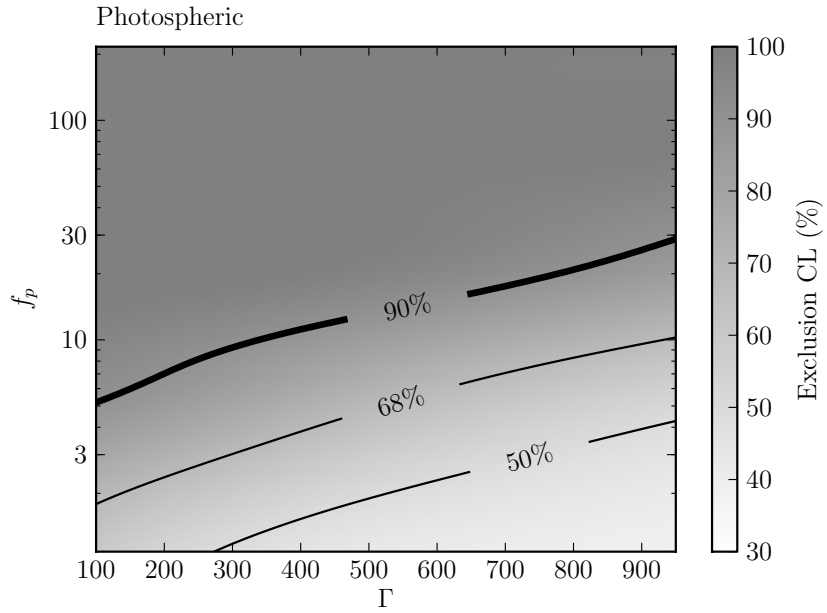


Figure 7.4: Exclusion contours for the photospheric fireball model. Because the photospheric model spectra vary more slowly with  $\Gamma$ , more of the parameter space is excluded than for the standard fireball model.

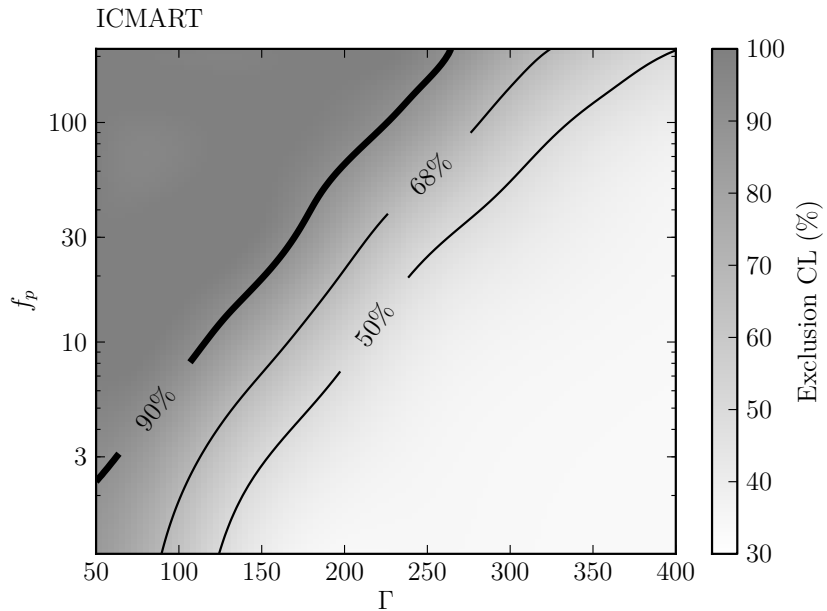


Figure 7.5: Exclusion contours for the ICMART fireball model. Because the ICMART model spectra are generally dimmer and more rapidly decreasing with  $\Gamma$ , less of the parameter space is excluded than for the standard fireball model.

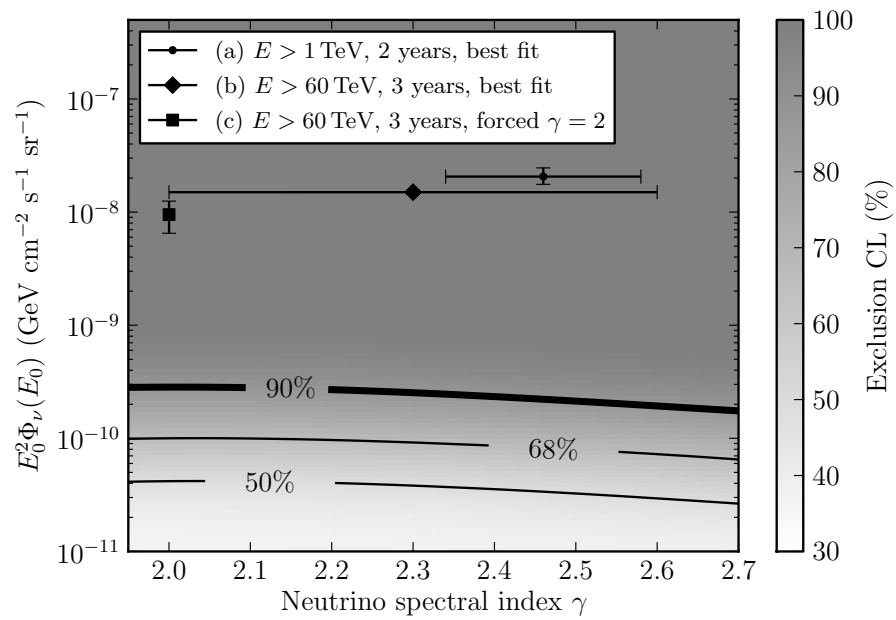


Figure 7.6: Exclusion contours showing constraints on an unbroken power law flux with a 10 TeV threshold in the context of the observed astrophysical neutrino flux. (a) is taken from [104]; (b) and (c) are from [103].

## Chapter 8: Conclusion and Outlook

The fundamental result of this experiment is that in four years of IceCube data, there is no sign of neutrino emission correlated with GRBs above the expected atmospheric backgrounds. This implies that we can set the most stringent constraints to date on neutrino production by GRBs. The interpretation of the null result is necessarily model dependent, so we have attempted to present the results in various theoretical contexts which are discussed in turn below.

For top-down models which neglect per-burst variation, we consider doubly-broken power law spectra with break energies throughout the sensitive range of IceCube. This is similar to the approach taken in previously published work [7] which neglected the higher-energy spectral break. Here, we tighten those constraints by approximately the factor by which we increase the number of bursts observed. It is clear from Figure 7.2 that we strongly exclude models that produce the entire UHECR flux using neutrons that freely escape the GRB fireball. If protons escape the fireball somehow — and for these models, the escape mechanism has not been specified precisely — our results are still in tension with GRB-dominated UHECR production, but the exclusion is not as strong. Because of the low background in this search and the generality of the models, our constraints will become more stringent almost linearly with time in the absence of a clear emerging signal.

Our constraints for bottom-up models in Figures 7.3 through 7.5 are not as straightforward to interpret. Recent work [55] suggests that we have tested the baryonic loading and bulk Lorentz factor parameter space which is relevant to GRB-dominated UHECR production in the standard fireball scenario. Some of the parameter space is strongly excluded. The allowed parameter space varies strongly moving from the neutrino-bright photospheric model to the neutrino-dim



ICMART model. These alternative cases have not yet been studied in the context of unified gamma–UHECR–neutrino analyses, so the implication of those results is not clear. Furthermore, we have not considered the impact of burst-to-burst variation of these parameters, i.e. if they are distributed somehow rather than constant across bursts. An additional complication is that the cited work used toy models of the GRB population to determine the relevant parameter space; so far, no study has used *actually observed* GRBs for this type of multi-messenger fit. For these reasons, the study of detailed models has the potential to be improved in several aspects, especially if follow-up work includes direct collaboration with theorists studying self-consistent multi-messenger models. Such work would lead to the most conclusive statements possible regarding UHECR production by GRBs.

Finally, in Figure 7.6, we show that GRBs are strongly disfavored as dominant sources of the diffuse astrophysical flux recently established [103, 104] by IceCube. This result is robust in spite the uncertainty in the spectrum. Note that a naive way to obtain a constraint would be to look for a correlation between GRBs and the specific events that confirm the astrophysical flux in an (as of yet unpublished) search for muon tracks from a diffuse astrophysical muon neutrino flux. The result here is even more sensitive to a GRB contribution because, while diffuse searches must use very tight cuts to eliminate all misreconstructed events, a GRB-specific search can take advantage of the small space-time signal window to tolerate some misreconstructed events in exchange for higher signal efficiency.

All results shown in this thesis are based on muon neutrinos interacting through the charged-current. However, regardless of the precise flavor distribution at the source, intergalactic propagation provides sufficiently long baselines to scramble the observed flavor ratio to approximately  $(e : \mu : \tau) = (1 : 1 : 1)$ . A search for cascade-topology events, which are observed for  $e$  and  $\tau$  charged-current

interactions and all neutral-current interactions, is underway. Furthermore, the latest southern sky muon neutrino search used the 59-string detector [7]; at the time of this writing a search sensitive to high energy ( $\gtrsim 100$  TeV) downgoing tracks in the completed detector is in the optimization phase. These additional detection channels are not as sensitive as the traditional northern hemisphere track search presented here, but they each provide a non-negligible improvement in sensitivity.

The GRB search has achieved unprecedented stability in several regards: the physical detector is complete; changes in data mass-processing have slowed significantly; decision tree forests have become standard tools for neutrino selection; and in recent years the unbinned likelihood method has only changed in minor ways such as the decoupling of different detector configurations and detection channels provided by (7.1) (as opposed to (6.11)). The analysis is sufficiently mature that steps are now being taken to search for neutrinos correlated with GRBs with a latency as low as days or even minutes. In the event of a very significant neutrino, this could allow IceCube to notify the community that a particular burst deserves thorough broadband follow-up. For correlations with poorly-localized bursts such as the one observed during the 79-string configuration, the GRB localization could be refined dramatically, conclusively confirming or excluding the GRB-neutrino correlation.

IceCube already provides world-leading constraints on GRBs as high energy neutrino, and hence UHECR, accelerators. With extensions of the search to the southern sky and other neutrino interaction channels, the analysis is becoming even more sensitive. Follow-up programs are being developed to obtain as much information as possible in the event that a significant GRB-neutrino correlation is observed. In the absence of a signal, it will become increasingly implausible that GRBs are important accelerators of the highest energy cosmic rays.

## Appendix A: GRB Catalogs

The prompt neutrino flux from GRBs is constrained by four years of data from IceCube. Of those, the IC79 and IC86-1 GRB catalogs are searched for the first time, while the IC40 [99] and IC59 [100] catalogs are detailed in previous dissertations. In this appendix, we provide per-GRB information taken from GRB-web [45] for use in this analysis. IC79 and IC86-1 GRBs are listed in Tables A.1 and A.2, respectively.

Each burst is named according to the date on which it occurred (formatted as YYMMDD) plus a letter indicating the order in which bursts on the same day were reported (A, B, etc.). Burst timing is expressed as a trigger time  $T_0$  in UT along with start and stop times  $T_1$  and  $T_2$  in seconds relative to  $T_0$ . The start and stop times are the most inclusive times of gamma-ray observation above background by any satellite.

The GRB position is given in equatorial coordinates:  $\alpha$  is the right ascension,  $\delta$  is the declination, and  $\sigma$  is the angular error. All angles are expressed in degrees. Errors marked by \* indicate bursts localized by Fermi-GBM; here, statistical errors are shown and additional systematic errors discussed in Section 2.2.1 apply. The redshift is given by  $z$ .

The remaining columns give fluence information.  $f_\gamma$  is the normalization of the fluence in  $\text{erg cm}^{-2}$ .  $\epsilon_\gamma$  is the peak energy in keV. The spectral indices are given by  $\alpha_\gamma$  and  $\beta_\gamma$ . Where  $z$ ,  $\epsilon_\gamma$ ,  $\alpha_\gamma$  or  $\beta_\gamma$  are unmeasured, average values are used as has been done in earlier IceCube work [6, 7, 51] except for GRBs only reported by Fermi-GBM, in which case average values are taken from their first two-year spectral catalog [46]. These values are indicated by †.

Finally, known northern GRBs that were excluded from the IC79 and IC86-1 catalogs are summarized in Figure A.3.

Table A.1: IC79 GRB Catalog

Name	Time			Position				Fluence			
	$T_0$	$T_1$	$T_2$	$\alpha$	$\delta$	$\sigma$	$z$	$f_\gamma$	$\epsilon_\gamma$	$\alpha_\gamma$	$\beta_\gamma$
100608A	09:10:07	-7.68	22.53	30.54	20.45	5.7*	2.15 <sup>†</sup>	$1.1 \times 10^{-15}$	205.0 <sup>†</sup>	1.05 <sup>†</sup>	2.25 <sup>†</sup>
100609A	18:48:12	-2.98	91.77	90.48	42.78	3.2*	2.15 <sup>†</sup>	$1.5 \times 10^{-15}$	205.0 <sup>†</sup>	1.05 <sup>†</sup>	2.25 <sup>†</sup>
100612A	13:04:22	0	0.58	63.53	13.74	3.4*	0.5 <sup>†</sup>	$3.4 \times 10^{-16}$	205.0 <sup>†</sup>	1.05 <sup>†</sup>	2.25 <sup>†</sup>
100612B	17:26:06	0.7	9.28	352	-1.83	2.6*	2.15 <sup>†</sup>	$8.5 \times 10^{-15}$	205.0 <sup>†</sup>	1.05 <sup>†</sup>	2.25 <sup>†</sup>
100614A	21:38:26	-9	282	263.499	49.234	0.0005	2.15 <sup>†</sup>	$2.2 \times 10^{-15}$	200.0 <sup>†</sup>	1.88	2.88
100614B	11:57:24	-149.76	22.53	224.76	40.87	3.6*	2.15 <sup>†</sup>	$1.2 \times 10^{-14}$	205.0 <sup>†</sup>	1.05 <sup>†</sup>	2.25 <sup>†</sup>
100616A	18:32:32	-0.19	10	342.91	3.09	45.8*	0.5 <sup>†</sup>	$4.3 \times 10^{-17}$	205.0 <sup>†</sup>	1.05 <sup>†</sup>	2.25 <sup>†</sup>
100621B	10:51:19	-6.66	117.25	103.83	37.35	3.5*	2.15 <sup>†</sup>	$4.8 \times 10^{-15}$	205.0 <sup>†</sup>	1.05 <sup>†</sup>	2.25 <sup>†</sup>
100621C	12:42:16	-0.45	0.58	160.86	14.72	11.6*	0.5 <sup>†</sup>	$2.1 \times 10^{-17}$	205.0 <sup>†</sup>	1.05 <sup>†</sup>	2.25 <sup>†</sup>
100625B	21:22:45	-7.42	21.76	338.26	20.29	4.9*	2.15 <sup>†</sup>	$8.8 \times 10^{-16}$	205.0 <sup>†</sup>	1.05 <sup>†</sup>	2.25 <sup>†</sup>
100629A	19:14:04	-0.13	0.7	231.21	27.81	3.9*	0.5 <sup>†</sup>	$1.8 \times 10^{-16}$	205.0 <sup>†</sup>	1.05 <sup>†</sup>	2.25 <sup>†</sup>
100701B	11:45:19	0	26.11	43.109	-2.224	0.277	2.15 <sup>†</sup>	$3.0 \times 10^{-13}$	1480.0	0.95	2.47
100706A	16:38:19	-0.13	10	255.16	46.89	12.4*	0.5 <sup>†</sup>	$2.0 \times 10^{-17}$	205.0 <sup>†</sup>	1.05 <sup>†</sup>	2.25 <sup>†</sup>
100709A	14:27:33	-2.56	97.54	142.53	17.38	4.9*	2.15 <sup>†</sup>	$5.1 \times 10^{-15}$	205.0 <sup>†</sup>	1.05 <sup>†</sup>	2.25 <sup>†</sup>
100713A	14:36:06	0	20	255.209	28.39	0.0417	2.15 <sup>†</sup>	$1.2 \times 10^{-15}$	200.0 <sup>†</sup>	1.0 <sup>†</sup>	2.0 <sup>†</sup>
100713B	23:31:34	-0.38	7.23	82.06	13	4.3*	2.15 <sup>†</sup>	$1.9 \times 10^{-15}$	205.0 <sup>†</sup>	1.05 <sup>†</sup>	2.25 <sup>†</sup>
100714A	16:07:24	-0.51	35.07	106.37	51.14	4.2*	2.15 <sup>†</sup>	$2.0 \times 10^{-15}$	205.0 <sup>†</sup>	1.05 <sup>†</sup>	2.25 <sup>†</sup>
100714B	16:27:20	-2.88	5.56	307.94	61.3	9.9*	2.15 <sup>†</sup>	$1.5 \times 10^{-15}$	205.0 <sup>†</sup>	1.05 <sup>†</sup>	2.25 <sup>†</sup>
100717A	08:55:06	-0.58	5.38	287.06	-0.66	9.1*	2.15 <sup>†</sup>	$2.7 \times 10^{-16}$	205.0 <sup>†</sup>	1.05 <sup>†</sup>	2.25 <sup>†</sup>
100717B	10:41:47	-0.13	2.3	304.31	19.53	9.4*	2.15 <sup>†</sup>	$2.1 \times 10^{-16}$	205.0 <sup>†</sup>	1.05 <sup>†</sup>	2.25 <sup>†</sup>
100718B	03:50:10	-21.62	11.02	121.83	-46.18	6.3*	2.15 <sup>†</sup>	$1.7 \times 10^{-15}$	205.0 <sup>†</sup>	1.05 <sup>†</sup>	2.25 <sup>†</sup>
100719C	19:48:09	-2.3	0.77	231.41	18.56	10.5*	2.15 <sup>†</sup>	$1.7 \times 10^{-16}$	205.0 <sup>†</sup>	1.05 <sup>†</sup>	2.25 <sup>†</sup>

Table A.1: IC79 GRB Catalog (continued)

Name	Time			Position				Fluence				
	$T_0$	$T_1$	$T_2$	$\alpha$	$\delta$	$\sigma$	$z$	$f_\gamma$	$\epsilon_\gamma$	$\alpha_\gamma$	$\beta_\gamma$	
100719D	23:44:04	1.54	23.36	113.3	5.4	2.3*	2.15 <sup>†</sup>	$3.2 \times 10^{-14}$	205.0 <sup>†</sup>	1.05 <sup>†</sup>	2.25 <sup>†</sup>	
100722B	06:58:25	-1.22	0.06	31.81	56.23	8.3*	0.5 <sup>†</sup>	$1.6 \times 10^{-17}$	205.0 <sup>†</sup>	1.05 <sup>†</sup>	2.25 <sup>†</sup>	
100724B	00:42:04	-4.1	230.608	120.04	76.74	1.1	2.15 <sup>†</sup>	$2.4 \times 10^{-12}$	467.8	0.84	1.84	
100725B	11:24:34	-4.8	226.1	290.033	76.956	0.0005	2.15 <sup>†</sup>	$5.4 \times 10^{-15}$	200.0 <sup>†</sup>	1.89	2.89	
100728B	10:31:55	-2.05	13.2	163.488	-45.473	0.0001	2.15 <sup>†</sup>	$5.4 \times 10^{-16}$	104.0	0.8	2.2	
100802A	05:45:36	-3.3	531.7	2.468	47.755	0.0006	2.15 <sup>†</sup>	$1.9 \times 10^{-15}$	149.0	1.17	3.17	
100804A	02:29:26	0.13	6.72	248.97	27.45	2.3*	2.15 <sup>†</sup>	$6.7 \times 10^{-15}$	205.0 <sup>†</sup>	1.05 <sup>†</sup>	2.25 <sup>†</sup>	
100805A	04:12:42	-1.4	17.1	299.877	52.628	0.0001	2.15 <sup>†</sup>	$5.3 \times 10^{-16}$	200.0 <sup>†</sup>	1.76	2.76	
100805B	07:12:12	-0.1	-0.03	22.8	34.19	7.9*	0.5 <sup>†</sup>	$3.1 \times 10^{-17}$	205.0 <sup>†</sup>	1.05 <sup>†</sup>	2.25 <sup>†</sup>	
100807A	09:13:13	-6.1	3.1	55.3	67.672	0.0005	2.15 <sup>†</sup>	$1.4 \times 10^{-16}$	200.0 <sup>†</sup>	2.32	3.32	
100810A	01:10:34	-1.86	0.7	124.77	-1.61	6.0*	2.15 <sup>†</sup>	$2.5 \times 10^{-16}$	205.0 <sup>†</sup>	1.05 <sup>†</sup>	2.25 <sup>†</sup>	
100811A	02:35:49	-0.06	0.32	345.87	15.86	6.4*	0.5 <sup>†</sup>	$4.5 \times 10^{-16}$	205.0 <sup>†</sup>	1.05 <sup>†</sup>	2.25 <sup>†</sup>	
100811B	18:44:10	-52.99	25.09	108.14	62.19	4.1*	2.15 <sup>†</sup>	$2.9 \times 10^{-15}$	205.0 <sup>†</sup>	1.05 <sup>†</sup>	2.25 <sup>†</sup>	
100814B	08:25:26	-0.77	6.66	122.82	18.49	3.3*	2.15 <sup>†</sup>	$9.1 \times 10^{-16}$	81.0	0.62	2.49	
100816A	00:37:51	-0.7	10.448	351.74	26.579	0.0004	0.8049	$2.8 \times 10^{-16}$	136.7	0.31	2.77	
100823A	17:25:33	0	25	20.704	5.835	0.0006	2.15 <sup>†</sup>	$2.0 \times 10^{-16}$	200.0 <sup>†</sup>	2.19	3.19	
100827A	10:55:49	-0.13	0.45	193.9	71.89	6.0*	0.5 <sup>†</sup>	$1.6 \times 10^{-16}$	205.0 <sup>†</sup>	1.05 <sup>†</sup>	2.25 <sup>†</sup>	
100829A	21:02:07	0	10.8	90.409	30.314	0.808	2.15 <sup>†</sup>	$4.4 \times 10^{-14}$	278.0	1.44	9.4	
100829B	08:59:07	0.26	95.23	115.45	-3.99	5.1*	2.15 <sup>†</sup>	$4.6 \times 10^{-15}$	205.0 <sup>†</sup>	1.05 <sup>†</sup>	2.25 <sup>†</sup>	
100831A	15:37:26	-23.3	16.9	161.26	33.65	10.4*	2.15 <sup>†</sup>	$1.8 \times 10^{-15}$	205.0 <sup>†</sup>	1.05 <sup>†</sup>	2.25 <sup>†</sup>	
100901A	13:34:10	-2.4	471.8	27.265	22.759	0.0006	1.408	$1.5 \times 10^{-15}$	200.0 <sup>†</sup>	1.52	2.52	
100902A	19:31:54	-49.5	409.6	48.629	30.979	0.0004	2.15 <sup>†</sup>	$2.2 \times 10^{-15}$	200.0 <sup>†</sup>	1.98	2.98	

Table A.1: IC79 GRB Catalog (continued)

Name	Time			Position					Fluence				
	$T_0$	$T_1$	$T_2$	$\alpha$	$\delta$	$\sigma$	$z$	$f_\gamma$	$\epsilon_\gamma$	$\alpha_\gamma$	$\beta_\gamma$		
100902B	23:45:20	-4.1	18.18	306.04	42.31	7.5*	2.15 <sup>†</sup>	$1.3 \times 10^{-15}$	205.0 <sup>†</sup>	1.05 <sup>†</sup>	2.25 <sup>†</sup>		
100905A	15:08:14	-1.6	2.1	31.55	14.929	0.0004	2.15 <sup>†</sup>	$1.1 \times 10^{-15}$	200.0 <sup>†</sup>	1.09	2.09		
100905B	21:46:23	-4.61	6.91	262.65	13.08	4.5*	2.15 <sup>†</sup>	$1.2 \times 10^{-15}$	205.0 <sup>†</sup>	1.05 <sup>†</sup>	2.25 <sup>†</sup>		
100906A	13:49:27	-0.2	142.264	28.684	55.631	0.0004	1.727	$2.7 \times 10^{-15}$	106.0	1.34	1.98		
100909A	09:04:00	0	60	73.951	54.654	0.0333	2.15 <sup>†</sup>	$6.2 \times 10^{-14}$	200.0 <sup>†</sup>	1.0 <sup>†</sup>	2.0 <sup>†</sup>		
100911A	19:35:40	-0.77	4.86	151.32	58.99	11.9*	2.15 <sup>†</sup>	$5.4 \times 10^{-16}$	205.0 <sup>†</sup>	1.05 <sup>†</sup>	2.25 <sup>†</sup>		
100915A	01:31:05	-36.3	72.2	315.694	65.673	0.0004	2.15 <sup>†</sup>	$3.1 \times 10^{-15}$	265.2	1.5	3.5		
100915B	05:49:40	-7.42	3	85.394	25.095	2.0*	2.15 <sup>†</sup>	$1.9 \times 10^{-16}$	83.49	1.35	3.35		
100919A	21:12:17	-38.4	11.2	163.24	6.02	2.7*	2.15 <sup>†</sup>	$3.6 \times 10^{-15}$	205.0 <sup>†</sup>	1.05 <sup>†</sup>	2.25 <sup>†</sup>		
100923A	20:15:10	-0.77	50.94	106.12	39.6	5.7*	2.15 <sup>†</sup>	$2.5 \times 10^{-15}$	205.0 <sup>†</sup>	1.05 <sup>†</sup>	2.25 <sup>†</sup>		
100924A	03:58:08	-15.1	128.9	0.672	7.004	0.0167	2.15 <sup>†</sup>	$2.4 \times 10^{-15}$	200.0 <sup>†</sup>	1.59	2.59		
100929A	05:38:53	-2.3	5.89	166.33	62.29	13.5*	2.15 <sup>†</sup>	$3.1 \times 10^{-16}$	205.0 <sup>†</sup>	1.05 <sup>†</sup>	2.25 <sup>†</sup>		
100929B	07:33:04	-0.51	4.1	243.62	33.33	23.9*	2.15 <sup>†</sup>	$2.0 \times 10^{-16}$	205.0 <sup>†</sup>	1.05 <sup>†</sup>	2.25 <sup>†</sup>		
101003A	05:51:08	-1.79	8.19	175.85	2.49	7.7*	2.15 <sup>†</sup>	$1.4 \times 10^{-15}$	205.0 <sup>†</sup>	1.05 <sup>†</sup>	2.25 <sup>†</sup>		
101008A	16:43:15	-4	106.6	328.875	37.067	0.0006	2.15 <sup>†</sup>	$2.0 \times 10^{-15}$	200.0 <sup>†</sup>	1.42	2.42		
101010A	04:33:47	-11.01	54.02	47.19	43.56	18.7*	2.15 <sup>†</sup>	$9.7 \times 10^{-16}$	205.0 <sup>†</sup>	1.05 <sup>†</sup>	2.25 <sup>†</sup>		
101015A	13:24:03	-2.05	498.5	73.16	15.46	6.3*	2.15 <sup>†</sup>	$2.3 \times 10^{-14}$	205.0 <sup>†</sup>	1.05 <sup>†</sup>	2.25 <sup>†</sup>		
101016A	05:50:16	-1.54	2.3	133.04	-4.62	3.5*	2.15 <sup>†</sup>	$1.5 \times 10^{-15}$	205.0 <sup>†</sup>	1.05 <sup>†</sup>	2.25 <sup>†</sup>		
101020A	23:40:41	-50	159	189.607	23.129	0.0567	2.15 <sup>†</sup>	$1.6 \times 10^{-15}$	200.0 <sup>†</sup>	2.04	3.04		
101021B	01:30:32	-0.51	1.02	0.46	47.34	13.0*	0.5 <sup>†</sup>	$4.5 \times 10^{-17}$	205.0 <sup>†</sup>	1.05 <sup>†</sup>	2.25 <sup>†</sup>		
101026A	00:49:16	-0.13	0.13	263.7	-0.37	7.8*	0.5 <sup>†</sup>	$1.4 \times 10^{-16}$	205.0 <sup>†</sup>	1.05 <sup>†</sup>	2.25 <sup>†</sup>		
101027A	05:30:30	-1.28	0.06	79.02	43.97	11.6*	0.5 <sup>†</sup>	$2.2 \times 10^{-17}$	205.0 <sup>†</sup>	1.05 <sup>†</sup>	2.25 <sup>†</sup>		

Table A.1: IC79 GRB Catalog (continued)

Name	Time			Position				Fluence			
	$T_0$	$T_1$	$T_2$	$\alpha$	$\delta$	$\sigma$	$z$	$f_\gamma$	$\epsilon_\gamma$	$\alpha_\gamma$	$\beta_\gamma$
101101A	17:51:34	-2.3	1.02	13.55	45.75	3.7*	2.15 <sup>†</sup>	$4.1 \times 10^{-16}$	205.0 <sup>†</sup>	1.05 <sup>†</sup>	2.25 <sup>†</sup>
101107A	00:16:26	2.3	378.12	168.33	22.43	4.6*	2.15 <sup>†</sup>	$4.5 \times 10^{-15}$	205.0 <sup>†</sup>	1.05 <sup>†</sup>	2.25 <sup>†</sup>
101112A	22:10:24	0	15.448	292.218	39.359	2.0*	2.15 <sup>†</sup>	$5.9 \times 10^{-16}$	105.8	0.79	2.02
101112B	23:36:56	-9.47	73.47	100.1	9.62	5.5*	2.15 <sup>†</sup>	$5.4 \times 10^{-15}$	205.0 <sup>†</sup>	1.05 <sup>†</sup>	2.25 <sup>†</sup>
101113A	11:35:36	-0.26	12.03	29.08	0.21	3.4*	2.15 <sup>†</sup>	$1.9 \times 10^{-15}$	205.0 <sup>†</sup>	1.05 <sup>†</sup>	2.25 <sup>†</sup>
101114A	00:32:50	-2.2	6.6	303.193	14.029	0.03	2.15 <sup>†</sup>	$8.0 \times 10^{-15}$	296.0	1.15	3.15
101119A	16:27:03	-0.32	0.32	226.49	59.61	16.3*	0.5 <sup>†</sup>	$2.6 \times 10^{-17}$	205.0 <sup>†</sup>	1.05 <sup>†</sup>	2.25 <sup>†</sup>
101123A	22:51:35	41.47	161.272	131.381	5.563	1.022	2.15 <sup>†</sup>	$3.2 \times 10^{-13}$	476.0	0.75	2.14
101127A	02:13:59	-3.33	26.11	290.31	7.89	23.3*	2.15 <sup>†</sup>	$4.4 \times 10^{-16}$	205.0 <sup>†</sup>	1.05 <sup>†</sup>	2.25 <sup>†</sup>
101129B	17:25:25	-0.06	0.51	271.54	1.01	8.5*	0.5 <sup>†</sup>	$1.2 \times 10^{-16}$	205.0 <sup>†</sup>	1.05 <sup>†</sup>	2.25 <sup>†</sup>
101130B	01:45:55	-2.3	2.56	274.61	26.62	23.7*	2.15 <sup>†</sup>	$1.5 \times 10^{-16}$	205.0 <sup>†</sup>	1.05 <sup>†</sup>	2.25 <sup>†</sup>
101202A	03:41:54	0	18.43	254.02	58.48	6.5*	2.15 <sup>†</sup>	$8.8 \times 10^{-16}$	205.0 <sup>†</sup>	1.05 <sup>†</sup>	2.25 <sup>†</sup>
101204B	08:14:19	-0.06	0.06	191.91	55.67	10.6*	0.5 <sup>†</sup>	$4.3 \times 10^{-17}$	205.0 <sup>†</sup>	1.05 <sup>†</sup>	2.25 <sup>†</sup>
101207A	12:51:42	5.63	67.07	175.75	8.72	4.3*	2.15 <sup>†</sup>	$4.2 \times 10^{-15}$	205.0 <sup>†</sup>	1.05 <sup>†</sup>	2.25 <sup>†</sup>
101208A	04:52:57	-0.19	10	212.4	4.04	11.9*	0.5 <sup>†</sup>	$4.8 \times 10^{-17}$	205.0 <sup>†</sup>	1.05 <sup>†</sup>	2.25 <sup>†</sup>
101211A	11:37:55	-2.82	10.75	31.84	10.06	11.4*	2.15 <sup>†</sup>	$1.0 \times 10^{-15}$	205.0 <sup>†</sup>	1.05 <sup>†</sup>	2.25 <sup>†</sup>
101213A	10:49:19	-1	201.1	241.314	21.897	0.0005	0.414	$9.1 \times 10^{-16}$	309.7	1.1	2.35
101219A	02:31:29	0	5.6	74.586	-2.527	0.0167	2.15 <sup>†</sup>	$2.5 \times 10^{-14}$	490.0	0.22	2.22
101220A	13:49:59	2.3	74.75	241.57	46.14	2.4*	2.15 <sup>†</sup>	$6.0 \times 10^{-15}$	205.0 <sup>†</sup>	1.05 <sup>†</sup>	2.25 <sup>†</sup>
101220B	20:43:54	-1.02	30.72	2.7	27.2	2.5*	2.15 <sup>†</sup>	$3.3 \times 10^{-15}$	205.0 <sup>†</sup>	1.05 <sup>†</sup>	2.25 <sup>†</sup>
101223A	20:00:19	-41.22	14.85	250.55	48.22	4.8*	2.15 <sup>†</sup>	$1.5 \times 10^{-15}$	205.0 <sup>†</sup>	1.05 <sup>†</sup>	2.25 <sup>†</sup>
101224A	05:27:13	0	2.66	285.939	45.706	0.035	2.15 <sup>†</sup>	$8.6 \times 10^{-16}$	330.0	0.83	2.83

Table A.1: IC79 GRB Catalog (continued)

Name	Time			Position				Fluence			
	$T_0$	$T_1$	$T_2$	$\alpha$	$\delta$	$\sigma$	$z$	$f_\gamma$	$\epsilon_\gamma$	$\alpha_\gamma$	$\beta_\gamma$
101224C	14:43:33	-2.56	23.04	290.16	34.46	9.1*	2.15 <sup>†</sup>	$1.6 \times 10^{-15}$	205.0 <sup>†</sup>	1.05 <sup>†</sup>	2.25 <sup>†</sup>
101225A	18:37:45	0	963	0.198	44.6	0.0004	2.15 <sup>†</sup>	$2.8 \times 10^{-15}$	200.0 <sup>†</sup>	1.82	2.82
101225B	09:02:54	20.54	101.76	60.68	32.77	2.7*	2.15 <sup>†</sup>	$1.3 \times 10^{-14}$	205.0 <sup>†</sup>	1.05 <sup>†</sup>	2.25 <sup>†</sup>
101231A	01:36:51	0	23.62	191.71	17.64	2.5*	2.15 <sup>†</sup>	$1.1 \times 10^{-14}$	205.0 <sup>†</sup>	1.05 <sup>†</sup>	2.25 <sup>†</sup>
110101A	04:50:20	-2.3	1.28	264.26	36.54	11.4*	2.15 <sup>†</sup>	$1.6 \times 10^{-16}$	205.0 <sup>†</sup>	1.05 <sup>†</sup>	2.25 <sup>†</sup>
110101B	12:08:22	-103.43	132.1	105.5	34.58	16.6*	2.15 <sup>†</sup>	$4.1 \times 10^{-15}$	205.0 <sup>†</sup>	1.05 <sup>†</sup>	2.25 <sup>†</sup>
110102A	18:52:25	-49.2	294.9	245.881	7.614	0.0001	2.15 <sup>†</sup>	$3.8 \times 10^{-14}$	267.0	1.22	2.3
110106A	15:25:16	-1	3.9	79.306	64.173	0.0005	2.15 <sup>†</sup>	$3.5 \times 10^{-16}$	200.0 <sup>†</sup>	1.71	2.71
110106B	21:26:16	-16.9	24.5	134.154	47.003	0.0005	0.618	$4.7 \times 10^{-16}$	200.0 <sup>†</sup>	1.61	2.61
110107A	21:15:51	-70	122.37	299.89	41.889	0.05	2.15 <sup>†</sup>	$9.1 \times 10^{-15}$	200.0 <sup>†</sup>	1.58	2.58
110112A	04:12:18	-0.1	0.5	329.932	26.456	0.0009	0.5 <sup>†</sup>	$9.6 \times 10^{-18}$	1000.0 <sup>†</sup>	2.14	3.14
110112B	22:24:54	0	2.34	10.6	64.41	2.0*	2.15 <sup>†</sup>	$1.2 \times 10^{-15}$	495.0	0.72	2.72
110117A	08:44:51	-1.79	70.66	130.87	47.59	9.8*	2.15 <sup>†</sup>	$1.6 \times 10^{-15}$	205.0 <sup>†</sup>	1.05 <sup>†</sup>	2.25 <sup>†</sup>
110119A	22:20:58	-86.4	217.5	348.586	5.986	0.0005	2.15 <sup>†</sup>	$3.7 \times 10^{-15}$	126.3	0.6	1.95
110123A	19:17:45	0.7	18.56	246.97	28.03	2.3*	2.15 <sup>†</sup>	$2.8 \times 10^{-14}$	280.0	0.64	1.96
110124A	18:49:09	-3.33	2.05	53.83	36.35	9.4*	2.15 <sup>†</sup>	$9.9 \times 10^{-17}$	205.0 <sup>†</sup>	1.05 <sup>†</sup>	2.25 <sup>†</sup>
110130A	05:31:53	-0.26	47.1	111.51	38.25	7.1*	2.15 <sup>†</sup>	$1.8 \times 10^{-15}$	205.0 <sup>†</sup>	1.05 <sup>†</sup>	2.25 <sup>†</sup>
110201A	09:35:08	-2.8	13.3	137.489	88.61	0.0217	2.15 <sup>†</sup>	$4.4 \times 10^{-15}$	200.0 <sup>†</sup>	1.09	2.09
110205A	02:02:41	0	330	164.63	67.525	0.0004	2.22	$3.5 \times 10^{-14}$	222.0	1.52	3.52
110206B	04:50:36	-6.4	5.89	333.7	1.61	15.6*	2.15 <sup>†</sup>	$4.9 \times 10^{-16}$	205.0 <sup>†</sup>	1.05 <sup>†</sup>	2.25 <sup>†</sup>
110210A	09:52:41	-102.9	153.6	13.057	7.78	0.0005	2.15 <sup>†</sup>	$1.1 \times 10^{-15}$	200.0 <sup>†</sup>	1.73	2.73
110212A	01:09:08	-1.8	2.6	69.025	43.716	0.0233	2.15 <sup>†</sup>	$7.0 \times 10^{-17}$	44.6	0.78	2.78



Table A.1: IC79 GRB Catalog (continued)

Name	Time			Position					Fluence				
	$T_0$	$T_1$	$T_2$	$\alpha$	$\delta$	$\sigma$	$z$	$f_\gamma$	$\epsilon_\gamma$	$\alpha_\gamma$	$\beta_\gamma$		
110213A	05:17:29	-31.2	32.8	42.964	49.273	0.0004	2.15 <sup>†</sup>	$2.3 \times 10^{-15}$	89.0	1.28	2.4		
110213B	14:31:33	0	50	41.768	0.952	0.0087	1.083	$2.6 \times 10^{-15}$	123.0	1.52	3.52		
110213C	21:00:52	-0.13	0.19	6.28	27.54	11.0*	0.5 <sup>†</sup>	$5.0 \times 10^{-18}$	205.0 <sup>†</sup>	1.05 <sup>†</sup>	2.25 <sup>†</sup>		
110220A	18:16:22	-1.79	31.23	185.49	16.58	6.4*	2.15 <sup>†</sup>	$1.3 \times 10^{-15}$	205.0 <sup>†</sup>	1.05 <sup>†</sup>	2.25 <sup>†</sup>		
110221A	05:51:20	-1.54	11.52	15.18	66.05	2.4*	2.15 <sup>†</sup>	$1.4 \times 10^{-15}$	205.0 <sup>†</sup>	1.05 <sup>†</sup>	2.25 <sup>†</sup>		
110223A	20:56:59	0.1	8.1	345.854	87.558	0.0006	2.15 <sup>†</sup>	$1.3 \times 10^{-15}$	200.0 <sup>†</sup>	1.0 <sup>†</sup>	2.0 <sup>†</sup>		
110226A	23:44:31	-2.3	11.78	199.29	35.77	7.4*	2.15 <sup>†</sup>	$1.2 \times 10^{-15}$	205.0 <sup>†</sup>	1.05 <sup>†</sup>	2.25 <sup>†</sup>		
110227B	05:30:11	-1.02	17.41	25.24	15.89	7.7*	2.15 <sup>†</sup>	$1.5 \times 10^{-15}$	205.0 <sup>†</sup>	1.05 <sup>†</sup>	2.25 <sup>†</sup>		
110228B	18:59:51	-3.84	13.31	245.09	16.41	5.2*	2.15 <sup>†</sup>	$6.0 \times 10^{-16}$	205.0 <sup>†</sup>	1.05 <sup>†</sup>	2.25 <sup>†</sup>		
110301A	05:08:43	0	5.7	229.35	29.4	2.3*	2.15 <sup>†</sup>	$1.3 \times 10^{-14}$	106.8	0.81	2.7		
110302A	01:01:52	-11.2	27.14	122.35	2.91	7.1*	2.15 <sup>†</sup>	$2.3 \times 10^{-15}$	205.0 <sup>†</sup>	1.05 <sup>†</sup>	2.25 <sup>†</sup>		
110304A	01:42:34	-0.26	19.26	322.93	33.27	4.7*	2.15 <sup>†</sup>	$2.2 \times 10^{-15}$	205.0 <sup>†</sup>	1.05 <sup>†</sup>	2.25 <sup>†</sup>		
110307A	23:19:08	-1.79	0.51	193.12	15.64	7.8*	2.15 <sup>†</sup>	$3.6 \times 10^{-16}$	205.0 <sup>†</sup>	1.05 <sup>†</sup>	2.25 <sup>†</sup>		
110311A	19:29:22	-1.79	4.61	117.59	34.29	9.9*	2.15 <sup>†</sup>	$7.0 \times 10^{-16}$	205.0 <sup>†</sup>	1.05 <sup>†</sup>	2.25 <sup>†</sup>		
110315A	23:57:04	-66.8	38.8	279.195	17.539	0.0004	2.15 <sup>†</sup>	$4.2 \times 10^{-15}$	200.0 <sup>†</sup>	1.77	2.77		
110328A	12:57:45	0	10	251.208	57.583	0.0005	2.15 <sup>†</sup>	$2.5 \times 10^{-14}$	200.0 <sup>†</sup>	1.0 <sup>†</sup>	2.0 <sup>†</sup>		
110328B	12:29:20	1.02	142.34	117.65	43.1	2.7*	2.15 <sup>†</sup>	$2.9 \times 10^{-14}$	369.0	1.11	1.94		
110331A	14:29:07	-0.06	3.14	6.66	25.99	5.1*	2.15 <sup>†</sup>	$1.6 \times 10^{-16}$	205.0 <sup>†</sup>	1.05 <sup>†</sup>	2.25 <sup>†</sup>		
110401A	22:04:20	-0.64	1.73	268.56	26.87	4.3*	2.15 <sup>†</sup>	$1.7 \times 10^{-14}$	1194.0	0.66	2.36		
110402A	00:12:58	-1.5	83.5	197.402	61.253	0.0006	2.15 <sup>†</sup>	$1.3 \times 10^{-13}$	1395.0	1.03	3.03		
110406A	03:44:06	0	9.216	17.34	35.809	0.0089	2.15 <sup>†</sup>	$3.9 \times 10^{-14}$	326.0	1.24	2.3		
110407A	14:06:41	-2.9	158.8	186.031	15.712	0.0006	2.15 <sup>†</sup>	$7.9 \times 10^{-16}$	57.9	0.73	2.73		

Table A.1: IC79 GRB Catalog (continued)

Name	Time			Position					Fluence			
	$T_0$	$T_1$	$T_2$	$\alpha$	$\delta$	$\sigma$	$z$	$f_\gamma$	$\epsilon_\gamma$	$\alpha_\gamma$	$\beta_\gamma$	
110411A	19:34:11	-11.9	86.3	291.442	67.712	0.0005	2.15 <sup>†</sup>	$1.1 \times 10^{-15}$	41.0	1.51	3.51	
110412A	07:33:21	13.7	40.4	133.491	13.488	0.0317	2.15 <sup>†</sup>	$1.4 \times 10^{-15}$	87.0	0.7	2.7	
110414A	07:42:14	-38.4	135.6	97.873	24.362	0.0004	2.15 <sup>†</sup>	$2.9 \times 10^{-14}$	200.0 <sup>†</sup>	1.0 <sup>†</sup>	2.0 <sup>†</sup>	
110421A	18:10:40	-2.56	37.89	277.23	50.8	2.7*	2.15 <sup>†</sup>	$6.6 \times 10^{-15}$	205.0 <sup>†</sup>	1.05 <sup>†</sup>	2.25 <sup>†</sup>	
110422B	00:41:49	-0.13	0.19	226.69	43.02	21.6*	0.5 <sup>†</sup>	$1.2 \times 10^{-17}$	205.0 <sup>†</sup>	1.05 <sup>†</sup>	2.25 <sup>†</sup>	
110428B	08:07:05	-53.76	47.87	128.44	19.94	3.6*	2.15 <sup>†</sup>	$9.9 \times 10^{-15}$	205.0 <sup>†</sup>	1.05 <sup>†</sup>	2.25 <sup>†</sup>	
110430A	09:00:14	1.02	33.54	147.06	67.95	3.2*	2.15 <sup>†</sup>	$4.4 \times 10^{-15}$	205.0 <sup>†</sup>	1.05 <sup>†</sup>	2.25 <sup>†</sup>	
110503A	17:35:45	-6.6	16.3	132.776	52.208	0.0001	1.61	$1.2 \times 10^{-14}$	219.0	0.98	2.7	

Table A.2: IC86-1 GRB Catalog

Name	Time			Position				Fluence			
	$T_0$	$T_1$	$T_2$	$\alpha$	$\delta$	$\sigma$	$z$	$f_\gamma$	$\epsilon_\gamma$	$\alpha_\gamma$	$\beta_\gamma$
100608A	09:10:07	-7.68	22.53	30.54	20.45	5.7*	2.15 <sup>†</sup>	$1.1 \times 10^{-15}$	205.0 <sup>†</sup>	1.05 <sup>†</sup>	2.25 <sup>†</sup>
100609A	18:48:12	-2.98	91.77	90.48	42.78	3.2*	2.15 <sup>†</sup>	$1.5 \times 10^{-15}$	205.0 <sup>†</sup>	1.05 <sup>†</sup>	2.25 <sup>†</sup>
100612A	13:04:22	0	0.58	63.53	13.74	3.4*	0.5 <sup>†</sup>	$3.4 \times 10^{-16}$	205.0 <sup>†</sup>	1.05 <sup>†</sup>	2.25 <sup>†</sup>
100612B	17:26:06	0.7	9.28	352	-1.83	2.6*	2.15 <sup>†</sup>	$8.5 \times 10^{-15}$	205.0 <sup>†</sup>	1.05 <sup>†</sup>	2.25 <sup>†</sup>
100614A	21:38:26	-9	282	263.499	49.234	0.0005	2.15 <sup>†</sup>	$2.2 \times 10^{-15}$	200.0 <sup>†</sup>	1.88	2.88
100614B	11:57:24	-149.76	22.53	224.76	40.87	3.6*	2.15 <sup>†</sup>	$1.2 \times 10^{-14}$	205.0 <sup>†</sup>	1.05 <sup>†</sup>	2.25 <sup>†</sup>
100616A	18:32:32	-0.19	10	342.91	3.09	45.8*	0.5 <sup>†</sup>	$4.3 \times 10^{-17}$	205.0 <sup>†</sup>	1.05 <sup>†</sup>	2.25 <sup>†</sup>
100621B	10:51:19	-6.66	117.25	103.83	37.35	3.5*	2.15 <sup>†</sup>	$4.8 \times 10^{-15}$	205.0 <sup>†</sup>	1.05 <sup>†</sup>	2.25 <sup>†</sup>
100621C	12:42:16	-0.45	0.58	160.86	14.72	11.6*	0.5 <sup>†</sup>	$2.1 \times 10^{-17}$	205.0 <sup>†</sup>	1.05 <sup>†</sup>	2.25 <sup>†</sup>
100625B	21:22:45	-7.42	21.76	338.26	20.29	4.9*	2.15 <sup>†</sup>	$8.8 \times 10^{-16}$	205.0 <sup>†</sup>	1.05 <sup>†</sup>	2.25 <sup>†</sup>
100629A	19:14:04	-0.13	0.7	231.21	27.81	3.9*	0.5 <sup>†</sup>	$1.8 \times 10^{-16}$	205.0 <sup>†</sup>	1.05 <sup>†</sup>	2.25 <sup>†</sup>
100701B	11:45:19	0	26.11	43.109	-2.224	0.277	2.15 <sup>†</sup>	$3.0 \times 10^{-13}$	1480.0	0.95	2.47
100706A	16:38:19	-0.13	10	255.16	46.89	12.4*	0.5 <sup>†</sup>	$2.0 \times 10^{-17}$	205.0 <sup>†</sup>	1.05 <sup>†</sup>	2.25 <sup>†</sup>
100709A	14:27:33	-2.56	97.54	142.53	17.38	4.9*	2.15 <sup>†</sup>	$5.1 \times 10^{-15}$	205.0 <sup>†</sup>	1.05 <sup>†</sup>	2.25 <sup>†</sup>
100713A	14:36:06	0	20	255.209	28.39	0.0417	2.15 <sup>†</sup>	$1.2 \times 10^{-15}$	200.0 <sup>†</sup>	1.0 <sup>†</sup>	2.0 <sup>†</sup>
100713B	23:31:34	-0.38	7.23	82.06	13	4.3*	2.15 <sup>†</sup>	$1.9 \times 10^{-15}$	205.0 <sup>†</sup>	1.05 <sup>†</sup>	2.25 <sup>†</sup>
100714A	16:07:24	-0.51	35.07	106.37	51.14	4.2*	2.15 <sup>†</sup>	$2.0 \times 10^{-15}$	205.0 <sup>†</sup>	1.05 <sup>†</sup>	2.25 <sup>†</sup>
100714B	16:27:20	-2.88	5.56	307.94	61.3	9.9*	2.15 <sup>†</sup>	$1.5 \times 10^{-15}$	205.0 <sup>†</sup>	1.05 <sup>†</sup>	2.25 <sup>†</sup>
100717A	08:55:06	-0.58	5.38	287.06	-0.66	9.1*	2.15 <sup>†</sup>	$2.7 \times 10^{-16}$	205.0 <sup>†</sup>	1.05 <sup>†</sup>	2.25 <sup>†</sup>
100717B	10:41:47	-0.13	2.3	304.31	19.53	9.4*	2.15 <sup>†</sup>	$2.1 \times 10^{-16}$	205.0 <sup>†</sup>	1.05 <sup>†</sup>	2.25 <sup>†</sup>
100718B	03:50:10	-21.62	11.02	121.83	-46.18	6.3*	2.15 <sup>†</sup>	$1.7 \times 10^{-15}$	205.0 <sup>†</sup>	1.05 <sup>†</sup>	2.25 <sup>†</sup>
100719C	19:48:09	-2.3	0.77	231.41	18.56	10.5*	2.15 <sup>†</sup>	$1.7 \times 10^{-16}$	205.0 <sup>†</sup>	1.05 <sup>†</sup>	2.25 <sup>†</sup>

Table A.2: IC86-1 GRB Catalog (continued)

Name	Time			Position					Fluence				
	$T_0$	$T_1$	$T_2$	$\alpha$	$\delta$	$\sigma$	$z$	$f_\gamma$	$\epsilon_\gamma$	$\alpha_\gamma$	$\beta_\gamma$		
100719D	23:44:04	1.54	23.36	113.3	5.4	2.3*	2.15 <sup>†</sup>	$3.2 \times 10^{-14}$	205.0 <sup>†</sup>	1.05 <sup>†</sup>	2.25 <sup>†</sup>		
100722B	06:58:25	-1.22	0.06	31.81	56.23	8.3*	0.5 <sup>†</sup>	$1.6 \times 10^{-17}$	205.0 <sup>†</sup>	1.05 <sup>†</sup>	2.25 <sup>†</sup>		
100724B	00:42:04	-4.1	230.608	120.04	76.74	1.1	2.15 <sup>†</sup>	$2.4 \times 10^{-12}$	467.8	0.84	1.84		
100725B	11:24:34	-4.8	226.1	290.033	76.956	0.0005	2.15 <sup>†</sup>	$5.4 \times 10^{-15}$	200.0 <sup>†</sup>	1.89	2.89		
100728B	10:31:55	-2.05	13.2	163.488	-45.473	0.0001	2.15 <sup>†</sup>	$5.4 \times 10^{-16}$	104.0	0.8	2.2		
100802A	05:45:36	-3.3	531.7	2.468	47.755	0.0006	2.15 <sup>†</sup>	$1.9 \times 10^{-15}$	149.0	1.17	3.17		
100804A	02:29:26	0.13	6.72	248.97	27.45	2.3*	2.15 <sup>†</sup>	$6.7 \times 10^{-15}$	205.0 <sup>†</sup>	1.05 <sup>†</sup>	2.25 <sup>†</sup>		
100805A	04:12:42	-1.4	17.1	299.877	52.628	0.0001	2.15 <sup>†</sup>	$5.3 \times 10^{-16}$	200.0 <sup>†</sup>	1.76	2.76		
100805B	07:12:12	-0.1	-0.03	22.8	34.19	7.9*	0.5 <sup>†</sup>	$3.1 \times 10^{-17}$	205.0 <sup>†</sup>	1.05 <sup>†</sup>	2.25 <sup>†</sup>		
100807A	09:13:13	-6.1	3.1	55.3	67.672	0.0005	2.15 <sup>†</sup>	$1.4 \times 10^{-16}$	200.0 <sup>†</sup>	2.32	3.32		
100810A	01:10:34	-1.86	0.7	124.77	-1.61	6.0*	2.15 <sup>†</sup>	$2.5 \times 10^{-16}$	205.0 <sup>†</sup>	1.05 <sup>†</sup>	2.25 <sup>†</sup>		
100811A	02:35:49	-0.06	0.32	345.87	15.86	6.4*	0.5 <sup>†</sup>	$4.5 \times 10^{-16}$	205.0 <sup>†</sup>	1.05 <sup>†</sup>	2.25 <sup>†</sup>		
100811B	18:44:10	-52.99	25.09	108.14	62.19	4.1*	2.15 <sup>†</sup>	$2.9 \times 10^{-15}$	205.0 <sup>†</sup>	1.05 <sup>†</sup>	2.25 <sup>†</sup>		
100814B	08:25:26	-0.77	6.66	122.82	18.49	3.3*	2.15 <sup>†</sup>	$9.1 \times 10^{-16}$	81.0	0.62	2.49		
100816A	00:37:51	-0.7	10.448	351.74	26.579	0.0004	0.8049	$2.8 \times 10^{-16}$	136.7	0.31	2.77		
100823A	17:25:33	0	25	20.704	5.835	0.0006	2.15 <sup>†</sup>	$2.0 \times 10^{-16}$	200.0 <sup>†</sup>	2.19	3.19		
100827A	10:55:49	-0.13	0.45	193.9	71.89	6.0*	0.5 <sup>†</sup>	$1.6 \times 10^{-16}$	205.0 <sup>†</sup>	1.05 <sup>†</sup>	2.25 <sup>†</sup>		
100829A	21:02:07	0	10.8	90.409	30.314	0.808	2.15 <sup>†</sup>	$4.4 \times 10^{-14}$	278.0	1.44	9.4		
100829B	08:59:07	0.26	95.23	115.45	-3.99	5.1*	2.15 <sup>†</sup>	$4.6 \times 10^{-15}$	205.0 <sup>†</sup>	1.05 <sup>†</sup>	2.25 <sup>†</sup>		
100831A	15:37:26	-23.3	16.9	161.26	33.65	10.4*	2.15 <sup>†</sup>	$1.8 \times 10^{-15}$	205.0 <sup>†</sup>	1.05 <sup>†</sup>	2.25 <sup>†</sup>		
100901A	13:34:10	-2.4	471.8	27.265	22.759	0.0006	1.408	$1.5 \times 10^{-15}$	200.0 <sup>†</sup>	1.52	2.52		
100902A	19:31:54	-49.5	409.6	48.629	30.979	0.0004	2.15 <sup>†</sup>	$2.2 \times 10^{-15}$	200.0 <sup>†</sup>	1.98	2.98		

Table A.2: IC86-1 GRB Catalog (continued)

Name	Time			Position					Fluence				
	$T_0$	$T_1$	$T_2$	$\alpha$	$\delta$	$\sigma$	$z$	$f_\gamma$	$\epsilon_\gamma$	$\alpha_\gamma$	$\beta_\gamma$		
100902B	23:45:20	-4.1	18.18	306.04	42.31	7.5*	2.15 <sup>†</sup>	$1.3 \times 10^{-15}$	205.0 <sup>†</sup>	1.05 <sup>†</sup>	2.25 <sup>†</sup>		
100905A	15:08:14	-1.6	2.1	31.55	14.929	0.0004	2.15 <sup>†</sup>	$1.1 \times 10^{-15}$	200.0 <sup>†</sup>	1.09	2.09		
100905B	21:46:23	-4.61	6.91	262.65	13.08	4.5*	2.15 <sup>†</sup>	$1.2 \times 10^{-15}$	205.0 <sup>†</sup>	1.05 <sup>†</sup>	2.25 <sup>†</sup>		
100906A	13:49:27	-0.2	142.264	28.684	55.631	0.0004	1.727	$2.7 \times 10^{-15}$	106.0	1.34	1.98		
100909A	09:04:00	0	60	73.951	54.654	0.0333	2.15 <sup>†</sup>	$6.2 \times 10^{-14}$	200.0 <sup>†</sup>	1.0 <sup>†</sup>	2.0 <sup>†</sup>		
100911A	19:35:40	-0.77	4.86	151.32	58.99	11.9*	2.15 <sup>†</sup>	$5.4 \times 10^{-16}$	205.0 <sup>†</sup>	1.05 <sup>†</sup>	2.25 <sup>†</sup>		
100915A	01:31:05	-36.3	72.2	315.694	65.673	0.0004	2.15 <sup>†</sup>	$3.1 \times 10^{-15}$	265.2	1.5	3.5		
100915B	05:49:40	-7.42	3	85.394	25.095	2.0*	2.15 <sup>†</sup>	$1.9 \times 10^{-16}$	83.49	1.35	3.35		
100919A	21:12:17	-38.4	11.2	163.24	6.02	2.7*	2.15 <sup>†</sup>	$3.6 \times 10^{-15}$	205.0 <sup>†</sup>	1.05 <sup>†</sup>	2.25 <sup>†</sup>		
100923A	20:15:10	-0.77	50.94	106.12	39.6	5.7*	2.15 <sup>†</sup>	$2.5 \times 10^{-15}$	205.0 <sup>†</sup>	1.05 <sup>†</sup>	2.25 <sup>†</sup>		
100924A	03:58:08	-15.1	128.9	0.672	7.004	0.0167	2.15 <sup>†</sup>	$2.4 \times 10^{-15}$	200.0 <sup>†</sup>	1.59	2.59		
100929A	05:38:53	-2.3	5.89	166.33	62.29	13.5*	2.15 <sup>†</sup>	$3.1 \times 10^{-16}$	205.0 <sup>†</sup>	1.05 <sup>†</sup>	2.25 <sup>†</sup>		
100929B	07:33:04	-0.51	4.1	243.62	33.33	23.9*	2.15 <sup>†</sup>	$2.0 \times 10^{-16}$	205.0 <sup>†</sup>	1.05 <sup>†</sup>	2.25 <sup>†</sup>		
101003A	05:51:08	-1.79	8.19	175.85	2.49	7.7*	2.15 <sup>†</sup>	$1.4 \times 10^{-15}$	205.0 <sup>†</sup>	1.05 <sup>†</sup>	2.25 <sup>†</sup>		
101008A	16:43:15	-4	106.6	328.875	37.067	0.0006	2.15 <sup>†</sup>	$2.0 \times 10^{-15}$	200.0 <sup>†</sup>	1.42	2.42		
101010A	04:33:47	-11.01	54.02	47.19	43.56	18.7*	2.15 <sup>†</sup>	$9.7 \times 10^{-16}$	205.0 <sup>†</sup>	1.05 <sup>†</sup>	2.25 <sup>†</sup>		
101015A	13:24:03	-2.05	498.5	73.16	15.46	6.3*	2.15 <sup>†</sup>	$2.3 \times 10^{-14}$	205.0 <sup>†</sup>	1.05 <sup>†</sup>	2.25 <sup>†</sup>		
101016A	05:50:16	-1.54	2.3	133.04	-4.62	3.5*	2.15 <sup>†</sup>	$1.5 \times 10^{-15}$	205.0 <sup>†</sup>	1.05 <sup>†</sup>	2.25 <sup>†</sup>		
101020A	23:40:41	-50	159	189.607	23.129	0.0567	2.15 <sup>†</sup>	$1.6 \times 10^{-15}$	200.0 <sup>†</sup>	2.04	3.04		
101021B	01:30:32	-0.51	1.02	0.46	47.34	13.0*	0.5 <sup>†</sup>	$4.5 \times 10^{-17}$	205.0 <sup>†</sup>	1.05 <sup>†</sup>	2.25 <sup>†</sup>		
101026A	00:49:16	-0.13	0.13	263.7	-0.37	7.8*	0.5 <sup>†</sup>	$1.4 \times 10^{-16}$	205.0 <sup>†</sup>	1.05 <sup>†</sup>	2.25 <sup>†</sup>		
101027A	05:30:30	-1.28	0.06	79.02	43.97	11.6*	0.5 <sup>†</sup>	$2.2 \times 10^{-17}$	205.0 <sup>†</sup>	1.05 <sup>†</sup>	2.25 <sup>†</sup>		

Table A.2: IC86-1 GRB Catalog (continued)

Name	Time			Position				Fluence			
	$T_0$	$T_1$	$T_2$	$\alpha$	$\delta$	$\sigma$	$z$	$f_\gamma$	$\epsilon_\gamma$	$\alpha_\gamma$	$\beta_\gamma$
101101A	17:51:34	-2.3	1.02	13.55	45.75	3.7*	2.15 <sup>†</sup>	$4.1 \times 10^{-16}$	205.0 <sup>†</sup>	1.05 <sup>†</sup>	2.25 <sup>†</sup>
101107A	00:16:26	2.3	378.12	168.33	22.43	4.6*	2.15 <sup>†</sup>	$4.5 \times 10^{-15}$	205.0 <sup>†</sup>	1.05 <sup>†</sup>	2.25 <sup>†</sup>
101112A	22:10:24	0	15.448	292.218	39.359	2.0*	2.15 <sup>†</sup>	$5.9 \times 10^{-16}$	105.8	0.79	2.02
101112B	23:36:56	-9.47	73.47	100.1	9.62	5.5*	2.15 <sup>†</sup>	$5.4 \times 10^{-15}$	205.0 <sup>†</sup>	1.05 <sup>†</sup>	2.25 <sup>†</sup>
101113A	11:35:36	-0.26	12.03	29.08	0.21	3.4*	2.15 <sup>†</sup>	$1.9 \times 10^{-15}$	205.0 <sup>†</sup>	1.05 <sup>†</sup>	2.25 <sup>†</sup>
101114A	00:32:50	-2.2	6.6	303.193	14.029	0.03	2.15 <sup>†</sup>	$8.0 \times 10^{-15}$	296.0	1.15	3.15
101119A	16:27:03	-0.32	0.32	226.49	59.61	16.3*	0.5 <sup>†</sup>	$2.6 \times 10^{-17}$	205.0 <sup>†</sup>	1.05 <sup>†</sup>	2.25 <sup>†</sup>
101123A	22:51:35	41.47	161.272	131.381	5.563	1.022	2.15 <sup>†</sup>	$3.2 \times 10^{-13}$	476.0	0.75	2.14
101127A	02:13:59	-3.33	26.11	290.31	7.89	23.3*	2.15 <sup>†</sup>	$4.4 \times 10^{-16}$	205.0 <sup>†</sup>	1.05 <sup>†</sup>	2.25 <sup>†</sup>
101129B	17:25:25	-0.06	0.51	271.54	1.01	8.5*	0.5 <sup>†</sup>	$1.2 \times 10^{-16}$	205.0 <sup>†</sup>	1.05 <sup>†</sup>	2.25 <sup>†</sup>
101130B	01:45:55	-2.3	2.56	274.61	26.62	23.7*	2.15 <sup>†</sup>	$1.5 \times 10^{-16}$	205.0 <sup>†</sup>	1.05 <sup>†</sup>	2.25 <sup>†</sup>
101202A	03:41:54	0	18.43	254.02	58.48	6.5*	2.15 <sup>†</sup>	$8.8 \times 10^{-16}$	205.0 <sup>†</sup>	1.05 <sup>†</sup>	2.25 <sup>†</sup>
101204B	08:14:19	-0.06	0.06	191.91	55.67	10.6*	0.5 <sup>†</sup>	$4.3 \times 10^{-17}$	205.0 <sup>†</sup>	1.05 <sup>†</sup>	2.25 <sup>†</sup>
101207A	12:51:42	5.63	67.07	175.75	8.72	4.3*	2.15 <sup>†</sup>	$4.2 \times 10^{-15}$	205.0 <sup>†</sup>	1.05 <sup>†</sup>	2.25 <sup>†</sup>
101208A	04:52:57	-0.19	10	212.4	4.04	11.9*	0.5 <sup>†</sup>	$4.8 \times 10^{-17}$	205.0 <sup>†</sup>	1.05 <sup>†</sup>	2.25 <sup>†</sup>
101211A	11:37:55	-2.82	10.75	31.84	10.06	11.4*	2.15 <sup>†</sup>	$1.0 \times 10^{-15}$	205.0 <sup>†</sup>	1.05 <sup>†</sup>	2.25 <sup>†</sup>
101213A	10:49:19	-1	201.1	241.314	21.897	0.0005	0.414	$9.1 \times 10^{-16}$	309.7	1.1	2.35
101219A	02:31:29	0	5.6	74.586	-2.527	0.0167	2.15 <sup>†</sup>	$2.5 \times 10^{-14}$	490.0	0.22	2.22
101220A	13:49:59	2.3	74.75	241.57	46.14	2.4*	2.15 <sup>†</sup>	$6.0 \times 10^{-15}$	205.0 <sup>†</sup>	1.05 <sup>†</sup>	2.25 <sup>†</sup>
101220B	20:43:54	-1.02	30.72	2.7	27.2	2.5*	2.15 <sup>†</sup>	$3.3 \times 10^{-15}$	205.0 <sup>†</sup>	1.05 <sup>†</sup>	2.25 <sup>†</sup>
101223A	20:00:19	-41.22	14.85	250.55	48.22	4.8*	2.15 <sup>†</sup>	$1.5 \times 10^{-15}$	205.0 <sup>†</sup>	1.05 <sup>†</sup>	2.25 <sup>†</sup>
101224A	05:27:13	0	2.66	285.939	45.706	0.035	2.15 <sup>†</sup>	$8.6 \times 10^{-16}$	330.0	0.83	2.83

Table A.2: IC86-1 GRB Catalog (continued)

Name	Time			Position				Fluence			
	$T_0$	$T_1$	$T_2$	$\alpha$	$\delta$	$\sigma$	$z$	$f_\gamma$	$\epsilon_\gamma$	$\alpha_\gamma$	$\beta_\gamma$
101224C	14:43:33	-2.56	23.04	290.16	34.46	9.1*	2.15 <sup>†</sup>	$1.6 \times 10^{-15}$	205.0 <sup>†</sup>	1.05 <sup>†</sup>	2.25 <sup>†</sup>
101225A	18:37:45	0	963	0.198	44.6	0.0004	2.15 <sup>†</sup>	$2.8 \times 10^{-15}$	200.0 <sup>†</sup>	1.82	2.82
101225B	09:02:54	20.54	101.76	60.68	32.77	2.7*	2.15 <sup>†</sup>	$1.3 \times 10^{-14}$	205.0 <sup>†</sup>	1.05 <sup>†</sup>	2.25 <sup>†</sup>
101231A	01:36:51	0	23.62	191.71	17.64	2.5*	2.15 <sup>†</sup>	$1.1 \times 10^{-14}$	205.0 <sup>†</sup>	1.05 <sup>†</sup>	2.25 <sup>†</sup>
110101A	04:50:20	-2.3	1.28	264.26	36.54	11.4*	2.15 <sup>†</sup>	$1.6 \times 10^{-16}$	205.0 <sup>†</sup>	1.05 <sup>†</sup>	2.25 <sup>†</sup>
110101B	12:08:22	-103.43	132.1	105.5	34.58	16.6*	2.15 <sup>†</sup>	$4.1 \times 10^{-15}$	205.0 <sup>†</sup>	1.05 <sup>†</sup>	2.25 <sup>†</sup>
110102A	18:52:25	-49.2	294.9	245.881	7.614	0.0001	2.15 <sup>†</sup>	$3.8 \times 10^{-14}$	267.0	1.22	2.3
110106A	15:25:16	-1	3.9	79.306	64.173	0.0005	2.15 <sup>†</sup>	$3.5 \times 10^{-16}$	200.0 <sup>†</sup>	1.71	2.71
110106B	21:26:16	-16.9	24.5	134.154	47.003	0.0005	0.618	$4.7 \times 10^{-16}$	200.0 <sup>†</sup>	1.61	2.61
110107A	21:15:51	-70	122.37	299.89	41.889	0.05	2.15 <sup>†</sup>	$9.1 \times 10^{-15}$	200.0 <sup>†</sup>	1.58	2.58
110112A	04:12:18	-0.1	0.5	329.932	26.456	0.0009	0.5 <sup>†</sup>	$9.6 \times 10^{-18}$	1000.0 <sup>†</sup>	2.14	3.14
110112B	22:24:54	0	2.34	10.6	64.41	2.0*	2.15 <sup>†</sup>	$1.2 \times 10^{-15}$	495.0	0.72	2.72
110117A	08:44:51	-1.79	70.66	130.87	47.59	9.8*	2.15 <sup>†</sup>	$1.6 \times 10^{-15}$	205.0 <sup>†</sup>	1.05 <sup>†</sup>	2.25 <sup>†</sup>
110119A	22:20:58	-86.4	217.5	348.586	5.986	0.0005	2.15 <sup>†</sup>	$3.7 \times 10^{-15}$	126.3	0.6	1.95
110123A	19:17:45	0.7	18.56	246.97	28.03	2.3*	2.15 <sup>†</sup>	$2.8 \times 10^{-14}$	280.0	0.64	1.96
110124A	18:49:09	-3.33	2.05	53.83	36.35	9.4*	2.15 <sup>†</sup>	$9.9 \times 10^{-17}$	205.0 <sup>†</sup>	1.05 <sup>†</sup>	2.25 <sup>†</sup>
110130A	05:31:53	-0.26	47.1	111.51	38.25	7.1*	2.15 <sup>†</sup>	$1.8 \times 10^{-15}$	205.0 <sup>†</sup>	1.05 <sup>†</sup>	2.25 <sup>†</sup>
110201A	09:35:08	-2.8	13.3	137.489	88.61	0.0217	2.15 <sup>†</sup>	$4.4 \times 10^{-15}$	200.0 <sup>†</sup>	1.09	2.09
110205A	02:02:41	0	330	164.63	67.525	0.0004	2.22	$3.5 \times 10^{-14}$	222.0	1.52	3.52
110206B	04:50:36	-6.4	5.89	333.7	1.61	15.6*	2.15 <sup>†</sup>	$4.9 \times 10^{-16}$	205.0 <sup>†</sup>	1.05 <sup>†</sup>	2.25 <sup>†</sup>
110210A	09:52:41	-102.9	153.6	13.057	7.78	0.0005	2.15 <sup>†</sup>	$1.1 \times 10^{-15}$	200.0 <sup>†</sup>	1.73	2.73
110212A	01:09:08	-1.8	2.6	69.025	43.716	0.0233	2.15 <sup>†</sup>	$7.0 \times 10^{-17}$	44.6	0.78	2.78

Table A.2: IC86-1 GRB Catalog (continued)

Name	Time			Position				Fluence			
	$T_0$	$T_1$	$T_2$	$\alpha$	$\delta$	$\sigma$	$z$	$f_\gamma$	$\epsilon_\gamma$	$\alpha_\gamma$	$\beta_\gamma$
110213A	05:17:29	-31.2	32.8	42.964	49.273	0.0004	2.15 <sup>†</sup>	$2.3 \times 10^{-15}$	89.0	1.28	2.4
110213B	14:31:33	0	50	41.768	0.952	0.0087	1.083	$2.6 \times 10^{-15}$	123.0	1.52	3.52
110213C	21:00:52	-0.13	0.19	6.28	27.54	11.0*	0.5 <sup>†</sup>	$5.0 \times 10^{-18}$	205.0 <sup>†</sup>	1.05 <sup>†</sup>	2.25 <sup>†</sup>
110220A	18:16:22	-1.79	31.23	185.49	16.58	6.4*	2.15 <sup>†</sup>	$1.3 \times 10^{-15}$	205.0 <sup>†</sup>	1.05 <sup>†</sup>	2.25 <sup>†</sup>
110221A	05:51:20	-1.54	11.52	15.18	66.05	2.4*	2.15 <sup>†</sup>	$1.4 \times 10^{-15}$	205.0 <sup>†</sup>	1.05 <sup>†</sup>	2.25 <sup>†</sup>
110223A	20:56:59	0.1	8.1	345.854	87.558	0.0006	2.15 <sup>†</sup>	$1.3 \times 10^{-15}$	200.0 <sup>†</sup>	1.0 <sup>†</sup>	2.0 <sup>†</sup>
110226A	23:44:31	-2.3	11.78	199.29	35.77	7.4*	2.15 <sup>†</sup>	$1.2 \times 10^{-15}$	205.0 <sup>†</sup>	1.05 <sup>†</sup>	2.25 <sup>†</sup>
110227B	05:30:11	-1.02	17.41	25.24	15.89	7.7*	2.15 <sup>†</sup>	$1.5 \times 10^{-15}$	205.0 <sup>†</sup>	1.05 <sup>†</sup>	2.25 <sup>†</sup>
110228B	18:59:51	-3.84	13.31	245.09	16.41	5.2*	2.15 <sup>†</sup>	$6.0 \times 10^{-16}$	205.0 <sup>†</sup>	1.05 <sup>†</sup>	2.25 <sup>†</sup>
110301A	05:08:43	0	5.7	229.35	29.4	2.3*	2.15 <sup>†</sup>	$1.3 \times 10^{-14}$	106.8	0.81	2.7
110302A	01:01:52	-11.2	27.14	122.35	2.91	7.1*	2.15 <sup>†</sup>	$2.3 \times 10^{-15}$	205.0 <sup>†</sup>	1.05 <sup>†</sup>	2.25 <sup>†</sup>
110304A	01:42:34	-0.26	19.26	322.93	33.27	4.7*	2.15 <sup>†</sup>	$2.2 \times 10^{-15}$	205.0 <sup>†</sup>	1.05 <sup>†</sup>	2.25 <sup>†</sup>
110307A	23:19:08	-1.79	0.51	193.12	15.64	7.8*	2.15 <sup>†</sup>	$3.6 \times 10^{-16}$	205.0 <sup>†</sup>	1.05 <sup>†</sup>	2.25 <sup>†</sup>
110311A	19:29:22	-1.79	4.61	117.59	34.29	9.9*	2.15 <sup>†</sup>	$7.0 \times 10^{-16}$	205.0 <sup>†</sup>	1.05 <sup>†</sup>	2.25 <sup>†</sup>
110315A	23:57:04	-66.8	38.8	279.195	17.539	0.0004	2.15 <sup>†</sup>	$4.2 \times 10^{-15}$	200.0 <sup>†</sup>	1.77	2.77
110328A	12:57:45	0	10	251.208	57.583	0.0005	2.15 <sup>†</sup>	$2.5 \times 10^{-14}$	200.0 <sup>†</sup>	1.0 <sup>†</sup>	2.0 <sup>†</sup>
110328B	12:29:20	1.02	142.34	117.65	43.1	2.7*	2.15 <sup>†</sup>	$2.9 \times 10^{-14}$	369.0	1.11	1.94
110331A	14:29:07	-0.06	3.14	6.66	25.99	5.1*	2.15 <sup>†</sup>	$1.6 \times 10^{-16}$	205.0 <sup>†</sup>	1.05 <sup>†</sup>	2.25 <sup>†</sup>
110401A	22:04:20	-0.64	1.73	268.56	26.87	4.3*	2.15 <sup>†</sup>	$1.7 \times 10^{-14}$	1194.0	0.66	2.36
110402A	00:12:58	-1.5	83.5	197.402	61.253	0.0006	2.15 <sup>†</sup>	$1.3 \times 10^{-13}$	1395.0	1.03	3.03
110406A	03:44:06	0	9.216	17.34	35.809	0.0089	2.15 <sup>†</sup>	$3.9 \times 10^{-14}$	326.0	1.24	2.3
110407A	14:06:41	-2.9	158.8	186.031	15.712	0.0006	2.15 <sup>†</sup>	$7.9 \times 10^{-16}$	57.9	0.73	2.73



Table A.2: IC86-1 GRB Catalog (continued)

Name	Time				Position				Fluence			
	$T_0$	$T_1$	$T_2$	$\alpha$	$\delta$	$\sigma$	$z$	$f_\gamma$	$\epsilon_\gamma$	$\alpha_\gamma$	$\beta_\gamma$	
110411A	19:34:11	-11.9	86.3	291.442	67.712	0.0005	2.15 <sup>†</sup>	$1.1 \times 10^{-15}$	41.0	1.51	3.51	
110412A	07:33:21	13.7	40.4	133.491	13.488	0.0317	2.15 <sup>†</sup>	$1.4 \times 10^{-15}$	87.0	0.7	2.7	
110414A	07:42:14	-38.4	135.6	97.873	24.362	0.0004	2.15 <sup>†</sup>	$2.9 \times 10^{-14}$	200.0 <sup>†</sup>	1.0 <sup>†</sup>	2.0 <sup>†</sup>	
110421A	18:10:40	-2.56	37.89	277.23	50.8	2.7*	2.15 <sup>†</sup>	$6.6 \times 10^{-15}$	205.0 <sup>†</sup>	1.05 <sup>†</sup>	2.25 <sup>†</sup>	
110422B	00:41:49	-0.13	0.19	226.69	43.02	21.6*	0.5 <sup>†</sup>	$1.2 \times 10^{-17}$	205.0 <sup>†</sup>	1.05 <sup>†</sup>	2.25 <sup>†</sup>	
110428B	08:07:05	-53.76	47.87	128.44	19.94	3.6*	2.15 <sup>†</sup>	$9.9 \times 10^{-15}$	205.0 <sup>†</sup>	1.05 <sup>†</sup>	2.25 <sup>†</sup>	
110430A	09:00:14	1.02	33.54	147.06	67.95	3.2*	2.15 <sup>†</sup>	$4.4 \times 10^{-15}$	205.0 <sup>†</sup>	1.05 <sup>†</sup>	2.25 <sup>†</sup>	
110503A	17:35:45	-6.6	16.3	132.776	52.208	0.0001	1.61	$1.2 \times 10^{-14}$	219.0	0.98	2.7	

Reason for omission	IC79 bursts	IC86-1 bursts
no run	110128A, 110131A, 110217A	110529A, 110705A, 120102A, 120204A, 120403A
test run	110413A, 110415A, 110422A	120116A
calibration run		110728A, 120218B
unstable run		110609A, 120513A

Table A.3: Summary of northern bursts omitted from the IC79 and IC86-1 catalogs for this experiment.

## Bibliography

- [1] V. F. Hess. Über Beobachtungen der durchdringenden Strahlung bei sieben Freiballonfahrten. *Physikalische Zeitschrift*, 13:1084–1901, 1912.
- [2] M. Ackermann et al. Detection of the Characteristic Pion-Decay Signature in Supernova Remnants. *Science*, 339:807, 2013.
- [3] A. M. Hillas. The Origin of Ultra-High-Energy Cosmic Rays. *ARA&A*, 22:425–444, 1984.
- [4] L. Anchordoqui, T. Paul, S. Reucroft, and J. Swain. Ultrahigh Energy Cosmic Rays: The State of the Art Before the Auger Observatory. *Int. J. Mod. Phys. A*, 18:2229–2366, 2003. (The figure is from Murat Boratav).
- [5] A. Domínguez, J. D. Finke, F. Prada, et al. Detection of the Cosmic  $\gamma$ -Ray Horizon from Multiwavelength Observations of Blazars. *ApJ*, 770:77, June 2013.
- [6] R. Abbasi et al. Search for muon neutrinos from gamma-ray bursts with the icecube neutrino telescope. *ApJ*, 710:346–359, 2010.
- [7] R. Abbasi et al. An absence of neutrinos associated with cosmic ray acceleration in gamma-ray bursts. *Nature*, 484:351–354, 2012.
- [8] NASA. The Vela-5B Satellite. Website.
- [9] R. W. Klebesadel, I. B. Strong, and R. A. Olson. Observations of Gamma-Ray Bursts of Cosmic Origin. *ApJ*, 182:L85–+, June 1973.
- [10] NASA. BATSE: Burst and Transient Source Experiment. Website.
- [11] W. S. Paciesas, C. A. Meegan, G. N. Pendleton, et al. The Fourth BATSE Gamma-Ray Burst Catalog (Revised). *ApJS*, 122:465–495, June 1999.
- [12] G. J. Fishman and C. A. Meegan. Gamma-Ray Bursts. *ARA&A*, 33:415–458, 1995.
- [13] L. Piro. The Beppo-SAX experiment (overview). In J. D. Hadjidemetriou & J. H. Seiradakis, editor, *Joint European and National Astronomical Meeting*, 1997.
- [14] E. Costa, F. Frontera, J. Heise, et al. Discovery of an X-ray afterglow associated with the  $\gamma$ -ray burst of 28 February 1997. *Nature*, 387:783–785, June 1997.
- [15] M. R. Metzger, S. G. Djorgovski, S. R. Kulkarni, et al. Spectral Constraints on the Redshift of the Optical Counterpart to the  $\gamma$ -Ray Burst of 8 May 1997. *Nature*, 387:878–880, June 1997.

- [16] J. P. Halpern, J. R. Thorstensen, D. J. Helfand, and E. Costa. Optical Afterglow of the  $\gamma$ -Ray Burst of 14 December 1997. *Nature*, 393:41–43, May 1998.
- [17] A. N. Ramaprakash, S. R. Kulkarni, D. A. Frail, et al. The Energetic Afterglow of the  $\gamma$ -Ray Burst of 14 December 1997. *Nature*, 393:43–46, May 1998.
- [18] NASA. HETE-2: The high energy transient explorer mission, 2000.
- [19] Krzysztof Z. Stanek et al. Spectroscopic Discovery of the Supernova 2003dh Associated with GRB 030329. *Astrophys. J.*, 591:L17–L20, 2003.
- [20] Derek B. Fox et al. The afterglow of GRB050709 and the nature of the short- hard gamma-ray bursts. *Nature*, 437:845–850, 2005.
- [21] N. Gehrels et al. The swift gamma-ray burst mission. *ApJ*, 611:1005–1020, 2004.
- [22] NASA. The swift gamma ray burst mission, 2004.
- [23] N. Kawai, G. Kosugi, K. Aoki, et al. An Optical Spectrum of the Afterglow of a  $\gamma$ -Ray Burst at a Redshift of  $z = 6.295$ . *Nature*, 440:184–186, March 2006.
- [24] J. Greiner, T. Krühler, J. P. U. Fynbo, et al. GRB 080913 at Redshift 6.7. *ApJ*, 693:1610–1620, March 2009.
- [25] N. R. Tanvir, D. B. Fox, A. J. Levan, et al. A  $\gamma$ -Ray Burst at a Redshift of  $z \approx 8.2$ . *Nature*, 461:1254–1257, October 2009.
- [26] R. Salvaterra, M. Della Valle, S. Campana, et al. GRB090423 at a Redshift of  $z \approx 8.1$ . *Nature*, 461:1258–1260, October 2009.
- [27] NASA. Fermi: Gamma ray space telescope, 2008.
- [28] W. B. Atwood, A. A. Abdo, M. Ackermann, et al. The Large Area Telescope on the Fermi Gamma-Ray Space Telescope Mission. *ApJ*, 697:1071–1102, June 2009.
- [29] C. Meegan, G. Lichti, P. N. Bhat, et al. THE fermi gamma-ray burst monitor. *ApJ*, 702:791–804, September 2009.
- [30] W.S. Paciesas et al. The fermi gbm gamma-ray burst catalog: The first two years. *ApJS*, 199:18, 2012.
- [31] D. N. Burrows, J. E. Hill, J. A. Nousek, et al. The SwiftX-Ray Telescope. *Space Sci. Rev.*, 120:165–195, October 2005.

- [32] NASA. Wind spacecraft. <http://science.nasa.gov/missions/wind/>, 1994.
- [33] R. L. Aptekar, D. D. Frederiks, S. V. Golenetskii, et al. Konus-W Gamma-Ray Burst Experiment for the GGS Wind Spacecraft. *Space Sci. Rev.*, 71:265–272, February 1995.
- [34] C. Winkler, T. J.-L. Courvoisier, G. Di Cocco, et al. The INTEGRAL Mission. *A&A*, 411:L1–L6, November 2003.
- [35] JAXA. Monitor of all-sky x-ray image. <http://kibo.jaxa.jp/en/experiment/ef/maxi/>, 2009.
- [36] NASA. International space station. [http://www.nasa.gov/mission\\_pages/station/main/](http://www.nasa.gov/mission_pages/station/main/), 1998.
- [37] M. Feroci, E. Costa, P. Soffitta, et al. SuperAGILE: The Hard X-Ray Imager for the AGILE Space Mission. *NIMA*, 581:728–754, November 2007.
- [38] T. Takahashi, K. Abe, M. Endo, et al. Hard X-Ray Detector (HXD) on Board Suzaku. *PASJ*, 59:35–51, January 2007.
- [39] K. Yamaoka, A. Endo, T. Enoto, et al. Design and In-Orbit Performance of the Suzaku Wide-Band All-Sky Monitor. *PASJ*, 61:35–+, January 2009.
- [40] K. Hurley, S. Golenetskii, R. Aptekar, et al. The Third Interplanetary Network. In N. Kawai and S. Nagataki, editors, *Deciphering the Ancient Universe with Gamma-Ray Bursts*, volume 1279 of *American Institute of Physics Conference Series*, pages 330–333, October 2010.
- [41] NASA. 2001 mars odyssey. [http://www.nasa.gov/mission\\_pages/station/main/](http://www.nasa.gov/mission_pages/station/main/), 2001.
- [42] NASA. Reuven ramaty high energy solar spectroscopic imager. <http://hesperia.gsfc.nasa.gov/rhessi3/>, 2002.
- [43] NASA. Messenger. <http://messenger.jhuapl.edu/>, 2004.
- [44] NASA. GCN: The Gamma-Ray Bursts Coordinates Network. <http://gcn.gsfc.nasa.gov/>.
- [45] GRB-web. <http://grbweb.icecube.wisc.edu>.
- [46] A. Goldstein et al. The fermi gbm gamma-ray burst spectral catalog: The first two years. *ApJS*, 199:19, 2012.
- [47] Andreas von Kienlin, Charles A. Meegan, William S. Paciesas, et al. The Second Fermi GBM Gamma-Ray Burst Catalog: The First Four Years. *Astrophys.J.Suppl.*, 211:13, 2014.

- [48] David Gruber, Adam Goldstein, Victoria Weller von Ahlefeld, et al. The Fermi GBM Gamma-Ray Burst Spectral Catalog: Four Years Of Data. *Astrophys.J.Suppl.*, 211:12, 2014.
- [49] D. Band et al. BATSE observations of gamma-ray burst spectra. 1. Spectral diversity. *Astrophys. J.*, 413:281–292, 1993.
- [50] Julia K. Becker. *Neutrinos on the Rocks: On the Phenomenology of Potential Astrophysical Neutrino Sources*. PhD thesis, Technische Universität Dortmund, Germany, 2007.
- [51] R. Abbasi, Y. Abdou, T. Abu-Zayyad, et al. Search for Muon Neutrinos from Gamma-Ray Bursts with the IceCube Neutrino Telescope. *ApJ*, 710:346–359, February 2010.
- [52] E. Waxman. Cosmological gamma-ray bursts and the highest energy cosmic rays. *Phys. Rev. Lett.*, 75:386–389, 1995.
- [53] Eli Waxman. High-energy cosmic rays from gamma-ray burst sources: A stronger case. *The Astrophysical Journal*, 606(2):988, 2004.
- [54] P. Baerwald, M. Bustamante, and W. Winter. UHECR Escape Mechanisms for Protons and Neutrons from Gamma-Ray Bursts, and the Cosmic-Ray-Neutrino Connection. *ApJ*, 768:186, May 2013.
- [55] P. Baerwald, M. Bustamante, and W. Winter. Are gamma-ray bursts the sources of ultra-high energy cosmic rays? *Astroparticle Physics*, 62:66–91, March 2015.
- [56] E. Waxman and J. Bahcall. High energy neutrinos from cosmological gamma-ray burst fireballs. *Phys. Rev. Lett.*, 78:2292–2295, 1997.
- [57] Boaz Katz, Ran Budnik, and Eli Waxman. The energy production rate & the generation spectrum of uhecrs. *JCAP*, 2009(03):020, 2009.
- [58] M. Ahlers et al. Grbs on probation: testing the uhe cr paradigm with icecube. *APh*, 35:87–94, 2011.
- [59] D. Guetta et al. Neutrinos from individual gamma-ray bursts in the batse catalog. *Astroparticle Phys.*, 20:429–455, 2004.
- [60] S. Hümmer et al. Neutrino emission from gamma-ray burst fireballs, revised. *Phys. Rev. Lett.*, 108:231101, 2012.
- [61] A. Mücke, R. Engel, J. P. Rachen, R. J. Protheroe, and T. Stanev. Monte Carlo simulations of photohadronic processes in astrophysics. *Computer Physics Communications*, 124:290–314, February 2000.
- [62] M. J. Rees and P. Mszros. Dissipative photosphere models of gamma-ray bursts and x-ray flashes. *ApJ*, 628(2):847, 2005.

- [63] B. Zhang and P. Kumar. Model-dependent high-energy neutrino flux from gamma-ray bursts. *PhRvL*, 110:121101, 2013.
- [64] Franck Bernard. *Caractérisation des performances d'un télescope sous-marin à neutrinos pour la détection du cascades contenues dans le cadre du project ANTARES*. PhD thesis, Université de la Méditerranée, 2000.
- [65] W. M. Yao et al. Review of particle physics. *J. Phys.*, G33:1–1232, 2006.
- [66] P. A. Čerenkov. Visible Radiation Produced by Electrons Moving in a Medium with Velocities Exceeding that of Light. *Phys. Rev.*, 52:378–379, August 1937.
- [67] D. Chirkin and W. Rhode. Propagating Leptons through Matter with Muon Monte Carlo (MMC). ArXiv e-print, July 2004.
- [68] M. Ackermann, J. Ahrens, X. Bai, et al. Optical Properties of Deep Glacial Ice at the South Pole. *J. Geophys. Res.*, 111:D13203, July 2006.
- [69] K. Woschnagg. Optical Properties of South Pole Ice at Depths from 140 to 2300 Meters. *International Cosmic Ray Conference*, 2:200, 1999.
- [70] IceCube Collaboration, M. G. Aartsen, R. Abbasi, et al. Measurement of South Pole ice transparency with the IceCube LED calibration system. *ArXiv e-prints*, January 2013.
- [71] N. E. Bramall, R. C. Bay, K. Woschnagg, R. A. Rohde, and P. B. Price. A deep high-resolution optical log of dust, ash, and stratigraphy in South Pole glacial ice. *Geophys. Res. Lett.*, 32:21815, November 2005.
- [72] A. Achterberg, M. Ackermann, J. Adams, et al. First Year Performance of the IceCube Neutrino Telescope. *Astropart. Phys.*, 26:155–173, October 2006.
- [73] R. Abbasi, Y. Abdou, T. Abu-Zayyad, et al. Calibration and characterization of the IceCube photomultiplier tube. *Nuclear Instruments and Methods in Physics Research A*, 618:139–152, June 2010.
- [74] R. Abbasi, M. Ackermann, J. Adams, et al. The IceCube Data Acquisition System: Signal Capture, Digitization, and Timestamping. *Nucl. Instrum. Meth.*, 601:294–316, April 2009.
- [75] N. Whitehorn. *A Search for High-Energy Neutrino Emission from Gamma-Ray Bursts*. PhD thesis, University of Wisconsin-Madison, 2012.
- [76] Charles L. Lawson and Richard J. Hanson. *Solving least squares problems*. Prentice-Hall, Englewood Cliffs, NJ, 1974.

- [77] M. G. Aartsen, R. Abbasi, Y. Abdou, et al. Improvement in fast particle track reconstruction with robust statistics. *Nuclear Instruments and Methods in Physics Research A*, 736:143–149, February 2014.
- [78] S. Boyd and L. Vandenberghe. *Convex Optimization*. Cambridge University Press, New York, 2009.
- [79] Dirk Pandel. Bestimmung von Wasser- und Detektorparametern und Rekonstruktion von Myonen bis 100 TeV mit dem Baikal-Neutrino-Teleskop NT-72. Diploma thesis, Humboldt-Universität zu Berlin, 1996.
- [80] J. Ahrens, X. Bai, R. Bay, et al. Muon Track Reconstruction and Data Selection Techniques in AMANDA. *Nuclear Instruments and Methods A*, 524:169–194, May 2004.
- [81] Norman L. Johnson, Samuel Kotz, and N. Balakrishnan. *Continuous Univariate Distributions*, volume 1, chapter 17. Wiley, New York, 2<sup>nd</sup> edition, 1994.
- [82] G. Japaridze and M. Ribordy. Realistic Arrival Time Distribution from an Isotropic Light Source. ArXiv e-print, June 2005.
- [83] N. van Eijndhoven, O. Fadiran, and G. Japaridze. Implementation of a Gauss Convolved Pandel PDF for Track Reconstruction in Neutrino Telescopes. *Astroparticle Physics*, 28:456–462, December 2007.
- [84] Juan-de-Dios Zornoza and Dmitry Chirkin. Muon energy reconstruction and atmospheric neutrino spectrum unfolding with the IceCube detector. 2007.
- [85] A. Gazizov and M. Kowalski. ANIS: High Energy Neutrino Generator for Neutrino Telescopes. *Comput. Phys. Commun.*, 172:203–213, November 2005.
- [86] H. L. Lai, J. Huston, S. Kuhlmann, et al. Global QCD Analysis of Parton Structure of the Nucleon: CTEQ5 Parton Distributions. *Eur. Phys. J. C*, 12:375–392, February 2000.
- [87] A. M. Dziewonski and D. L. Anderson. Preliminary Reference Earth Model. *Phys. Earth Planet. Inter.*, 25:297–356, June 1981.
- [88] M. Honda, T. Kajita, K. Kasahara, S. Midorikawa, and T. Sanuki. Calculation of Atmospheric Neutrino Flux Using the Interaction Model Calibrated with Atmospheric Muon Data. *Phys. Rev. D*, 75:043006–+, February 2007.
- [89] D. Heck, J. Knapp, J. N. Capdevielle, G. Schatz, and T. Thouw. CORSIKA: A Monte Carlo Code to Simulate Extensive Air Showers. Technical Report FZKA 6019, Forschungszentrum Karlsruhe, Germany, February 1998.



- [90] J. R. Hörandel. On the Knee in the Energy Spectrum of Cosmic Rays. *Astropart. Phys.*, 19:193–220, May 2003.
- [91] S. V. Ter-Antonyan and L. S. Haroyan. About EAS Size Spectra and Primary Energy Spectra in the Knee Region. ArXiv e-print, March 2000.
- [92] J. Lundberg, P. Miočinović, K. Woschnagg, et al. Light Tracking Through Ice and Water: Scattering and Absorption in Heterogeneous Media with PHOTONICS. *Nucl. Instrum. Meth.*, 581:619–631, November 2007.
- [93] J. R. Quinlan. Induction of decision trees. *Mach. Learn.*, 1(1):81–106, March 1986.
- [94] Yoav Freund and Robert E Schapire. A decision-theoretic generalization of on-line learning and an application to boosting. *Journal of computer and system sciences*, 55(1):119–139, 1997.
- [95] Michael J Kearns and Yishay Mansour. A fast, bottom-up decision tree pruning algorithm with near-optimal generalization. In *ICML*, volume 98, pages 269–277. Citeseer, 1998.
- [96] G. C. Hill, J. Hodges, B. Hughey, A. Karle, and M. Stamatikos. Examining the Balance Between Optimising an Analysis for Best Limit Setting and Best Discovery Potential. In L. Lyons and M. Karagöz Ünel, editors, *Statistical Problems in Particle Physics, Astrophysics and Cosmology: Proceedings of PHYSTAT05*, pages 108–111, London, 2005. Imperial College Press.
- [97] M.G. Aartsen et al. Searches for Extended and Point-like Neutrino Sources with Four Years of IceCube Data. 2014.
- [98] J. T. Kent. The fisher-bingham distribution on the sphere. *J. Royal Stat. Soc.*, 44:71–80, 1982.
- [99] K. J. Meagher. *Limits on Neutrino Emission from Gamma-Ray Bursts with the 40 String IceCube Detector*. PhD thesis, University of Maryland, 2012.
- [100] P. C. Redl. *A search for muon neutrinos coincident with Gamma-ray Bursts with the IceCube 59-String detector*. PhD thesis, University of Maryland, 2011.
- [101] A. Achterberg, M. Ackermann, J. Adams, et al. Five years of searches for point sources of astrophysical neutrinos with the AMANDA-II neutrino telescope. *PhRvD*, 75(10):102001, May 2007.
- [102] R. Abbasi, Y. Abdou, T. Abu-Zayyad, et al. Limits on Neutrino Emission from Gamma-Ray Bursts with the 40 String IceCube Detector. *Phys. Rev. Lett.*, 106(14):141101, April 2011.

- [103] M.G. Aartsen, M. Ackermann, J. Adams, et al. Observation of High-Energy Astrophysical Neutrinos in Three Years of IceCube Data. *PhRvL*, 113:101101, 2014.
- [104] M.G. Aartsen, M. Ackermann, J. Adams, et al. Atmospheric and Astrophysical Neutrinos above 1 TeV Interacting in IceCube. *PhRvD*, 12 2014.